

# Technological advances in deep brain stimulation

*Towards an adaptive therapy*



Kees van Dijk



**TECHNOLOGICAL ADVANCES IN DEEP  
BRAIN STIMULATION**  
TOWARDS AN ADAPTIVE THERAPY

*Kees van Dijk*

# UNIVERSITY OF TWENTE.

Faculty of Electrical Engineering, Mathematics and Computer Science

Department of Biomedical Signals & Systems



This work was supported by Stichting Toegepast Wetenschappelijk Instituut  
voor Neuromodulatie ([www.stichtingtwin.nl](http://www.stichtingtwin.nl))

Cover design: Kees van Dijk  
Printed by: Proefschriftmaken | [Proefschriftmaken.nl](http://Proefschriftmaken.nl)  
Lay-out: Kees van Dijk  
ISBN: 978-90-365-5188-5  
DOI: 10.3990/1.9789036551885

© 2021 Kees van Dijk, The Netherlands. All rights reserved. No parts of this thesis may be reproduced, stored in a retrieval system or transmitted in any form or by any means without permission of the author. Alle rechten voorbehouden. Niets uit deze uitgave mag worden vermenigvuldigd, in enige vorm of op enige wijze, zonder voorafgaande schriftelijke toestemming van de auteur



# **TECHNOLOGICAL ADVANCES IN DEEP BRAIN STIMULATION**

**TOWARDS AN ADAPTIVE THERAPY**

DISSERTATION

to obtain  
the degree of doctor at the Universiteit Twente,  
on the authority of the rector magnificus,  
prof. dr. ir. A. Veldkamp,  
on account of the decision of the Doctorate Board  
to be publicly defended  
on Friday 25 June 2021 at 14.45 hours

by

**Kees Joab van Dijk**

born on the 21st of March, 1986  
in Kampen, The Netherlands

This dissertation has been approved by:

Supervisors

prof. dr. ir. P.H. Veltink

dr. ir. T. Heida

## **Graduation Committee:**

Chair / secretary:

prof. dr. J.N. Kok

Supervisors:

prof. dr. ir. P.H. Veltink  
dr. ir. T. Heida

Committee Members:

prof. dr. C.C. McIntyre  
prof. dr. V. Visser-Vandewalle  
prof. dr. Y. Temel  
prof. dr. ir. M.J.A.M. van Putten  
prof. dr. R.J.A. van Wezel

Opgedragen aan mijn vader (1953-2020)

# Table of Contents

<b>SUMMARY</b>	<b>9</b>
<b>SAMENVATTING</b>	<b>13</b>
<b>LIST OF ACRONYMS</b>	<b>17</b>
<b>CHAPTER 1 :</b>	
<i>GENERAL INTRODUCTION AND THESIS OUTLINE</i>	<b>19</b>
<b>CHAPTER 2 :</b>	
<i>A NOVEL LEAD DESIGN ENABLES SELECTIVE DEEP BRAIN STIMULATION OF NEURAL POPULATIONS IN THE SUBTHALAMIC REGION</i>	<b>33</b>
<b>CHAPTER 3 :</b>	
<i>AVOIDING INTERNAL CAPSULE STIMULATION WITH A NEW EIGHT CHANNEL STEERING DEEP BRAIN STIMULATION LEAD</i>	<b>51</b>
<b>CHAPTER 4 :</b>	
<i>SPATIAL LOCALIZATION OF SOURCES IN THE RAT SUBTHALAMIC MOTOR REGION USING AN INVERSE CURRENT SOURCE DENSITY METHOD</i>	<b>71</b>
<b>CHAPTER 5 :</b>	
<i>QUANTIFICATION OF HAND MOTOR SYMPTOMS IN PARKINSON'S DISEASE: A PROOF-OF-PRINCIPLE STUDY USING INERTIAL AND FORCE SENSORS</i>	<b>89</b>
<b>CHAPTER 6 :</b>	
<i>MEASURING HAND AND FINGER MOVEMENTS TO EVALUATE MEDICATION-INDUCED SYMPTOM IMPROVEMENTS IN PARKINSON'S DISEASE PATIENTS</i>	<b>116</b>
<b>CHAPTER 7 :</b>	
<i>GENERAL DISCUSSION</i>	<b>132</b>
<b>PUBLICATIONS</b>	<b>148</b>
<b>DANKWOORD</b>	<b>152</b>



# Summary

## Technological advances in deep brain stimulation

Parkinson's disease (PD) is clinically characterized by four main motor symptoms; (rest)tremor of the limbs, slowness of voluntary movement (bradykinesia), lack of movement (akinesia), muscle rigidity and balance problems (axial disturbances). A treatment method called deep brain stimulation (DBS) may considerably reduce the patient's motor symptoms. The clinical procedure involves the implantation of a DBS lead, consisting of multiple electrode contacts, through which continuous high frequency (around 130 Hz) electric pulses are delivered in the brain. In this thesis, I presented our research which had the goal to improve current DBS technology, focusing on bringing the conventional DBS system a step closer to adaptive DBS, a personalized DBS therapy. The chapters in this thesis can be seen as individual building blocks for such an adaptive DBS system.

After the introductory chapter, in the **second** and **third** chapter, two novel DBS lead designs are studied and compared to the conventional DBS lead. The lead studied in chapter two contains forty small electrode contacts, and the lead studied in chapter three contains eight electrode contacts, divided over the circumference of the electrode lead. Stimulation through one or a subset of these electrode contacts should allow the physician to steer the stimulation field to a chosen direction, this is called directional DBS. In this thesis, the directional DBS performance of the two novel DBS lead designs is investigated in a detailed computational model. This model consists of a finite element static electric field model combined with multi-compartment neuron and axon models, representing neural populations in the subthalamic region. This region is the most often preferred target for stimulation in case of PD patients. The model showed that both studied leads were able to exploit the novel distribution of the electrode contacts to shape and steer the stimulation field to activate more neurons in the chosen target compared to the conventional lead, and to counteract lead displacement. The results from chapter three also show that correct placement and orientation of the lead in the target remains an important aspect in achieving the optimal stimulation outcome. This type of DBS lead is widely used today.

In the **fourth** chapter, an inverse current source density (CSD) method is applied on local field potentials (LFP) measured in a rat model. The measurements are performed using a fine needle-shaped probe consisting of 16 electrodes positioned. Inserting the probe at multiple locations in the subthalamic region provided us with a fine three dimensional measurement grid. The CSD method allowed us to locate sources of dendritic activation within the subthalamic nucleus (STN), evoked by cortical stimulation. A distinguished pattern of sources was found within the STN related to the dendritic activation by neural



hyper-direct and indirect pathways, transferring information from the activated cortex, through the basal ganglia to the thalamus, and back to the cortex. We discussed that this pattern of CSD sources can act as a landmark within the STN to locate the potential stimulation target.

The **fifth** and **sixth** chapter described the last building block of the DBS system. We introduced an inertial sensors and force sensor based measurement system, which can record hand kinematics and joint stiffness of PD patients. The fifth chapter describes the experimental methods on how this system can be used to objectively monitor three of the main PD symptoms, i.e. tremor, bradykinesia and rigidity. To demonstrate applicability of the system, various outcome parameters of measured hand motor symptoms of the patients in off- versus on-medication condition are presented. The last chapter focusses on one specific symptom: bradykinesia. As the visual assessment during the clinical rating for this symptom especially relies on the assessment of the finger movements, we believed the detailed measurements of the sensory system will be advantageous in rating this symptom. The results of a study including 35 PD patients showed the sensory system and the metrics distilled from the measurement data were proven to be sensitive to detect clinical changes. Multiple metrics showed significant changes between the PD patient's state when he/she was off medication and after his/her medication intake. Metrics sensitive to changes in the clinical state of the patient, which can act as a feedback signal in an adaptive DBS system, are the last building block of the DBS system we presented in this thesis.



# Samenvatting

## Technologische vooruitgang in diepe hersenstimulatie

De ziekte van Parkinson, in het engels “Parkinson’s disease (PD)” wordt gekenmerkt door vier klinisch belangrijke motorische symptomen; (rust) tremor van de ledematen, traagheid in de uitvoering van bewegingen (bradykinesie), het niet uit kunnen voeren van bewegingen (akinesie), spierstijfheid en evenwichtsproblemen (axiale stoornissen). Een behandelmethode genaamd diepe hersenstimulatie, in het engels “deep brain stimulation (DBS)”, kan de motorische symptomen van de patiënt aanzienlijk verminderen. De klinische procedure omvat de implantatie van een DBS-lead met meerdere elektrode contactpunten. Daarmee worden continue, met hoogfrequente (rond 130 Hz) elektrische pulsen, de neuronen in de hersenen gestimuleerd. In dit proefschrift presenteerde ik mijn onderzoek met als doel het verbeteren van de huidige DBS-technologie, waarbij de nadruk ligt om conventionele DBS technologie dichterbij adaptieve DBS te brengen. Deze adaptieve DBS techniek zorgt voor een automatische patiënt specifieke DBS-therapie. De hoofdstukken in dit proefschrift kunnen worden gezien als afzonderlijke bouwstenen voor een dergelijk adaptief DBS-systeem.

Na het inleidende hoofdstuk worden in het **tweede** en **derde** hoofdstuk twee nieuwe DBS-lead ontwerpen bestudeerd en vergeleken met de conventionele DBS-lead. De lead uit hoofdstuk twee bevat veertig kleine elektrode contactpunten, en de lead uit hoofdstuk drie bevat acht elektrode contactpunten, in beide gevallen zijn de contactpunten verdeeld over de omtrek van de lead. Stimulatie via één of meerdere van deze (elektrode) contactpunten zou de arts in staat moeten stellen het stimulatieveld in een bepaalde richting te sturen. Deze techniek wordt directionele DBS genoemd. In dit proefschrift wordt de mogelijkheid van directionele DBS met deze twee nieuwe DBS-leads onderzocht in een gedetailleerd simulatie model. Het model bestaat uit een eindig elementen model om de statische elektrische velden te berekenen, gecombineerd met multi-compartmenten neuron- en axonmodellen van verschillende neurale populaties in het gebied rond de nucleus subthalamicus (STN). Deze hersenkern is een belangrijke “target” bij DBS voor PD patiënten. Het model toont aan dat beide nieuwe DBS-leads in staat zijn om de vernieuwde distributie van de elektrode contactpunten rond de omtrek van de DBS-lead te benutten, en op die manier het stimulatieveld zo te sturen dat meer neuronen in de gekozen target worden gestimuleerd. Het kunnen sturen van het stimulatieveld vermindert ook de gevoeligheid voor foutieve plaatsing van de lead ten opzichte van de target. De resultaten van hoofdstuk drie laten zien dat de juiste oriëntatie van de lead in de target een belangrijk aspect blijft bij het bereiken van het optimale stimulatie-resultaat. Dit type DBS-lead wordt tegenwoordig veel gebruikt.

In het **vierde** hoofdstuk wordt een inverse current source density (CSD) methode toegepast op lokale veldpotentialen gemeten in een rat model. De metingen zijn uitgevoerd met een fijn, naaldvormig meetinstrument met 16 elektrode contactpunten. Door dit instrument op meerdere locaties in de STN in te brengen, kregen we een fijn driedimensionaal meetraster. De CSD-methode stelde ons in staat meerdere bronnen van dendritische activatie te lokaliseren in de STN. De activering werd opgewekt door corticale stimulatie, wat leidde tot een uniek patroon van bronnen binnen de STN. Deze bronnen kunnen we relateren aan dendritische activatie door neurale hyper-directe en indirecte paden. Via deze paden wordt informatie overgebracht vanaf de geactiveerde cortex, via de basale ganglia naar de thalamus, en terug naar de cortex. Tot slot bespreken we in het laatste discussie hoofdstuk dat dit patroon van CSD-bronnen als een oriëntatiepunt kan dienen binnen de STN om de potentiële DBS target te lokaliseren.

In het **vijfde** en **zesde** hoofdstuk beschrijven we de laatste bouwsteen van het adaptieve DBS-systeem. In hoofdstuk vijf introduceren we een meetsysteem bestaande uit inertieële sensoren en een krachtsensor, dat kan worden gebruikt om de handkinematica en gewrichtsstijfheid van PD-patiënten te meten. Naast het meetsysteem wordt ook de experimentele methode beschreven om met dit systeem drie van de belangrijke PD-symptomen objectief te monitoren, namelijk tremor, bradykinesie en rigiditeit. Om de toepasbaarheid van het systeem aan te tonen, worden verschillende uitkomstparameters gepresenteerd van patiënten met- en zonder -medicatie. In het laatste hoofdstuk staat één symptoom centraal: bradykinesie. De klinische beoordeling van dit symptoom wordt met name gedaan aan de hand van de beoordeling van de vingerbewegingen. Wij zien daarom, bij het beoordelen van dit symptoom, de gedetailleerde objectieve metingen met dit systeem als groot voordeel. De resultaten van ons onderzoek met 35 PD-patiënten laten zien dat de uitkomstparameters gebaseerd op de bewegingsmetingen gevoelig zijn voor het detecteren van klinische veranderingen. Meerdere uitkomstparameters laten significante veranderingen zien tussen de toestand van de PD-patiënt met of zonder actieve medicatie. Binnen het kader van dit proefschrift kunnen de uitkomstparameters die gevoelig zijn voor veranderingen in de klinische toestand van de patiënt mogelijk gebruikt worden als feedbacksignaal in een adaptief DBS-systeem.



# List of acronyms

3D	Three dimensional
ANOVA	Analyses of variance
AV	angular velocity
BG	Basal ganglia
CC-lead	cylindrical contact lead
Cl	Chloride
CoM	Center of mass
CSD	Current source density
DBS	Deep brain stimulation
DTI	Diffusion tensor imaging
FDA	Food and drug administration
FEM	Finite element method
GABA	Gamma-aminobutyric acid
GPe	Globus pallidus externus
GPI	Globus pallidus internus
HD-lead	High density lead
Hz	Hertz
IC	internal capsule
ICC	interclass coefficient
iCSD	Inverse current source density
IP	Interphalangeal
K	Potassium
LFP	Local field potential
MCP	metacarpophalangeal
MCS	Motor cortex stimulation
MDS	Movement disorder society
ME	Motor examination
MRI	magnetic resonance imaging
Na	Sodium
PD	Parkinson's disease
PSTHs	Post stimulus time histograms
RMS	Root mean square
RoM	Range of motion
SD	Standard deviation
SNc	Substantia nigra pars compacta
SNr	Substantia nigra pars reticulata
STN	Subthalamic nucleus
STR	Striatum
UPDRS	Unified Parkinson's disease rating scale
VTA	Volume of tissue activated





# Chapter 1

General introduction and thesis outline

# General Introduction

## Parkinson's disease

Parkinson's disease (PD) is the second most common neurodegenerative disorder after Alzheimer's disease. Age is an important factor in the onset of the disease, with the disease rarely diagnosed before the age of fifty years and a sharp increase of incidence after an age of sixty years [1, 2]. For example in the Netherlands, a total of around 30 thousand men and 22 thousand women are diagnosed with parkinsonism, giving a prevalence of 3,6 per thousand men and 2,5 per thousand women in the Netherlands [3]. Since the elderly population is growing rapidly in the Netherlands, an increase of the social and economic burden of the disease can be expected in the future.

While Alzheimer's disease causes problems with memory, thinking and behavior, PD is in general known as a movement disorder. The disease is clinically characterized by four main motor symptoms; (rest)tremor of the limbs, slowness of voluntary movement (bradykinesia), muscle rigidity and balance problems (axial disturbances). The diagnosis of the disease is primarily based on these clinical motor symptoms. After excluding secondary parkinsonism, for example caused by certain medications or poisonings, a different nervous system disorder, or another illness, the patient should at least show two of the main motor symptoms. In addition, asymmetric symptom onset and a good response of the symptoms to levodopa medication are supportive for a diagnosis of PD. Besides the main motor symptoms, PD patients can also suffer from non-motor symptoms such as mood changes, sleep disorders, and cognition problems [1, 4, 5].

Diagnoses of PD during the life of the patient is primarily done by evaluation of symptoms, however this only allows us to make an estimate. To be 100% sure if the diagnoses was correct, histological confirmation through postmortem examination needs to be done [4, 6]. This postmortem final diagnoses includes the finding of Lewy bodies, abnormal aggregates of protein that develop inside nerve cells, and a clear degeneration of pigmented neurons in the substantia nigra pars compacta [7]. This particular brain area is important for the production of dopamine in the brain and is part of an important brain network called the basal ganglia (BG), a group of nuclei mainly associated with voluntary motor control functions and also important for limbic and associative non-motor functions [8]. PD symptoms are all closely related to these functions.

## The basal ganglia

Because of the important role of the BG in the pathology and its relation to the clinical symptoms, PD is also called a BG-circuit disorder. The BG-circuit gets its input from the cortex and consists of a network of brain nuclei; the subthalamic nucleus (STN), striatum (STR), globus pallidus internus (GPi), globus pallidus externus (GPe), substantia nigra pars reticulata (SNr), and the substantia nigra pars compacta (SNc) (Figure 1-1). The STN and STR receive input from many of the different cortical areas, including a large input pathway from the motor cortex. The GPi and the SNr provide the BG output to the thalamus and brainstem, with the thalamus connecting back to the cortex closing the cortico-basal ganglia-thalamo-cortical loop. We can distinguish three pathways through which the cortical information flows through the BG. First, the hyperdirect pathway, where the STN receives input from the cortex and then directly connects to the GPi. Second, the direct pathway, where the cortical input from the STR flows to the GPi. Third, the indirect pathways, where the cortical input not directly flows to the output structures, but first goes through the GPe and STN. In addition, there is an internal feedback loop between the STN and the GPe, and the dopamine producing SNc provides important modulating input to the STR [9-11].

In case of PD, the loss of dopaminergic neurons in the SNc causes changes in neural activity within the basal ganglia and abnormal synchronized oscillatory activity at multiple levels of the cortico-basal ganglia-thalamo-cortical loop. The power of oscillatory neural activity can be divided into different frequency bands. Three major frequency bands of oscillation have been identified in the BG which relates to functional movements and PD symptoms, i.e. 10 Hertz (Hz) and lower frequencies, 11 to 30 Hz (beta band), and the range from 60 Hz and higher frequencies (high gamma). Within the PD group the influence of levodopa treatment shows interesting differences in the different bands. In the untreated PD state compared to the treated case, synchronized activity is more prominent at the frequency of rest and

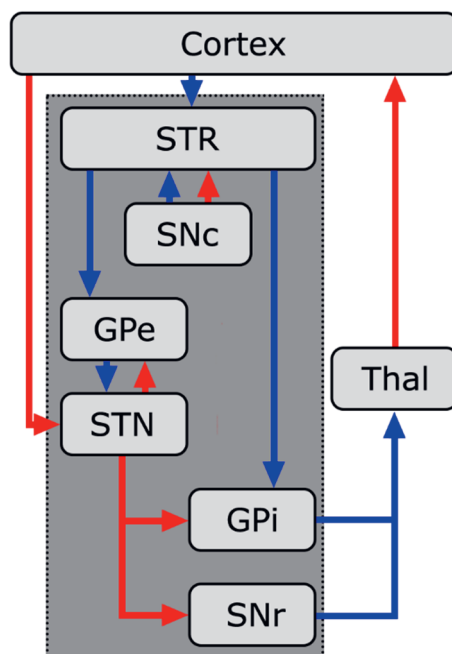


Figure 0-1, A schematic representation of the cortico - basal ganglia - thalamo - cortical circuits. Blue arrows indicate inhibitory projections and red arrows represent excitatory projections. The thalamus is denoted with Thal in the figure.

action tremor at 3 to 10 Hz and show high power in the beta band. Levodopa intake reduces the power at the lower frequencies and increases the power in the gamma band. The BG activity synchronized at 60 Hz is considered to be prokinetic, advantageous for the performance of movements, and important to start and stop voluntary movements [12-14].

## Deep brain stimulation

As PD symptoms are caused by the loss of dopaminergic neurons, an obvious way to treat these is by dopamine replacement therapy. For this purpose, the dopamine precursor levodopa is used often in the early stages of the disease. Unfortunately, in later stages of this progressive the disease the dose needs to get higher and higher, causing disabling side effects [15]. A therapy for PD which is based on modulation of the pathological oscillatory behavior in the BG, is deep brain stimulation (DBS) [16]. The therapy involves implanting an internal pulse generator that generates high frequency electrical pulses that are continuously delivered via a lead consisting of multiple electrode contacts to a specific target in the brain. DBS of the STN, has proven to be an effective treatment of the various motor symptoms and reduces medication needs [17, 18]. The placement of the lead requires precise stereotaxic surgery. Before surgery, the stimulation targets are predetermined by indirect targeting using stereotactic coordinates and imaging techniques, such as magnetic resonance imaging or computer tomography to determine the target in the individual patient. During surgery, before the stimulation electrode is positioned at its final location, a physiological mapping is done by micro-electrode recordings and subsequent test stimulation. First, the micro-electrode recordings are used to identify specific firing patterns within the STN area. Next, test stimulation is performed to confirm symptomatic improvement and side effects while the patient is awake and in an off-medication state. Once the location with the best symptomatic improvement and the least side effects is found, the DBS lead is implanted. In the outpatient clinic, a few weeks after surgery, the stimulator is turned on and most optimal stimulation settings are selected. The settings are obtained on an empirical basis with monopolar cathodic stimulation with a stimulus frequency of around 120–180 Hz, 60–200  $\mu$ s pulse width and 1–5 mA or 1–5 V stimulation amplitude [19]. Currently, in all patients stimulation is applied continuously, 24 hours a day, and settings can only be modified in the neural modulation clinic, which is often only a few times a year. This means, the stimulation protocol is static and does not depend on the clinical condition of the patient. In case of a minor displacement of the electrodes and non-optimal stimulation settings, current spread outside intended target regions may occur and may induce unwanted stimulation-related side-effects, such as dysarthria, facial contractions, ocular deviations and even mood and cognitive changes [20]. These drawbacks ask for new technological developments, to

reduce side effects, to enable dynamic alteration of stimulation, or just to improve battery lifetime.

## **Novel techniques in Deep Brain stimulation**

After two decennia of minimal changes in DBS technology, there is an emerging research field for novel DBS technology. Some of the new technologies are still in an experimental phase, however, while others are currently being introduced in the clinic. We can distinguish three promising trends: alternative stimulation signals, steering DBS, and adaptive DBS.

### **Stimulation signals:**

Trends in alternative stimulation signals includes innovation in the shape of the stimulation waveforms, regulated current vs. regulated voltage waveforms, and different temporal patterns of stimulation [21, 22]. The conventional stimulation signal is a regular pulse train with a high pulse frequency ( $>120$  Hz). Reducing the number of pulses per seconds will decrease the energy consumption, which is an important consideration for the size, battery life and recharge frequency in case of rechargeable batteries of implanted pulse generators. However regular low frequency stimulation has shown to be harmful and worsen the tremor and bradykinesia of the patient [23, 24]. As described before, the oscillatory activation in the BG in the gamma frequency band are considered to be prokinetic. A novel stimulation paradigm uses personalized regular stimulation within the gamma frequency band (30-90 Hz) with outcomes similar as obtained with the conventional high frequency stimulation [25]. Besides regular stimulation at lower frequencies also irregular patterns of stimulation have been studied in computational models, non-human primates, and human patients. Some irregular patterns seem to be as effective as or even more effective than conventional DBS [26, 27]. The finding that the effects of DBS are dependent on the temporal pattern of stimulation, in addition to the frequency of stimulation, has driven the scientific field to design and test novel temporal patterns of DBS.

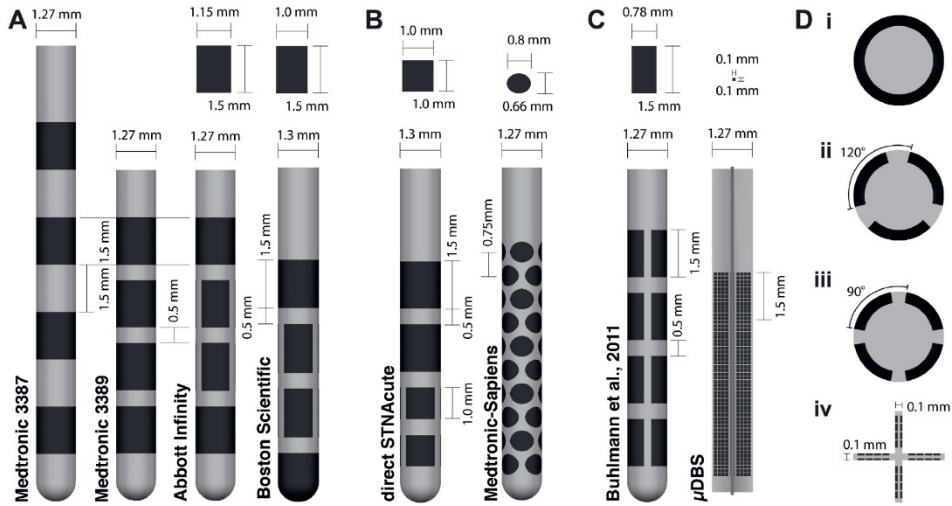


Figure 1-2 , An overview of multiple DBS lead designs, including the dimensions of the lead and contacts. (A) four FDA-approved lead designs include the Medtronic 3387/3389, the eight-contact Abbott Infinity lead and the eight-contact Boston Scientific lead. (B) two directional leads that have not yet been approved by the FDA, but have been implanted in human patients for testing; i.e. the eight-contact direct STNacute and the 40-contact Medtronic-Sapiens lead. (C) Two lead designs that have not been implanted into human patients; i.e. the 16-contact segmented from Buhlmann et al. and the  $\mu$ DBS. (D) Cross-sections of the DBS electrodes. (i) Axisymmetric ring contacts, as seen in the Medtronic 3387/3389 and other cylindrical contacts on directional leads. (ii) Axisymmetric ring contacts segmented into three smaller contacts, such as the Abbott infinity, the Boston scientific and the direct STNacute (iii) Four contacts per rotation can be found in the Medtronic-Sapiens and the segmented lead from Buhlmann et al. (iv) Plus-shaped cross-section found on the  $\mu$ DBS lead. [Figure by Anderson et al. [37]]

Steering-DBS is a method to overcome a big hurdle in DBS, i.e. the stimulation of structures of fibers that cause side effects which may be due to a small misplacement and/or displacement of the lead [28, 29]. Two methods can be seen in steering DBS, i.e. current steering and directional steering. With current steering the shape of the stimulation field is shaped by selecting the appropriate current on each of the contacts, a steering method which is possible with a conventional lead with cylindrical shaped electrodes (Figure 1-2) [30, 31]. Direction steering uses new lead designs (Figure 1-2) which give more freedom to shape the stimulation field by selecting a number of contact points on the lead. This means the novel lead designs in general have more contact points. Currently, eight channel lead designs, which all started with a lead specifically designed for a directional steering DBS study by Pollo et al. [32], are further developed by industry. The eight channel leads by Boston Scientific (Marlborough, Massachusetts, US) and Abbott (former St. Jude Medical) (Lake Bluff, Illinois, U.S) have been approved by the food and drug administration (FDA), received the CE-mark in 2015, and are introduced in the clinic [33]. These leads contain a cylindrically shaped and rounded contact at the bottom,

followed by two cylinders that are split into three individual electrode contacts for directional steering-DBS, and the top electrode is a cylindrical shaped contact again. Besides the already FDA approved leads, a few other promising lead design were introduced. For example the eight-contact direct STNacute and the 40-contact Medtronic-Sapiens (Medtronic Inc., Minneapolis, US), which have both been tested in human patients. The latter allows precise directional steering DBS through a high-density array of 40 contacts [34]. Until now, this lead has only been tested intra-operatively as the increased number of contacts demanded complex and vulnerable electric connectivity. This made it not suited for chronic implantation yet. Finally, two lead designs, which are not tested in human patients yet, are the 16-contact segmented lead [35] and the micro-array based DBS lead, the  $\mu$ DBS, with 1760 contacts [36].

### Adaptive DBS:

The last technological advancement is Adaptive DBS, which is based on automatically (and continuously) estimating the clinical condition of the PD patient and using this information to automatically adapt the stimulation parameters. An adaptive DBS protocol aims to reduce the patient's need, caused by the deteriorating nature of the disease, for visiting the neural-modulation clinic to manually modify the stimulation settings. On a shorter time scale adaptive DBS possibly would be able to react on the fluctuating clinical state of the patient during the day, where in theory, stimulation is given only when necessary. This way, adaptive DBS may generate less side effects, show increased functional improvement and reduced energy consumption of the DBS stimulation protocol [38-40].

To develop adaptive DBS protocols a feedback signal is required, which enables reliable robust estimation of the clinical state of that individual subject. Firstly, we can distinguish between feedback based on electrophysiological signals, which can be measured in the BG circuit with the DBS lead or with a separate measurement electrode. Using the DBS lead not only to stimulate but also as a measurement device has the big advantage that no additional steps in the conventional DBS surgical procedure are needed. The limitations are that only signals in the BG-circuit can be used and as the DBS lead electrodes are relative big only local field potentials (LFP) can be measured. Nevertheless, using the LFP beta band power as a feedback signal has recently shown to be a suitable feedback signal with promising results [41]. Secondly, feedback signals can be based on wearable sensors to record movements, such as gyroscopes and accelerometers. Monitoring and quantifying PD symptoms with such sensors have been an important topic in the last decade and important progress has been made in this field. Especially tremor seems to be a detectable symptom and feasible as a robust feedback signal for adaptive DBS [38].

Thirdly, feedback based on questionnaires, which can be answered on mobile phone applications. This is a less objective measure than those obtained from wearable sensors. However, the more subjective nature of the questionnaires takes into account the patient's interpretation of the motor symptoms and non-motor symptoms and its effects on the quality of life [38].

In conclusion, adaptive DBS is a technology which is still under development, and needs clinical trials to establish a good understanding of the relation between possible feedback signals and PD symptoms. Especially one feedback signal which is robust and sensitive for multiple motor and non-motor symptom has not yet been found.

## The aim of the present study

In this thesis I aim to improve multiple aspects of the current DBS technology, with the focus on bringing the conventional DBS system a step closer to adaptive DBS. Figure 1-3 shows a graphical representation of the DBS system we envision, including corresponding chapter numbers of this thesis.

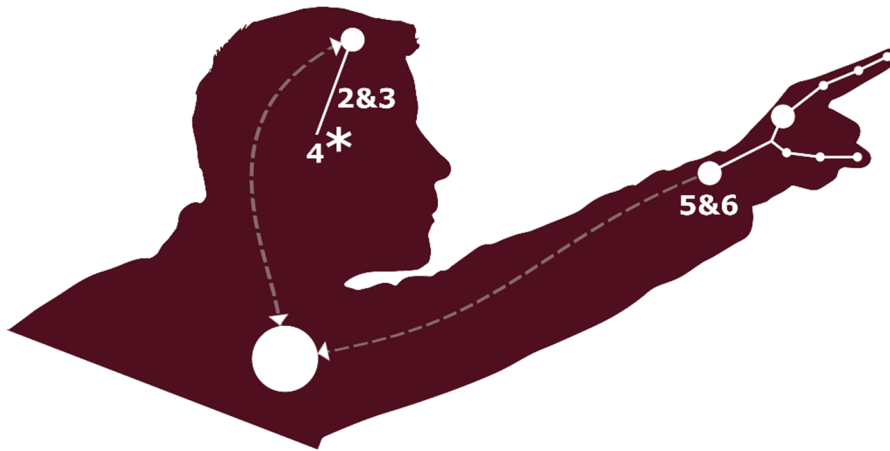


*Figure 1-3 A graphical representation of a DBS system, including the thesis chapter numbers in which we elaborate on that specific part of the system; i.e. chapter 2&3 discuss novel DBS leads, chapter 4 electrophysiological signals measured in the DBS target, chapter 5&6 describes the quantitative measurement of PD symptoms.*



## Thesis outline

**Chapter 2:** This is the first of two chapters describing novel lead designs which can be used for directional steering DBS. In this first chapter a detailed computational model of the brain is described, which consists of a finite element model to calculate the electric stimulation field and neuron multi-compartment models to study the effect of the electric field on the brain tissue. This model is used to study a novel high density DBS lead with forty electrode contact points and to compare the performances of this new lead design with the conventional cylindrical contact lead.

**Chapter 3:** In this chapter a computational model approach is also used to study the performance of a new directional steering DBS lead. Instead of the novel lead from chapter 2, which consists of forty contact points, the DBS lead studied in this chapter consists of eight electrode contacts, and is clinically available nowadays.

**Chapter 4:** In this chapter we focus on electrophysiological signals, which can be measured within the STN. In future, these signals might provide information on the condition of the patient, which can be used in adaptive DBS. In this chapter, we introduce the use of the current source density method as a way to visualize the spatial organization of evoked electrophysiological responses in the STN. This fundamental study is performed in rats and can be seen as an exploratory study on data analyses methods which can be used in the future on measurements performed in humans with high density leads such as described in chapter 2.

**Chapter 5:** In this chapter we focus on measuring hand movements to quantify the four cardinal PD symptoms. In the future, this information can be used directly as a feedback signal in adaptive DBS or to find the relation between electrophysiological signals and PD symptoms. This chapter describes a proof of principal study on measuring PD symptoms with an instrumented glove including inertial sensors and magnetometers and an additional force sensor.

**Chapter 6:** In this chapter we focus on hand movement analyses to quantify the PD symptom bradykinesia. We perform reliability analyses of different parameters and demonstrate patient specific symptom improvements induced by medication.

## References

1. Poewe, W., Seppi, K., Tanner, C. M., Halliday, G. M., Brundin, P., Volkmann, J., ... & Lang, A. E. (2017). Parkinson disease. *Nature reviews Disease primers*, 3(1), 1-21.
2. Van Den Eeden, S. K., Tanner, C. M., Bernstein, A. L., Fross, R. D., Leimpeter, A., Bloch, D. A., & Nelson, L. M. (2003). Incidence of Parkinson's disease: variation by age, gender, and race/ethnicity. *American journal of epidemiology*, 157(11), 1015-1022.
3. M.M.J. Nielen (NIVEL), M.J.J.C. Poos (RIVM) ,B. Post (UMCN) F.F. Jager red. (RIVM), <https://www.volksgezondheidenzorg.info/onderwerp/ziekte-van-parkinson/cijfers-context/huidige-situatie#node-prevalentie-ziekte-van-parkinson-huisartsenpraktijk>, 04-09-2019
4. Gelb DJ, Oliver E, Gilman S. Diagnostic Criteria for Parkinson Disease. *Arch Neurol*. 1999;56(1):33–39. doi:10.1001/archneur.56.1.33
5. Jankovic J Parkinson's disease: clinical features and diagnosis *Journal of Neurology, Neurosurgery & Psychiatry* 2008;79:368-376.
6. Joutsa, J., Gardberg, M., Røyttä, M., & Kaasinen, V. (2014). Diagnostic accuracy of parkinsonism syndromes by general neurologists. *Parkinsonism & related disorders*, 20(8), 840-844
7. Gibb, W. R., & Lees, A. (1988). The relevance of the Lewy body to the pathogenesis of idiopathic Parkinson's disease. *Journal of Neurology, Neurosurgery & Psychiatry*, 51(6), 745-752.
8. Albin, R. L., Young, A. B., & Penney, J. B. (1989). The functional anatomy of basal ganglia disorders.
9. Parent, A., & Hazrati, L. N. (1995). Functional anatomy of the basal ganglia. II. The place of subthalamic nucleus and external pallidum in basal ganglia circuitry. *Brain research reviews*, 20(1), 128-154.
10. Marani, E., Heida, T., Lakke, E. A., & Usunoff, K. G. (2008). The subthalamic nucleus: Part I: Development, cytology, topography and connections (Vol. 198). Springer Science & Business Media.
11. Nambu, A., Tokuno, H., & Takada, M. (2002). Functional significance of the cortico-subthalamo-pallidal 'hyperdirect' pathway. *Neuroscience research*, 43(2), 111-117.
12. Brown, P., Oliviero, A., Mazzone, P., Insola, A., Tonali, P., & Di Lazzaro, V. (2001). Dopamine dependency of oscillations between subthalamic nucleus and pallidum in Parkinson's disease. *Journal of Neuroscience*, 21(3), 1033-1038.
13. Levy, R., Ashby, P., Hutchison, W. D., Lang, A. E., Lozano, A. M., & Dostrovsky, J. O. (2002). Dependence of subthalamic nucleus oscillations on movement and dopamine in Parkinson's disease. *Brain*, 125(6), 1196-1209.
14. Cassidy, M., Mazzone, P., Oliviero, A., Insola, A., Tonali, P., Lazzaro, V. D., & Brown, P. (2002). Movement-related changes in synchronization in the human basal ganglia. *Brain*, 125(6), 1235-1246.

15. Jankovic, J. (2005). Motor fluctuations and dyskinesias in Parkinson's disease: clinical manifestations. *Movement disorders: official journal of the Movement Disorder Society*, 20(S11), S11-S16.
16. McIntyre, C. C., Savasta, M., Kerkerian-Le Goff, L., & Vitek, J. L. (2004). Uncovering the mechanism (s) of action of deep brain stimulation: activation, inhibition, or both. *Clinical neurophysiology*, 115(6), 1239-1248.
17. Deuschl, G., Schade-Brittinger, C., Krack, P., Volkmann, J., Schäfer, H., Bötzel, K., ... & Gruber, D. (2006). A randomized trial of deep-brain stimulation for Parkinson's disease. *New England Journal of Medicine*, 355(9), 896-908.
18. Benabid, A. L. (2003). Deep brain stimulation for Parkinson's disease. *Current opinion in neurobiology*, 13(6), 696-706.
19. Machado, A., Rezai, A. R., Kopell, B. H., Gross, R. E., Sharan, A. D., & Benabid, A. L. (2006). Deep brain stimulation for Parkinson's disease: surgical technique and perioperative management. *Movement disorders: official journal of the Movement Disorder Society*, 21(S14), S247-S258.
20. Temel, Y., Kessels, A., Tan, S., Topdag, A., Boon, P., & Visser-Vandewalle, V. (2006). Behavioural changes after bilateral subthalamic stimulation in advanced Parkinson disease: a systematic review. *Parkinsonism & related disorders*, 12(5), 265-272.
21. Rossi, P. J., Gunduz, A., Judy, J., Wilson, L., Machado, A., Giordano, J. J., ... & McIntyre, C. C. (2016). Proceedings of the third annual deep brain stimulation think tank: a review of emerging issues and technologies. *Frontiers in neuroscience*, 10, 119.
22. Ramirez-Zamora, A., Giordano, J. J., Gunduz, A., Brown, P., Sanchez, J. C., Foote, K. D., ... & McIntyre, C. (2018). Evolving applications, technological challenges and future opportunities in neuromodulation: proceedings of the fifth annual deep brain stimulation think tank. *Frontiers in neuroscience*, 11, 734.
23. Timmermann, L., Wojtecki, L., Gross, J., Lehrke, R., Voges, J., Maarouf, M., ... & Schnitzler, A. (2004). Ten-Hertz stimulation of subthalamic nucleus deteriorates motor symptoms in Parkinson's disease. *Movement disorders: official journal of the Movement Disorder Society*, 19(11), 1328-1333.
24. Fogelson, N., Kühn, A. A., Silberstein, P., Limousin, P. D., Hariz, M., Trottenberg, T., ... & Brown, P. (2005). Frequency dependent effects of subthalamic nucleus stimulation in Parkinson's disease. *Neuroscience letters*, 382(1-2), 5-9.
25. Deeb, W., Giordano, J. J., Rossi, P. J., Mogilner, A. Y., Gunduz, A., Judy, J. W., ... & Dougherty, D. D. (2016). Proceedings of the fourth annual deep brain stimulation think tank: a review of emerging issues and technologies. *Frontiers in integrative neuroscience*, 10, 38.
26. Bocker, D. T., Swan, B. D., Turner, D. A., Gross, R. E., Tatter, S. B., Koop, M. M., ... & Grill, W. M. (2013). Improved efficacy of temporally non-regular deep brain stimulation in Parkinson's disease. *Experimental neurology*, 239, 60-67.

27. Tass, P. A., Qin, L., Hauptmann, C., Dovero, S., Bezard, E., Boraud, T., & Meissner, W. G. (2012). Coordinated reset has sustained aftereffects in Parkinsonian monkeys. *Annals of neurology*, 72(5), 816-820.
28. Okun, M. S., Tagliati, M., Pourfar, M., Fernandez, H. H., Rodriguez, R. L., Alterman, R. L., & Foote, K. D. (2005). Management of referred deep brain stimulation failures: a retrospective analysis from 2 movement disorders centers. *Archives of neurology*, 62(8), 1250-1255.
29. Butson, C. R., Cooper, S. E., Henderson, J. M., & McIntyre, C. C. (2007). Patient-specific analysis of the volume of tissue activated during deep brain stimulation. *Neuroimage*, 34(2), 661-670.
30. Frankemolle, A. M., Wu, J., Noecker, A. M., Voelcker-Rehage, C., Ho, J. C., Vitek, J. L., ... & Alberts, J. L. (2010). Reversing cognitive-motor impairments in Parkinson's disease patients using a computational modelling approach to deep brain stimulation programming. *Brain*, 133(3), 746-761.
31. Chaturvedi, A., Foutz, T. J., & McIntyre, C. C. (2012). Current steering to activate targeted neural *Brain stimulation* pathways during deep brain stimulation of the subthalamic region., 5(3), 369-377.
32. Pollo, C., Kaelin-Lang, A., Oertel, M. F., Stieglitz, L., Taub, E., Fuhr, P., ... & Schüpbach, M. (2014). Directional deep brain stimulation: an intraoperative double-blind pilot study. *Brain*, 137(7), 2015-2026.
33. Dembek, T. A., Reker, P., Visser-Vandewalle, V., Wirths, J., Treuer, H., Klehr, M., ... & Timmermann, L. (2017). Directional DBS increases side-effect thresholds—A prospective, double-blind trial. *Movement Disorders*, 32(10), 1380-1388.
34. Contarino, M. F., Bour, L. J., Verhagen, R., Lourens, M. A., de Bie, R. M., van den Munckhof, P., & Schuurman, P. R. (2014). Directional steering: a novel approach to deep brain stimulation. *Neurology*, 83(13), 1163-1169.
35. Buhlmann, J., Hofmann, L., Tass, P. A., & Hauptmann, C. (2011). Modeling of a segmented electrode for desynchronizing deep brain stimulation. *Frontiers in neuroengineering*, 4, 15.
36. Willsie, A. C., & Dorval, A. D. (2015). Computational field shaping for deep brain stimulation with thousands of contacts in a novel electrode geometry. *Neuromodulation: Technology at the Neural Interface*, 18(7), 542-551.
37. Anderson, D. N., Osting, B., Vorwerk, J., Dorval, A. D., & Butson, C. R. (2018). Optimized programming algorithm for cylindrical and directional deep brain stimulation electrodes. *Journal of neural engineering*, 15(2), 026005.
38. Habets, J. G., Heijmans, M., Kuijf, M. L., Janssen, M. L., Temel, Y., & Kubben, P. L. (2018). An update on adaptive deep brain stimulation in Parkinson's disease. *Movement Disorders*, 33(12), 1834-1843.
39. Priori, A., Foffani, G., Rossi, L., & Marceglia, S. (2013). Adaptive deep brain stimulation (aDBS) controlled by local field potential oscillations. *Experimental neurology*, 245, 77-86.

40. Little, S., Pogosyan, A., Neal, S., Zavala, B., Zrinzo, L., Hariz, M., ... & Green, A. L. (2013). Adaptive deep brain stimulation in advanced Parkinson disease. *Annals of neurology*, 74(3), 449-457.
41. Little, S., Beudel, M., Zrinzo, L., Foltynie, T., Limousin, P., Hariz, M., ... & Aziz, T. Z. (2016). Bilateral adaptive deep brain stimulation is effective in Parkinson's disease., Neurosurgery. *Journal of Neurology & Psychiatry*, 87(7), 717-721.



# Chapter 2

A novel lead design enables selective deep brain stimulation of  
neural populations in the subthalamic region

*Based on:*

Van Dijk, K. J., Verhagen, R., Chaturvedi, A., McIntyre, C. C., Bour, L. J., Heida, C., & Veltink, P. H. (2015). A novel lead design enables selective deep brain stimulation of neural populations in the subthalamic region. *Journal of neural engineering*, 12(4), 046003.

## Abstract

*Objective.* The clinical effects of deep brain stimulation of the subthalamic nucleus (STN-DBS) as a treatment for Parkinson's disease are sensitive to the location of the DBS lead within the STN. New high density (HD) lead designs have been created which are hypothesized to provide additional degrees of freedom in shaping the stimulating electric field. The objective of this study is to compare the performances of a new HD lead with a conventional cylindrical contact (CC) lead.

*Approach.* A computational model, consisting of a finite element electric field model combined with multi-compartment neuron and axon models representing different neural populations in the subthalamic region, was used to evaluate the two leads. We compared ring-mode and steering-mode stimulation with the HD lead to single contact stimulation with the CC lead. These stimulation modes were tested for the lead 1) positioned in the centroid of the STN, 2) shifted one mm towards the internal capsule (IC), and 3) shifted two mm towards the IC. Under these conditions, we quantified the number of STN neurons that were activated without activating IC fibers, which are known to cause side-effects.

*Main results.* The modelling results show that the HD lead is able to mimic the stimulation effect of the CC lead. Additionally, in steering-mode stimulation there was a significant increase of activated STN neurons compared to the CC mode.

*Significance.* From the model simulations we conclude that the HD lead in steering-mode with optimized stimulation parameter selection can stimulate more STN cells. Next, the clinical impact of the increased number of activated STN cells should be tested and balanced across the increased complexity of identifying the optimized stimulation parameter settings for the HD lead.



## Introduction

Deep brain stimulation (DBS) for Parkinson's disease (PD) patients may reduce considerably their symptoms including tremor, rigidity and akinesia [1, 2]. The clinical procedure involves the implantation of a DBS lead, consisting of multiple electrode contacts, through which continuous high frequency electric pulses (typically with a frequency of 130 Hz and pulse duration of 60-90  $\mu$ s) are delivered in a specific brain area [3]. In the case of PD, the preferred targeted brain area is the subthalamic nucleus (STN) [4-6]. This nucleus is a small biconvex shaped structure located deep in the brain and is surrounded by several bundles of myelinated fibers such as the lenticular fasciculus, and internal capsule (IC) [7]. The clinical outcome of the therapy is rather sensitive to the precise location of the DBS lead within the STN [8, 9]. Unfortunately, despite careful stereotactic planning with high-tech 3D MRI imaging techniques, placement errors within a range from 1 to 3 mm still may occur [10, 11]. Also, a DBS lead which initially was placed correctly post-surgery may become displaced over time due to several reasons [12, 13].

In case of a displaced lead, the injected stimulation current will spread out to unwanted brain regions and, for instance, may evoke activation in the easily excitable myelinated fibers passing nearby [14]. Activation of some of these myelinated fiber tracts may have a positive clinical effect, as is the case for the efferent globus pallidus internus (GPi) fibers in the lenticular fasciculus [15], or the motor cortex axons of the hyperdirect pathway [16]. However, both activation of fibers in the IC as well as neurons in the non-sensorimotor part of the STN may cause undesirable side-effects including ocular deviation, speech difficulties, facial contractions, a decline in cognitive functioning, and mood changes, [9, 17-21]. Given these side-effects, it is crucial to prevent unwanted current spread and ultimately to be able to compensate for a displacement without the need to reposition the DBS lead.

To compensate for positioning errors, the stimulating electric field can be adjusted by selecting the appropriate electrode contact(s) on the lead. In this manner, the conventional lead, consisting of four cylindrical contacts (CC), is able to compensate for a displacement primarily in the dorsal-ventral direction. New lead designs are currently in development, which additionally enable steering of the stimulating field in the lateral-medial and anterior-posterior directions through a high-density (HD) array of contacts [22, 23]. An example of this type is the HD lead in development at Sapiens Steering Brain Stimulation BV (Eindhoven, NL), which is currently in a clinical test phase [24]. The latest design of this HD lead, will consist of ten rows along the lead and each row containing four individual oval shaped electrode contacts, facing different directions (Figure 2-2). With this design, the spatial steering of the stimulation field is achieved by activation of an

appropriate combination of the 40 available contacts. Unfortunately, the high amount of possible combinations of contacts will increasingly complicate selecting optimal stimulation parameters. Therefore, more insight is needed into the spatial steering-modes of HD leads and new tools need to be developed to find these optimal steering parameters.

Computational models can be used to evaluate and visualize steering-modes DBS effects in the brain [22, 25, 26]. For example, Martens et al. (2010) evaluated a prototype design of a HD lead using a computational model. In their model, they showed that the high density lead is able to spatially steer the electric field in a homogeneous isotropic volume conductor and shift the center of the volume of activated tissue. This result suggests that indeed it is possible to compensate for lead displacement using an HD lead. However, as they also noted in their discussion, calculations were performed under the assumption that the brain acts as a homogenous isotropic volume conductor. In general, the state of the art electric field models with heterogeneous anisotropic volume conduction show significant differences in the shape of their reconstructed electric fields compared to the homogeneous isotropic models [14, 27-29]. To evaluate the possibility to compensate for a lead displacement, the effect of the steered field on the various neural populations in the subthalamic region needs to be estimated. The activation effect is often estimated by the volume of tissue activated, i.e. the tissue enclosed within an iso-surface of the activation function [30, 31]. However, a more realistic approach, with respect to the surrounding axon fiber bundles, is to evaluate the stimulation effect in more detailed multi-compartment neuron models of different neural populations in the subthalamic region [28].

In this study, we used computational models to investigate the stimulation effect of a HD lead and its ability to compensate for a lead displacement. The model system, based on a previous study by Chaturvedi et al. (2012), included a heterogeneous anisotropic volume conductor with multi-compartment neuron and axon models of three important neural populations in the subthalamic region [32]. Two populations, i.e., the STN projections cells and the efferent GPi fibers in lenticular fasciculus, represent therapeutic DBS targets while a third population, i.e., the IC fibers, represents a neural population that will cause side-effects when stimulated. In the current model we have compared the stimulation effect of the conventional CC lead with that of a HD lead, which has 40 contacts. The aim of the computer simulation was to initiate an action potential in a maximum percentage of STN cells without activating IC fibers. Simulations were performed with the DBS leads positioned at three different locations within the STN, using different stimulation modes.

## Materials and Methods

### The subthalamic region

In the current study the computational model of the subthalamic region used was based on previous work of Chaturvedi et al. (2012). In summary, their model system consists of two parts; the electric field model, and the neuron model. The electric field model is a finite element method (FEM) model with the geometry and volume conduction properties of the subthalamic region based on a human brain atlas, which consists of a T1 MRI and a diffusion tensor imaging (DTI) dataset [33]. The DTI dataset was used to estimate the anisotropy and heterogeneity of the tissue conductivity in the brain [34]. The model incorporated a 0.5 mm tissue encapsulation layer around the electrode to account for the chronic electrode impedance of around 1 k $\Omega$  for the CC lead. A multiresolution finite element mesh was used with over 4.2 million nodes. In this FEM model the Poisson equation was solved in three-dimensions to determine the potential field generated by current stimulation, and was carried out in SCIRun v3.0.2 (University of Utah, Salt Lake City, US). The computed potential field formed the input into the neuron model, which is a multi-compartment neuron model programmed in NEURON 6.2 (Yale university, New Haven, US) [35]. The model consists of three neural populations in the subthalamic region, which are most likely activated by DBS. These neural populations are the STN projections cells, the efferent GPi fibers in the lenticular fasciculus, and the IC fibers. The STN and GPi axon trajectories were based on non-human primate cell tracings [36, 37], and the IC fiber trajectories were based on streamline tractography using the DTI dataset accompanying the brain atlas. Because morphologic data of the axons of the neural populations was limited, and to enable consistent comparison between stimulation induced activation of the different neural populations, and variability between different axon models, every axon was implemented with the same model parameters (5.7  $\mu$ m axon diameter model[38]). Finally, SCIRun v3.0.2 was used for visualization of the complete model (Figure 2-1).

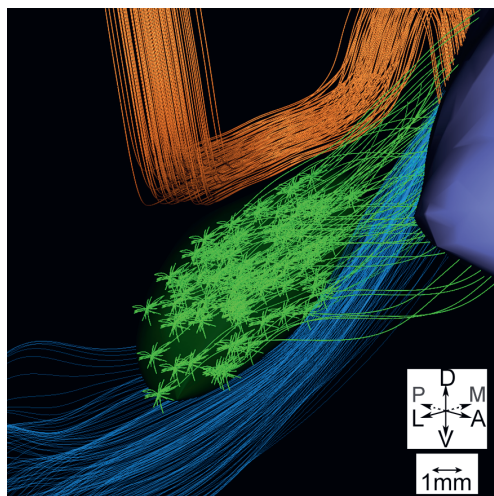


Figure 2-1. The anatomical model of the subthalamic region viewed from anterior-lateral direction. Two relevant nuclei are shown: the STN (green volume), and the globus pallidus (purple volume). The three neural populations are shown: the efferent GPi fibers (orange), the IC fibers (blue) and the STN projection neurons (green).

## DBS lead geometry

Either a CC lead or an HD lead (Figure 2-2) was incorporated within the FEM model. The CC lead was based on the Medtronic 3389 electrode (Medtronic Inc., Minneapolis, US), which has a body diameter of 1.27 mm and carries four cylindrical contacts (C0-C3). These contacts each have a length of 1.5 mm, a 6 mm<sup>2</sup> contact surface area, and an inter-electrode spacing of 0.5 mm. The HD lead was based on the Sapiens Steering Brain Stimulation lead design, which also has a diameter of 1.27 mm and carries 40 oval shaped electrode contacts. The 40 contacts are divided into ten rows (R0-R9) of four contacts, and each row is rotated by 45 degrees from each other. Each oval shaped contact has a 0.42 mm<sup>2</sup> contact surface area, and contact center-to-center distances of 1 mm and 0.75 mm in the horizontal and vertical directions, respectively.

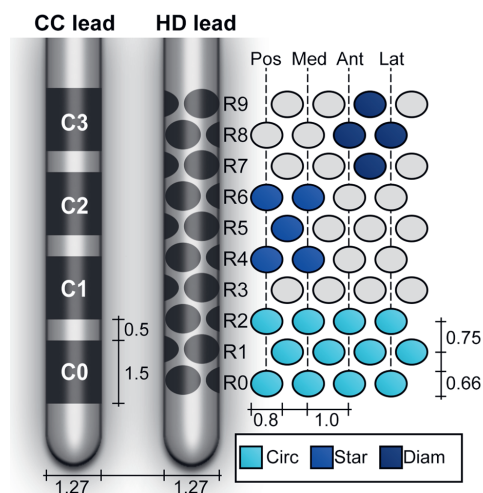


Figure 2-2. Representation of CC lead (left) and the HD lead with its schematic overview of the 40 contacts (right). Examples of the diam(ond) configuration in anterior-lateral direction, star configuration in posterior-medial direction, and circ(ular)-mode (R0-R2) of the HD lead are indicated in different blue scales.

## DBS lead location

For each simulation only one of the DBS leads was positioned in the STN. This DBS lead was positioned either at the center location, at a 1 mm off-center location, or at a 2 mm off-center location (Figure 2-3). For the center location, the lead targeted the centroid of the STN: the second electrode contact from the tip (C1) of the CC lead was positioned in the center, the fourth row of electrode contacts from the tip (R3) of the HD lead was positioned in the center. At the off-center locations, the lead was linearly shifted 1 mm or 2 mm towards the IC, on the line between the centroid of the STN and the point given by the average location of the nearest axon segments of each IC fiber in the model. This resulted in a shift 0.46 mm posteriorly, 0.59 mm medially, and 0.66 mm ventrally with respect to the center location, per 1 mm displacement. For all three locations, the lead approached the target in an AC/PC-based coordinate system with a typical lead arc and collar angles of 20 degrees and 100 degrees, respectively (Figure 2-3).

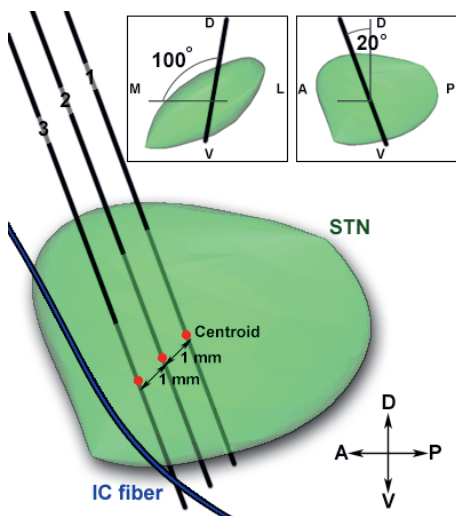


Figure 2-3, Representation of the DBS lead locations. The STN volume is shown in green, one IC fiber is shown in blue, and the three lead trajectories are shown by black lines. Trajectory 1 is the center location, trajectory 2 is the 1 mm off-center location, and trajectory 3 is the 2 mm off-center location. The top two views (left coronal, right sagittal) of the STN show the trajectory arc and collar angles of 20 degrees and 100 degrees, respectively, in an AC/PC-based coordinate system. The main (sagittal) view of the STN shows the shifts of the lead trajectory in the direction of the IC.

## Stimulation protocols

Monopolar stimulation protocols were tested for different contact configurations and stimulation amplitudes. The stimulation signal was a biphasic charge-balanced stimulation pulse, i.e. a 100  $\mu$ s rectangular waveform, with amplitudes ranging from -1 mA to -5 mA with a 0.5 mA step size, followed by a 5 ms period of low amplitude anodic stimulation. The outer boundary of the FEM model was used as reference for the return current. The stimulation signal was used for single source stimulation by evenly spreading the injected current over the selected electrode contact(s). The possible contact configurations varied per lead. For the CC lead, one of the four electrode contacts, C0-C3

(6.0 mm<sup>2</sup> activated electrode surface), was selected to simulate circular-mode stimulation (Figure 2-2). For the HD lead, we distinguish two types of circular-mode stimulation and two types of steering-mode stimulations, i.e. HD circular ‘mimic’, HD circular ‘free’, HD star, and HD diamond (Figure 2-2). For both HD circular modes, three adjacent rows, each with four electrode contacts, (5.0 mm<sup>2</sup> activated electrode surface) were selected for stimulation. In HD circular ‘mimic’ mode, we used the same stimulation pulse amplitude and similar vertical contacts height as the optimal CC configuration, i.e. R0-R2 for C0, R2-R4 for C1, R5-R7 for C2 and R7-R9 for C3. In HD circular ‘free’ mode, there were no constraints in the stimulation pulse amplitude and selection of the vertical contact height. In HD steering-mode, the electrode contacts were selected in either a star or diamond configuration. In the star configuration, five adjacent electrode contacts were selected in either medial, lateral, posterior, anterior, or any of the intermediate directions (2.1 mm<sup>2</sup> activated electrode surface). In the diamond configuration, four adjacent electrode contacts were selected in the medial, lateral, posterior, anterior, or any of the intermediate directions (1.7 mm<sup>2</sup> activated electrode surface). Stimulation in diamond configuration with -5 mA stimulation amplitudes results in the maximum charge density of 29  $\mu\text{C}/\text{cm}^2$ , which is below the often recommended charge density limit of 30  $\mu\text{C}/\text{cm}^2$ . For each stimulation mode, all possible directions and vertical positions of the configurations were simulated to find the optimal settings.

### Activation of neural populations

The effect of the evoked potential field by each stimulation protocol (each amplitude and each contact configuration) was evaluated in the neuron part of the computational model. To quantify the differences between stimulation protocols we aimed to maximize the amount of activated STN cells without activating the IC fibers, but with allowing activation of efferent GPi fibers. A cell or axon is counted as activated when the stimulation pulse evoked at least one action potential that propagated to the end segment of the axon. The optimal stimulation protocol was defined as the configuration that activated the highest percentage of STN cells, without activating any IC fiber.

### Statistical analysis

15 datasets were created to compare the different stimulation configurations statistically. Five datasets were created with the leads at the center location and five datasets for each of the two off-center locations. For each dataset, the STN cell bodies were randomly distributed inside the STN, the GPi fibers were randomly distributed within a given boundary box dorsal to the STN, and the IC fibers were kept constant [32]. Differences were analyzed statistically, using a repeated measures ANOVA test with significance level of 0.05. When necessary, six Bonferroni corrected paired-sample t-tests were performed,

i.e. the CC configuration with each of the four HD configurations, the two HD circular modes (free and mimic) with each other, and the two HD steering modes (star and diamond) with each other.

## Results

In the model system, a population of 99 STN cells, a bundle of 99 GPi fibers, and a bundle of 199 IC fibers were placed in the subthalamic region. Each neuron with a cell segment located at the position of the DBS lead was removed from the model. For the 15 datasets, this resulted in neuron models including  $182.3 \pm 13.1$  IC fibers, 99 GPi fibers, and  $79.8 \pm 4.3$  STN cells.

### Comparison of the CC and HD leads in circular-modes

We compared the circular-mode stimulation of the CC lead with the circular-mode stimulations of the HD lead, both with and without the mimicking constraints ('mimic' and 'free', respectively) (Figure 2-4). The CC lead, with its optimal stimulation settings, was able to activate  $56.6\% \pm 4.8\%$  STN cells at center location,  $31.4\% \pm 1.4\%$  of STN cells at the 1 mm off-center location, and  $6.4\% \pm 4.4\%$  of STN cells at the 2 mm off-center location. The HD lead in circular 'mimic' mode was able to activate  $53.0\% \pm 4.2\%$  of STN cells at center location,  $31.5\% \pm 3.0\%$  cells at the 1 mm off-center location, and  $6.2\% \pm 4.2\%$  cells at the 2 mm off-center location. For all locations, there were no significant differences between the percentage of activation with the CC lead and with the HD lead in circular 'mimic' mode.

Ignoring the mimicking constraints, i.e. the circular 'free' model, resulted in a maximum activation of  $58.5\% \pm 3.7\%$  STN cells at center location,  $31.9\% \pm 2.4\%$  cells at the 1 mm off-center location, and  $7.2\% \pm 4.3\%$  cells at the 2 mm off-center location. In all cases, there were no significant differences between the CC lead and the HD lead, with regard to the number/percentage of activated STN cells and the overall currents that were used. The corresponding optimal stimulation pulse amplitudes for each lead location are presented in Table 2-1.

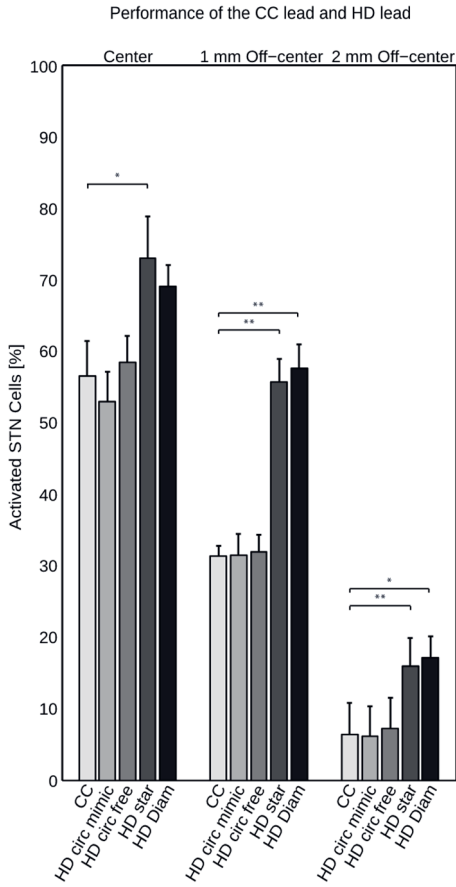


Figure 2-4, The performance of the five stimulation modes, i.e. the CC, HD circ(ular) mimic, HD circ(ular) free, HD star and HD diam(ond). Bars denote mean values with standard deviations of the percentage of activated STN cells after stimulation for the 5 datasets per lead location each with random distributions of the cells/fibers in the neural populations. Significant differences after Bonferroni correction for multiple comparisons ( $n=6$ ) are indicated with one asterisks ( $p<0.05$ ) or two asterisks ( $p<0.01$ ).

Table 2-1. Stimulation effect of the CC lead and HD lead.

	Center		1 mm off-center		2 mm off-center	
	STN [%]	Amp [mA]	STN [%]	Amp [mA]	STN [%]	Amp [mA]
CC	56.6±4.8	4.5±0	31.4±1.4	2.3±0.45	6.4±4.4	0.4±0.22
HD circular 'mimic'	53.0±4.2	4.5±0	31.5±3.0	2.3±0.45	6.2±4.2	0.4±0.22
HD circular 'free'	58.5±3.7	3.9±0.9	31.9±2.4	2.4±0.22	7.2±4.3	0.5±0
HD star	73.0±5.9	4.5±0	55.7±3.2	3.6±0.82	16.0±3.9	1±0
HD diamond	69.1±2.9	5±0	57.7±3.3	3.9±0.22	17.1±3.1	1.5±0
Mean±standard deviation of the percentage of activated STN cells with the corresponding stimulation amplitudes						



## Comparison of the CC and HD leads in steering-modes

Next, we compared the circular-mode stimulation of the CC lead with the HD lead in steering-mode (star and diamond configurations) (Figure 2-4). The star configuration was able to activate  $73.0\% \pm 5.9\%$  of STN cells at the center location,  $55.7\% \pm 3.2\%$  cells at the 1 mm off-center location, and  $16.0\% \pm 3.9\%$  cells at the 2 mm off-center location. The percentage of activated STN cells by the HD lead in star steering mode was significantly larger at the center location ( $p < 0.05/6$ ) as well as at the off-center locations ( $p < 0.01/6$ ). The diamond configuration was able to activate  $69.1\% \pm 2.9\%$  of STN cells at the center location,  $57.7\% \pm 3.3\%$  cells at the 1 mm off-center location, and  $17.1\% \pm 3.1\%$  cells at the 2 mm off-center location. The percentage of activated STN cells by the HD lead in diamond steering mode was significantly larger at both off-center locations ( $p < 0.01/6$  (1 mm) and  $p < 0.05/6$  (2 mm)). There was no significant difference between the percentages of activated STN cells between the two types of steering configurations. The corresponding stimulation pulse amplitudes for each lead location are also included in Table 2-1.

Finally, each stimulation mode individually activated significantly fewer STN cells at the 1 mm off-center location compared to the activation at center location ( $p < 0.05$ ). However, there was no significant difference between the stimulation of the CC lead at center location and the HD lead stimulation in steering-mode at the 1 mm off-center location. In other words, while the displacement significantly decreased the percentage of STN cell activation of both leads according to our predefined criterion, the HD lead with the 1 mm displacement error was still able to activate a similar amount of STN cells as the CC lead located in the center of the STN (Figure 2-5).

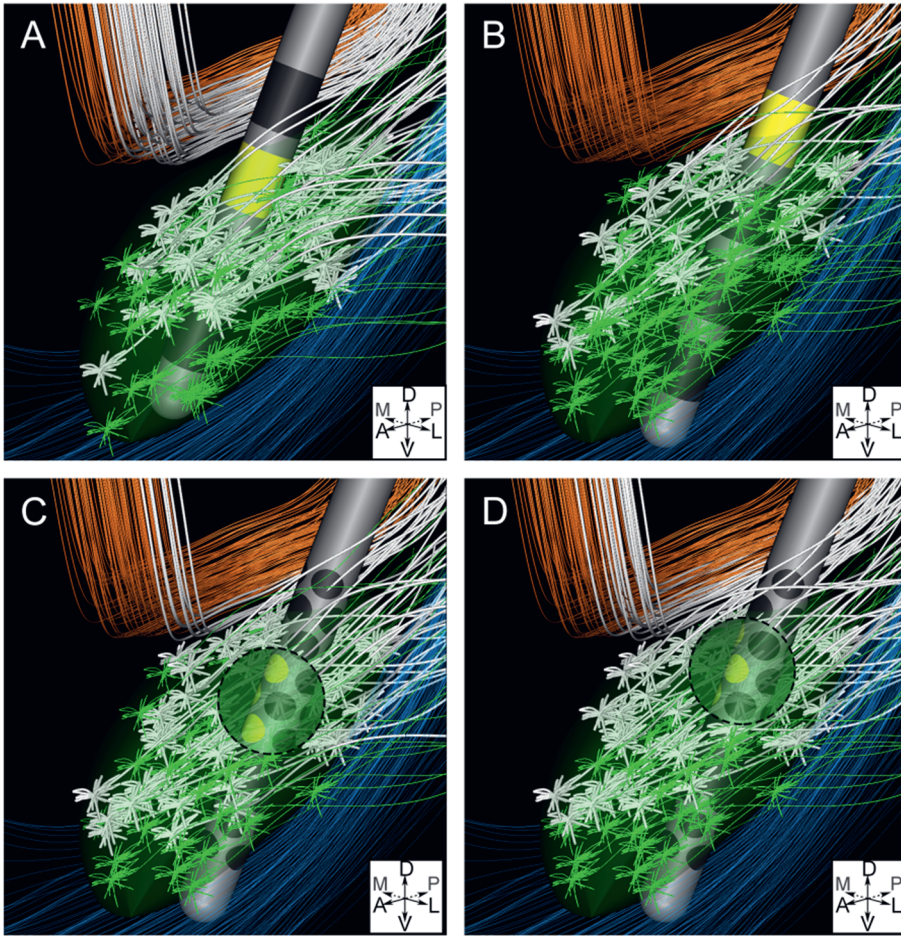


Figure 2-5, An example of the activation of STN cells illustrating the ability to compensate for a lead displacement error using the HD lead. The panels show the GPi efferent fibers in orange, STN cells in green, IC fibers in blue, and the STN cells in green. Cells and fibers that were activated by the stimulation pulse are displayed in white. (A) The optimal configuration of the CC lead at center location [4.5 mA, 53% stimulated STN cells]. (B) The optimal configuration for the CC lead at the 1 mm off-center location [2.5 mA, 31% stimulated STN cells]. (C) The optimal star steering configuration for the HD lead at the 1 mm off-center location [3 mA, 57% stimulated STN cells]. (D) The optimal diamond steering configuration for the HD lead at off-center location [3.5 mA, 56% stimulated STN cells].

## Discussion

In the current study, we used a computational model approach to investigate the stimulation effects of a new HD DBS lead design. The primary advantage of this HD lead is the ability to steer the stimulation field towards target areas and/or away from areas that cause side effects. However, the HD lead should also be able to mimic the conventional circular-mode stimulation. This requirement is important to ensure backwards compatibility with the currently used systems [22]. By stimulating with the HD lead at the same location and amplitude as the CC lead, the HD lead is able to activate a similar percentage of STN cells. Furthermore, the HD lead has more optional configurations than the CC lead. We studied all possible ‘monopolar’ circular-mode stimulation configurations with twelve electrode contacts in three adjacent rows. This resulted in eight different vertical positions with 0.75 mm resolution for the HD lead, against four heights with 1.5 mm resolution for the CC lead. Interestingly, the increased resolution in vertical position did not result in a significantly better performance of the HD lead in circular ‘free’ mode. A potential reason for this might be due to the use of three rows of smaller contacts in HD circular mode, when added together, this covers a slightly larger volume along the vertical direction as compared to a single CC contact. This reduces some specificity of the HD lead. Additionally, the stimulating field in dorsal-ventral direction was only bound by the IC ventrally to the STN. Therefore, by adopting the criterion that IC fibers were not allowed to be activated, the shape of the electric field dorsal of the STN was less critical, and therefore the increased vertical spatial resolution of the HD lead had a minor influence.

When looking at the steering-mode stimulation, the results from the model clearly showed an increased activation by the HD lead compared to the stimulation with the CC lead. The most notable improvement was in the case where the lead was displaced 1 mm towards the IC. While the CC lead was on average only able to activate 31% of the STN cells, the HD lead activated on average 57% STN cells. This amount of activation for the HD lead was similar to the activation with the CC lead at center location. This suggests that the HD lead in steering mode, when displaced 1 mm towards the IC, is still able to generate the same neuron activation effect as the CC lead that is placed at the center of the STN. For the larger displacement of 2 mm, the HD lead in steering-mode stimulation was still able to activate significantly more STN cells than the CC lead. However, the percentages of activated STN cells were very low for all of the stimulation configurations at this location. By having the lead this close to the IC field steering cannot fully compensate for the lead displacement compared to the stimulation effects of the lead at center location.

We should note, however, that we only studied two types of steering-mode stimulation: star and diamond configuration. Other types of contact configurations as well as multipolar stimulation may further increase the performance of the HD lead in specific scenarios. Of course, the same applies for the CC lead. Chaturvedi et al. (2012) showed in a similar computational model that the CC lead in bipolar configuration with two independent sources performs significantly better than the lead in monopolar stimulation. However, allowing additional types of configurations for the HD lead will make it extremely complicated to manually find the optimal DBS settings. Therefore, we limited the configurations to two simple types of steering-modes. Both types used adjacent electrode contacts centered on certain heights and directions of the lead. The results showed no significant differences between the two configuration types. However, at center location there was no significant difference between the diamond configuration and the CC lead, while there was a significantly larger percentage of STN cells stimulated with the star steering configuration. Therefore, we prefer the star configuration for steering-mode stimulation. Also, the star configuration uses five instead of four electrode contacts, which results in a larger contact surface area, and therefore a lower current density per contact [39].

To quantify the stimulation effect we adopted the criterion that a maximum amount of activated STN cells is desired with DBS. Therefore, we searched, for each stimulation mode, for the highest percentage of activated STN cells and allowed activation of the GPi efferent fibers. Several studies [15, 40-42] show that patients with the best clinical outcome tend to have direct activation of axonal tissue dorsal to the STN compared to those who have stimulation confined within the STN. It has been suggested that adverse DBS effects are caused by the fact that the STN contains three functional modalities: motor, limbic and associative functions. Consequently, stimulation of the areas that are not concerned with motor function may result in adverse effects [18, 43]. Additionally, instead of maximizing the activation of motor STN cells it actually might be better to focus on the activation of passing GPi fibers [40], subpopulations of fibers within the IC [44], passing fibers of the substantia nigra [42], or cortical afferents to the STN [16]. Given all these uncertainties, we decided only to focus on maximization of the amount of the activated STN cells, which is conventionally considered as the main target for STN DBS. In principle it can be regarded as an example to show the steering effect of the HD lead on a plausible target.

We decided to focus on maximizing the activation effect, and not on minimizing energy consumption. The DBS battery is implanted under the skin below the clavicle and surgery is needed to replace it once it is depleted. Therefore, battery life is an important aspect in DBS therapy. Shaping the stimulation field to compensate for a lead displacement did demand higher stimulation amplitudes in our model simulations. However, because of

the uncertainties with regard to the selection of target areas for optimal clinical effects, and inaccurate or lack of data on the resistivity of the contacts of the HD lead, a comparison of stimulation power for the different leads and configurations is at this point beyond the scope of our study.

Our model representation of the HD lead was included in a state of the art computational model of the subthalamic region that included many important and realistic details. The technical limitations of this computational model are well described in previous studies [15, 28, 31]. The limitations will have effect on the quantified percentage of activated STN cells. For example, all axons in this model have the same diameter of  $5.7\text{ }\mu\text{m}$  and therefore the same dynamic properties and excitability [38]. In the human nervous system, long-distance connections typically tend to have larger axon diameters. Given this, the IC fibers probably have relatively large axon diameters, while the STN axon diameters are known to be smaller than  $5.7\text{ }\mu\text{m}$  [45]. In this study, the size of the IC fibers was more important for the results, because the selection of the steering mode stimulation parameters was based on avoiding activation of these IC fibers. In general, larger diameter axons are more easily excitable than smaller diameter ones. Therefore, when using IC pathway activation as a proxy to avoid side-effects, it seemed logical to more accurately describe the IC axons with a larger diameter model. Finally, since our results focus on a comparison between the CC and HD leads in the same model, the limitations will influence both leads and therefore will have little impact on the comparison. The model already proved to be an adequate tool to study new stimulation paradigms for the CC lead [32]. In this study, we also showed that the model enables to explore new lead designs and prove the concepts of steering-mode stimulation.

## Conclusion

We found that the concepts of steering the stimulation field with a HD lead design used in this study may be beneficial, and it allows to correct for lead displacement errors. We have demonstrated that even a simple steering-mode outperforms current state of the art systems. However, more research is needed on the stimulation of other therapeutic targets and side-effect regions. In the future this information can be incorporated into a patient specific model, based on the one used in this study, to help select the contact configuration with the best therapeutic window for each patient individually.

## References

1. Breit S, Schulz JB, and Benabid AL. Deep brain stimulation. *Cell Tissue Res* 2004; 318(1): p. 275-88.
2. Benabid AL. Deep brain stimulation for Parkinson's disease. *Curr Opin Neurobiol* 2003; 13(6): p. 696-706.
3. Machado A, Rezai AR, Kopell BH, Gross RE, Sharan AD, and Benabid AL. Deep brain stimulation for Parkinson's disease: surgical technique and perioperative management. *Mov Disord* 2006; 21 Suppl 14: p. S247-58.
4. Hamani C, Richter E, Schwab JM, and Lozano AM. Bilateral subthalamic nucleus stimulation for Parkinson's disease: a systematic review of the clinical literature. *Neurosurgery* 2005; 56(6): p. 1313-21; discussion 1321-4.
5. Krack P, Batir A, Van Blercom N, et al. Five-year follow-up of bilateral stimulation of the subthalamic nucleus in advanced Parkinson's disease. *N Engl J Med* 2003; 349(20): p. 1925-34.
6. Odekerken VJ, van Laar T, Staal MJ, et al. Subthalamic nucleus versus globus pallidus bilateral deep brain stimulation for advanced Parkinson's disease (NSTAPS study): a randomised controlled trial. *Lancet Neurol* 2013; 12(1): p. 37-44.
7. Hamani C, Saint-Cyr JA, Fraser J, Kaplitt M, and Lozano AM. The subthalamic nucleus in the context of movement disorders. *Brain* 2004; 127(Pt 1): p. 4-20.
8. Hamel W, Fietzek U, Morsnowski A, et al. Deep brain stimulation of the subthalamic nucleus in Parkinson's disease: evaluation of active electrode contacts. *J Neurol Neurosurg Psychiatry* 2003; 74(8): p. 1036-46.
9. Okun MS, Tagliati M, Pourfar M, et al. Management of referred deep brain stimulation failures: a retrospective analysis from 2 movement disorders centers. *Arch Neurol* 2005; 62(8): p. 1250-5.
10. Fitzpatrick JM, Konrad PE, Nickele C, Cetinkaya E, and Kao C. Accuracy of customized miniature stereotactic platforms. *Stereotact Funct Neurosurg* 2005; 83(1): p. 25-31.
11. Zylka W, Sabczynski J, and Schmitz G. A Gaussian approach for the calculation of the accuracy of stereotactic frame systems. *Medical Physics* 1999; 26(3): p. 381-391.
12. van den Munckhof P, Contarino MF, Bour LJ, Speelman JD, de Bie RM, and Schuurman PR. Postoperative curving and upward displacement of deep brain stimulation electrodes caused by brain shift. *Neurosurgery* 2010; 67(1): p. 49-53; discussion 53-4.
13. Contarino MF, Bot M, Speelman JD, et al. Postoperative displacement of deep brain stimulation electrodes related to lead-anchoring technique. *Neurosurgery* 2013; 73(4): p. 681-8; discussion 188.
14. McIntyre CC, Mori S, Sherman DL, Thakor NV, and Vitek JL. Electric field and stimulating influence generated by deep brain stimulation of the subthalamic nucleus. *Clin Neurophysiol* 2004; 115(3): p. 589-95.
15. Miocinovic S, Parent M, Butson CR, et al. Computational analysis of subthalamic nucleus and lenticular fasciculus activation during therapeutic deep brain stimulation. *J Neurophysiol* 2006; 96(3): p. 1569-80.

16. Li S, Arbuthnott GW, Jutras MJ, Goldberg JA, and Jaeger D. Resonant antidromic cortical circuit activation as a consequence of high-frequency subthalamic deep-brain stimulation. *J Neurophysiol* 2007; 98(6): p. 3525-37.
17. Frankemolle AM, Wu J, Noecker AM, et al. Reversing cognitive-motor impairments in Parkinson's disease patients using a computational modelling approach to deep brain stimulation programming. *Brain* 2010; 133(Pt 3): p. 746-61.
18. Temel Y, Blokland A, Steinbusch HW, and Visser-Vandewalle V. The functional role of the subthalamic nucleus in cognitive and limbic circuits. *Prog Neurobiol* 2005; 76(6): p. 393-413.
19. Funkiewiez A, Ardouin C, Krack P, et al. Acute psychotropic effects of bilateral subthalamic nucleus stimulation and levodopa in Parkinson's disease. *Mov Disord* 2003; 18(5): p. 524-30.
20. Krack P, Fraix V, Mendes A, Benabid AL, and Pollak P. Postoperative management of subthalamic nucleus stimulation for Parkinson's disease. *Mov Disord* 2002; 17 Suppl 3: p. S188-97.
21. Tamma F, Caputo E, Chiesa V, et al. Anatomic-clinical correlation of intraoperative stimulation-induced side-effects during HF-DBS of the subthalamic nucleus. *Neurol Sci* 2002; 23 Suppl 2: p. S109-10.
22. Martens HC, Toader E, Decre MM, et al. Spatial steering of deep brain stimulation volumes using a novel lead design. *Clin Neurophysiol* 2011; 122(3): p. 558-66.
23. Willsie A and Dorval AD. Charge steering in a novel DBS electrode may accommodate surgical targeting errors. in *Neural Engineering (NER), 2013 6th International IEEE/EMBS Conference on*. 2013.
24. Contarino MF, Bour LJ, Verhagen R, et al. Directional steering: A novel approach to deep brain stimulation. *Neurology* 2014; 83(13): p. 1163-9.
25. Keane M, Deyo S, Abosch A, Bajwa JA, and Johnson MD. Improved spatial targeting with directionally segmented deep brain stimulation leads for treating essential tremor. *Journal of Neural Engineering* 2012; 9(4).
26. Pollo C, Kaelin-Lang A, Oertel MF, et al. Directional deep brain stimulation: an intraoperative double-blind pilot study. *Brain* 2014; 137(Pt 7): p. 2015-26.
27. Astrom M, Lemaire JJ, and Wardell K. Influence of heterogeneous and anisotropic tissue conductivity on electric field distribution in deep brain stimulation. *Med Biol Eng Comput* 2012; 50(1): p. 23-32.
28. Chaturvedi A, Butson CR, Lempka SF, Cooper SE, and McIntyre CC. Patient-specific models of deep brain stimulation: influence of field model complexity on neural activation predictions. *Brain Stimul* 2010; 3(2): p. 65-7.
29. Butson CR and McIntyre CC. Tissue and electrode capacitance reduce neural activation volumes during deep brain stimulation. *Clin Neurophysiol* 2005; 116(10): p. 2490-500.
30. Butson CR and McIntyre CC. Role of electrode design on the volume of tissue activated during deep brain stimulation. *J Neural Eng* 2006; 3(1): p. 1-8.
31. Butson CR, Cooper SE, Henderson JM, and McIntyre CC. Patient-specific analysis of the volume of tissue activated during deep brain stimulation. *Neuroimage* 2007; 34(2): p. 661-70.

32. Chaturvedi A, Foutz TJ, and McIntyre CC. Current steering to activate targeted neural pathways during deep brain stimulation of the subthalamic region. *Brain Stimul* 2012; 5(3): p. 369-77.
33. Wakana S, Jiang H, Nagae-Poetscher LM, van Zijl PC, and Mori S. Fiber tract-based atlas of human white matter anatomy. *Radiology* 2004; 230(1): p. 77-87.
34. Tuch DS, Wedeen VJ, Dale AM, George JS, and Belliveau JW. Conductivity tensor mapping of the human brain using diffusion tensor MRI. *Proceedings of the National Academy of Sciences of the United States of America* 2001; 98(20): p. 11697-11701.
35. Hines ML and Carnevale NT. The NEURON simulation environment. *Neural Comput* 1997; 9(6): p. 1179-209.
36. Sato F, Parent M, Levesque M, and Parent A. Axonal branching pattern of neurons of the subthalamic nucleus in primates. *J Comp Neurol* 2000; 424(1): p. 142-52.
37. Parent M and Parent A. The pallidofugal motor fiber system in primates. *Parkinsonism Relat Disord* 2004; 10(4): p. 203-11.
38. McIntyre CC, Richardson AG, and Grill WM. Modeling the excitability of mammalian nerve fibers: Influence of afterpotentials on the recovery cycle. *Journal of Neurophysiology* 2002; 87(2): p. 995-1006.
39. Shannon RV. A Model of Safe Levels for Electrical-Stimulation. *IEEE Transactions on Biomedical Engineering* 1992; 39(4): p. 424-426.
40. Moks CB, Butson CR, Walter BL, Vitek JL, and McIntyre CC. Deep brain stimulation activation volumes and their association with neurophysiological mapping and therapeutic outcomes. *Journal of Neurology Neurosurgery and Psychiatry* 2009; 80(6): p. 659-666.
41. Yelnik J, Damier P, Demeret S, et al. Localization of stimulating electrodes in patients with Parkinson disease by using a three-dimensional atlas-magnetic resonance imaging coregistration method. *J Neurosurg* 2003; 99(1): p. 89-99.
42. Herzog J, Fietzek U, Hamel W, et al. Most effective stimulation site in subthalamic deep brain stimulation for Parkinson's disease. *Movement Disorders* 2004; 19(9): p. 1050-1054.
43. Janssen ML, Zwartjes DG, Temel Y, et al. Subthalamic neuronal responses to cortical stimulation. *Mov Disord* 2012; 27(3): p. 435-8.
44. Xu W, Miciocinovic S, Zhang J, Baker KB, McIntyre CC, and Vitek JL. Dissociation of motor symptoms during deep brain stimulation of the subthalamic nucleus in the region of the internal capsule. *Exp Neurol* 2011; 228(2): p. 294-7.
45. Mathai A, Wichmann T, and Smith Y. More than meets the eye-myelinated axons crowd the subthalamic nucleus. *Mov Disord* 2013; 28(13): p. 1811-5.



# Chapter 3

Avoiding internal capsule stimulation with a new eight  
channel steering deep brain stimulation lead

*Based on:*

van Dijk, K. J., Verhagen, R., Bour, L. J., Heida, C., & Veltink, P. H. (2018).  
Avoiding Internal Capsule Stimulation With a New Eight-Channel Steering Deep  
Brain Stimulation Lead. *Neuromodulation: Technology at the Neural Interface*, 21(6),  
553-561.

## Abstract

*Objective.* Novel deep brain stimulation (DBS) lead designs are currently entering the market, which are hypothesized to provide a way to steer the stimulation field away from neural populations responsible for side effects and towards populations responsible for beneficial effects. The objective of this study is to assess the performances of a new eight channel steering-DBS lead and compare this with a conventional cylindrical contact (CC) lead.

*Approach.* The two leads were evaluated in a finite element electric field model combined with multi-compartment neuron and axon models, representing the internal capsule (IC) fibers and subthalamic nucleus (STN) cells. We defined the optimal stimulation setting as the configuration that activated the highest percentage of STN cells, without activating any IC fibers. With this criterion we compared monopolar stimulation using a single contact of the steering-DBS lead and CC lead, on three locations and four orientations of the lead. In addition, we performed a current steering test case by dividing the current over two contacts with the steering-DBS lead in its worst-case orientation.

*Main results.* In most cases the steering-DBS lead is able to stimulate a significantly higher percentage of STN cells compared to the CC lead using single contact stimulation or using a two contact current steering protocol when there is approximately a 1 mm displacement of the CC lead. The results also show that correct placement and orientation of the lead in the target remains an important aspect in achieving the optimal stimulation outcome.

*Significance.* Currently, clinical trials are set up in Europe with a similar design as the steering-DBS lead. Our results illustrate the importance of the orientation of the new steering-DBS lead in avoiding side effects induced by stimulation of IC fibers. Therefore, in clinical trials sufficient attention should be paid to implanting the steering DBS-lead in the most effective orientation.

## Introduction

With FDA approval for almost 15 years, deep brain stimulation (DBS) of the subthalamic nucleus (STN) has become an established treatment for patients with Parkinson's disease (PD) [1, 2]. PD is a neurological movement disorder and the symptoms of the disease are closely related to pathological neural activity within the basal ganglia network [3]. Because the STN is part of the basal ganglia network, STN-DBS directly modulates the pathological neural activity in the network by use of electric stimulation. Conventionally, this electric stimulation, a continuous train of electric pulses (typically with frequencies between 120-180 HZ, 1-5 mA amplitude, and 60-200  $\mu$ s pulse width [2]), is delivered in the STN through a lead containing four cylindrical contacts (CC) and is powered by a single source from a surgical implanted pulse generator. Until now the technology for DBS has not changed tremendously over the years [4, 5]. Lately however, technological developments have been reported in terms of new stimulation paradigms [6, 7], closed-loop DBS [8-10], independent current source stimulators [11], and directional steering-DBS with high density and 8 channel lead designs [12-14]. Most of the new technologies are still in an early development phase, although some of the technologies are already used in clinic.

Steering-DBS is a method to overcome a big hurdle in DBS, i.e. the stimulation of structures of fibers that cause side effects due to a small misplacement and/or displacement of the lead. The clinical outcome of the therapy is rather sensitive to the precise location of the lead with respect to the target [15, 16]. Unfortunately, displacement of 1 to 3 millimeters can occur during surgery or post-surgery due to several reasons, such as a post-surgery brain shift and inaccuracy of the stereotactic frame and limitations of imaging methods [17-20]. In case of displacement of the lead, the stimulating electric field will influence the neurons and axons outside the intended target region. The target, the STN, is a small biconvex shaped structure surrounded by several bundles of myelinated axons such as the internal capsule (IC) [21]. The large diameter, myelinated axons of the IC are easily stimulated which will induce unwanted side effects, such as dysarthria, muscle contractions and gaze paresis [22].

To compensate for lead displacement, the stimulating electric field can be adjusted by selecting the appropriate electrode contact(s) on the lead. In this manner, with the conventional CC lead it is possible to compensate for a displacement along the direction of the lead. Eight channel lead designs, which started with a lead specifically designed for a study by Pollo et al. by Aleva Neurotherapeutics SA (Lausanne, CH) [14], followed by Boston Scientific (Marlborough, Massachusetts, US) and St. Jude Medical (St. Paul, Minnesota, US), are also able to steer the electric field in the direction perpendicular to

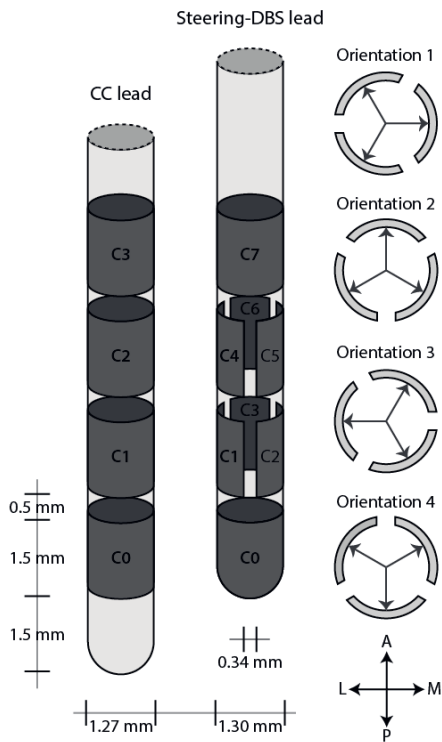


Figure 3-1, Representation of CC lead (left) and the Steering-DBS lead, with a schematic overview of the four orientations (right). Contact C1/C4 is pointing to medial (orientation 1), anterior (orientation 2), lateral (orientation 3), or posterior (orientation 4) direction.

the lead. These leads have eight electrode contacts divided over four heights along the lead. For example, the lead by Boston Scientific contains a cylindrical shaped contact including the tip of the lead as the bottom electrode contact, followed by two cylinders which are split into three individual electrode contacts for directional steering-DBS, and the top electrode is a cylindrical shaped contact (Figure 3-1). In addition, this eight electrode contact lead design can be connected to a matching pulse generator with eight independent current courses. To assess the benefits of this particular steering-DBS system, clinical trials are currently set up in a number of clinics [23].

To aid clinicians in clinical trials, computational models can be used to give more insight in how steering-DBS is able to shape the electric field and affect the surrounding axons and neurons. Patient specific models which are used to visualize the potential field [24] and the volume of tissue activated (VTA), which is based on the spatial second order derivative of the potential field [25], can be a helpful tool for customized DBS-programming in patients. Multiple modeling studies have been performed to get a more accurate representation/estimation of the potential field and VTA by adding biological details in the model such as heterogeneous tissue conductivity, anisotropic conductivity, encapsulation layers and tissue capacitive behavior [26-29]. Next to the visualization, these more realistic models can also be used to automatically select stimulation parameters

[30], to study new lead designs [12, 14, 31, 32], and new stimulation paradigms such as coordinated reset [33]. Previous studies on directional DBS electrodes have emphasized the potential improvement of the clinical effect by avoiding anatomical structures responsible for side effects [12, 14]. In a previous study by the authors, a high density (HD) directional DBS-lead containing 40 contacts, developed at Sapiens Steering Brain Stimulation BV, currently Medtronic Eindhoven Design center (Eindhoven, NL), was assessed in a computational model [34]. Instead of looking at the potential field and VTA volume to avoid certain anatomical structures, this model included multi-compartment neuron and axon models of two important neural populations in the subthalamic region, i.e. the STN neurons, which represent the cells for positive clinical effect, and the IC fibers that will cause side effects when stimulated. Having the two neural populations in the model enabled adjustment of the contact configurations and stimulation amplitudes until the maximum number of activated STN cells was found without stimulating any of the axon fibers of the IC.

In this current study we will use computational modelling procedures to assess the performance of a steering-DBS lead based on the eight electrode contacts lead design. The model includes a heterogeneous anisotropic volume conductor model to compute the evoked potential field in the subthalamic region, and uses multi-compartment neuron and axon models to investigate the stimulation effect of STN cells and the ability to avoid activation of IC fibers. We will compare this stimulation effect of the steering-DBS lead with the CC lead. The effect of one millimeter and two millimeter displacement is investigated, and as the new steering-DBS lead is not cylindrical symmetric we will also study the effect of four different orientations of the lead. Finally, we will test for this steering-DBS lead on each location and orientation the performance of monopolar stimulation versus a current steering stimulation paradigm using two adjacent electrode contacts.

## Materials and Methods

### The computational model

The model system of the DBS target region, the implanted DBS lead, and the stimulation effect on nearby neurons and axons, is based on previous work by Chaturvedi et al. [26, 35]. The model system consists of two consecutive parts. In the first part, the static electric field generated by current controlled stimulation [36], was computed in a finite element method (FEM) model of an adult brain. The geometry and conductivity of the brain is based on a human brain atlas consisting of a T1 MRI and a diffusion tensor imaging (DTI) dataset, with dimensions of 178 mm by 159 mm by 120 mm [37]. The DTI dataset was used to estimate the anisotropy and heterogeneity of the tissue conductivity. A linear

transformation (0.8 S/mm<sup>2</sup> scaling factor) was used to convert the diffusions tensors into conductivity tensors [38]. The FEM model contains the DBS lead with a 0.5 mm tissue encapsulation layer (0.18 S/m) around the lead to account for the chronic electrode impedance of around 1 k $\Omega$  for the CC lead (mean impedance of 1005  $\Omega \pm 6.8 \Omega$  standard deviation for the CC lead contacts in the model). The complete geometry was divided into 4.1 million tetrahedral elements. The outer boundary was set to 0 V and Dirichlet boundary conditions were used. With this FEM model the potential field generated by the stimulation was calculated by solving the Poisson equation in three-dimensions in SCIRun v3.0.2 (University of Utah, Salt Lake City, US).

In the second part, the effect of the electric field on nearby cells was computed in a multi-compartment neuron model programmed in NEURON 6.2 (Yale university, New Haven, US) [39]. Two neural populations are included in the model, i.e. the STN projection cells and the IC fibers. The anatomical geometry of the IC fibers were defined through streamline tractography within SCIRun using the DTI dataset. With this, two hundred fibers were tract from a seedbox (5 by 1 by 2 mm) located ventral-lateral to the STN. Three types of STN cells were placed in the model, each type projecting to the globus pallidus with a slightly different axon trajectory [35, 40]. The somas of the STN cells were placed randomly within the atlas-defined border of the STN volume. Every axon is implemented with the same model parameters (5.7  $\mu\text{m}$  axon diameter model [41]). This cable model includes detailed representations of the nodes of Ranvier, paranodal, and intermodal sections of the axons. For visualization purposes the output from the second part of the model system was again imported in SCIRun v3.0.2.

## DBS lead geometry

Either a CC lead or a steering-DBS lead (Figure 3-1) was incorporated within the FEM model. The CC lead was based on the Medtronic 3389 electrode (Medtronic Inc., Minneapolis, US), which has a body diameter of 1.27 mm and carries four cylindrical contacts (C0-C3). These contacts each have a length of 1.5 mm, a 6 mm<sup>2</sup> contact surface area, and an inter-electrode spacing of 0.5 mm. The steering-DBS lead was based on the design now commercially available by Boston Scientific (Marlborough, Massachusetts, US), which has a body diameter of 1.3 mm and carries 8 contacts (C0-C7). C0 is the contact at the tip of the lead with a length of 1.5 mm and 6 mm<sup>2</sup> contact surface area. Contacts C1-C6 form two rings, each of three steering-DBS contacts with a length of 1.5 mm and 1.6 mm<sup>2</sup> contact surface area. Contact C7 has the same shape as a standard CC lead contact. The inter-electrode spacing along the lead is 0.5 mm and the inter-electrode circumferential spacing between the steering-DBS electrode contacts (C1-C6) is 0.34 mm.

## DBS lead location and orientation

Three locations of the lead were assessed in the model, i.e. the center location, a 1 mm off-center location, and a 2 mm off-center location. For the center location, The CC lead lies inside the STN with the center of contact C1 at the centroid of the STN. In case of the steering-DBS lead the combined center of C1-C3 was located at the centroid of the STN. For the 1 mm and 2 mm off-center location the lead was shifted on a line between the centroid of the STN and the middle position of the nearest axon segments for each IC fiber in the model. This resulted in our datasets in a shift of 0.46 mm, 0.59 mm, and 0.66 mm in posterior, medial, and ventral directionally shift per 1 mm displacement. Unlike the CC lead, the steering-DBS lead is not fully symmetric with respect to the axis of the lead. Therefore, we included four different orientations of the six steering electrode contacts (Figure 3-1). The trajectory of the lead was kept constant in all cases, whereas the lead approached the target in an AC/PC-based coordinate system with a typical lead arc and collar angle of 20 degrees and 100 degrees, respectively.

## Stimulation protocols

For the CC lead, each of the four electrode contacts were selected consecutively for stimulation with increasing stimulation amplitude up to a value at which IC fibers were activated. For the steering-DBS lead, we tested two types of stimulation protocols. Firstly, a single contact stimulation protocol was used, where stimulation on each of the individual single contacts was simulated (Figure 3-2) with increasing stimulation amplitudes up to a value at which IC fibers were activated. Secondly, a current steering stimulation protocol was used, where the current was simultaneously injected through two adjacent contacts with specified percentages (20%/80%, 40%/60%, 60%/40%, 80%/20%) of the total current divided over both contacts, again with increasing stimulation amplitudes up to a value at which IC fibers were activated.

The stimulation signal was a monopolar biphasic charge-balanced current pulse, i.e. a 100  $\mu$ s rectangular waveform, with the total injected current ranging from -1 mA to -5 mA with a 0.5 mA step size, followed by a 5 ms period of low amplitude charge balanced anodic stimulation.

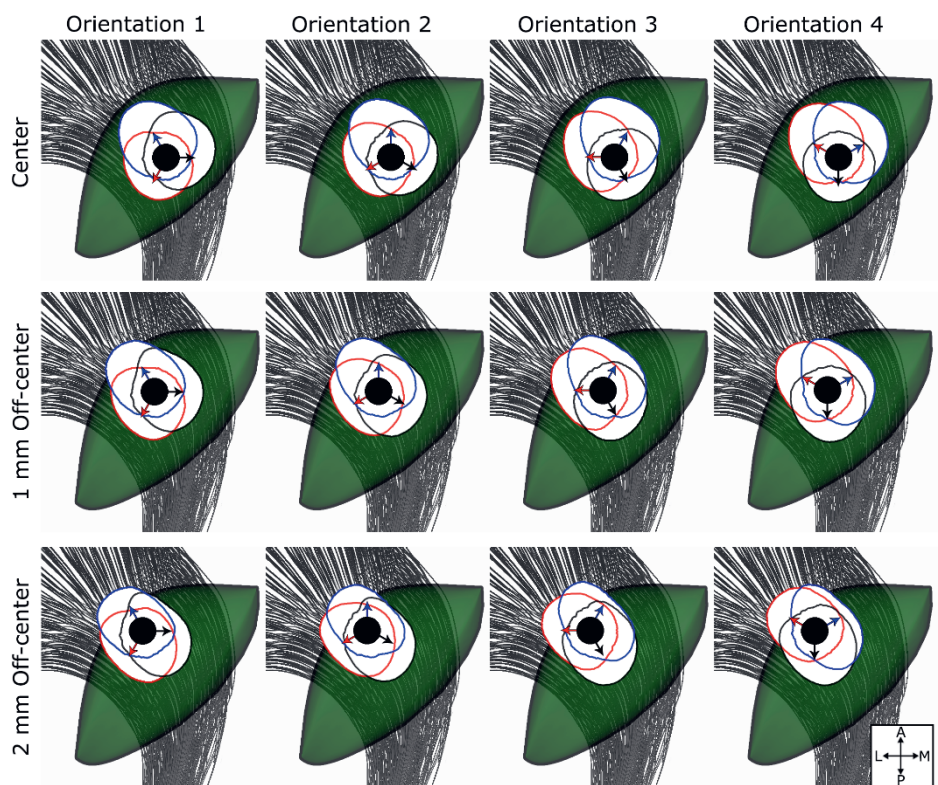


Figure 3-2, Top view of the STN (green volume) with the IC fibers running underneath the STN looking along the axis of the DBS-lead (black circle). On each of the lead locations and orientations, three iso-contours (0.1 V) of the potential field are shown in red, blue and black, corresponding to monopolar stimulation (1 mA) through contact C4-C5-C6 heading in the direction of the color matched arrow. L = lateral; M = medial; P = posterior; A = anterior

## Activation of neural populations

The effect of the deep brain stimulation was evaluated in the neuron part of the computational model system: 15 datasets were created, five for each location of the lead. The STN cell bodies were randomly distributed inside the STN and the location of IC fibers was fixed. Each neuron or axon with a segment located at the position of the DBS lead was removed from the model. For the 15 datasets, this resulted in neuron models including  $182.3 \pm 13.1$  IC fibers and  $79.8 \pm 4.3$  STN cells. A cell or axon is counted as activated when the stimulation pulse evoked at least one action potential that propagated to the end segment of the axon.



## Statistical analysis

To quantify the differences between stimulation protocols we defined the optimal stimulation protocol as the configuration that activated the highest percentage of STN cells, without activating any of the IC fibers. A repeated measure ANOVA with significance level of 0.05 was performed, followed by a Bonferroni corrected multiple comparison procedure to statistically test the individual optimal stimulation effect in each situation. In each of the three lead locations, we compared each of the four lead orientations: optimal single contact stimulation versus optimal current steering stimulation; optimal single contact stimulation versus the optimal stimulation effect of the CC lead; finally, optimal current steering stimulation versus the optimal stimulation effect of the CC lead.

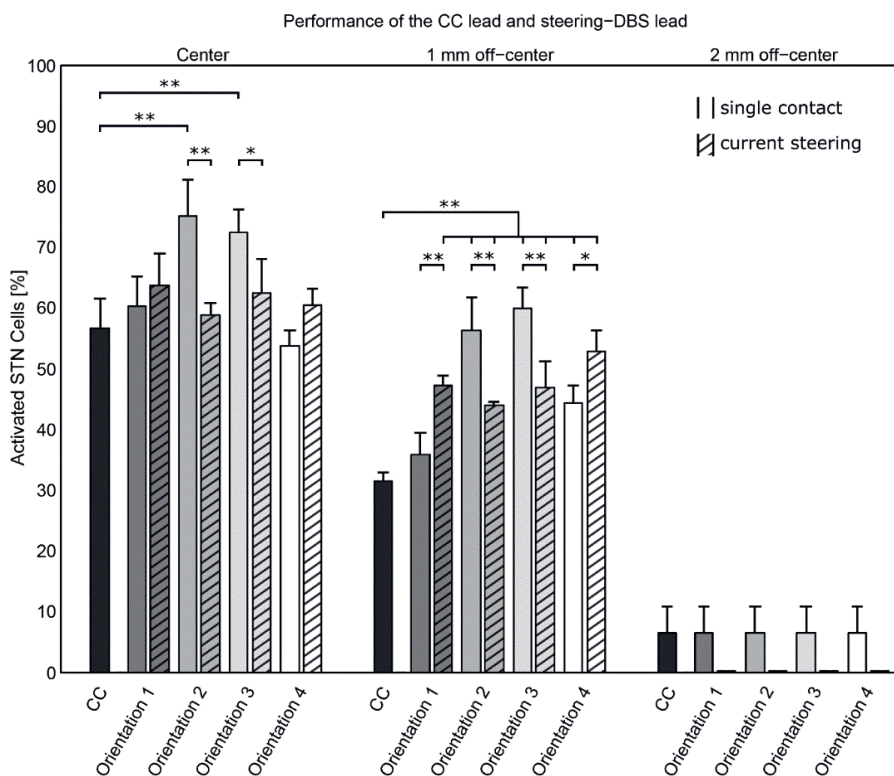


Figure 3-3, The performance of the five stimulation modes, i.e. the CC and the 4 orientations of the steering-DBS lead. Bars denote mean values with standard deviations of the percentage of activated STN cells after stimulation for the 5 datasets per lead location each with random distributions of the STN cells. The non-hatched bars represent the results for single contact stimulation and the hatched bars represent the results for current steering stimulation. Significant differences are indicated with one asterisks ( $p < 0.05$ ) or two asterisks ( $p < 0.01$ ).

## Results

We found for each lead location, orientation, and stimulation protocol the optimal stimulation settings. Figure 3-3 shows the percentage of STN cells which were activated and which denotes all significant differences between the different orientations (see Figure 3-1 for the orientations) and the two stimulation protocols.

### Single contact stimulation protocol

At center location, the steering-DBS lead using single contact stimulation was able to activate  $60.3\% \pm 4.8\%$  STN cells in the first orientation,  $75.1\% \pm 5.9\%$  STN cells in the second orientation,  $72.3\% \pm 3.9\%$  STN cells in the third orientation, and  $53.7\% \pm 2.5\%$  STN cells in the fourth orientation. In the first orientation, the optimal stimulation was applied through the bottom medial contact (3 of 5 datasets) or the top posterior-lateral contact (2 of 5 datasets) with an amplitude of  $4.1 \pm 0.82$  mA. In the fourth orientation, the optimal stimulation was through the bottom or top posterior contact with an amplitude of  $4.3 \pm 0.76$  mA. In both the second and third orientation, the optimal stimulation was through the bottom posterior-medial contact with an amplitude of  $5.0 \pm 0.0$  mA or  $4.5 \pm 0.0$  mA, respectively.

At 1 mm off-center location, the steering-DBS lead was able to activate  $35.8\% \pm 3.5\%$  STN cells in the first orientation,  $56.3\% \pm 5.4\%$  STN cells in the second orientation,  $59.8\% \pm 3.6\%$  STN cells in the third orientation, and  $44.3\% \pm 2.9\%$  STN cells in the fourth orientation. The optimal stimulation settings used the top medial contact ( $2.0 \pm 0.0$  mA) and the top posterior contact ( $2.5 \pm 0.0$  mA) for the first and fourth orientation. In the second and third orientation, the optimal stimulation settings used the top posterior-medial contact ( $3.5 \pm 0.0$  mA and  $4.0 \pm 0.0$  mA, respectively). Figure 3-4 shows the activated STN cells for the optimal stimulation setting in each of the 4 orientations.

At 2 mm off-center location, in each orientation, the steering-DBS lead was able to activate  $6.4\% \pm 4.4\%$  STN cells, while stimulating through the cylindrical contact C7 with an amplitude of  $0.4 \pm 0.22$  mA.

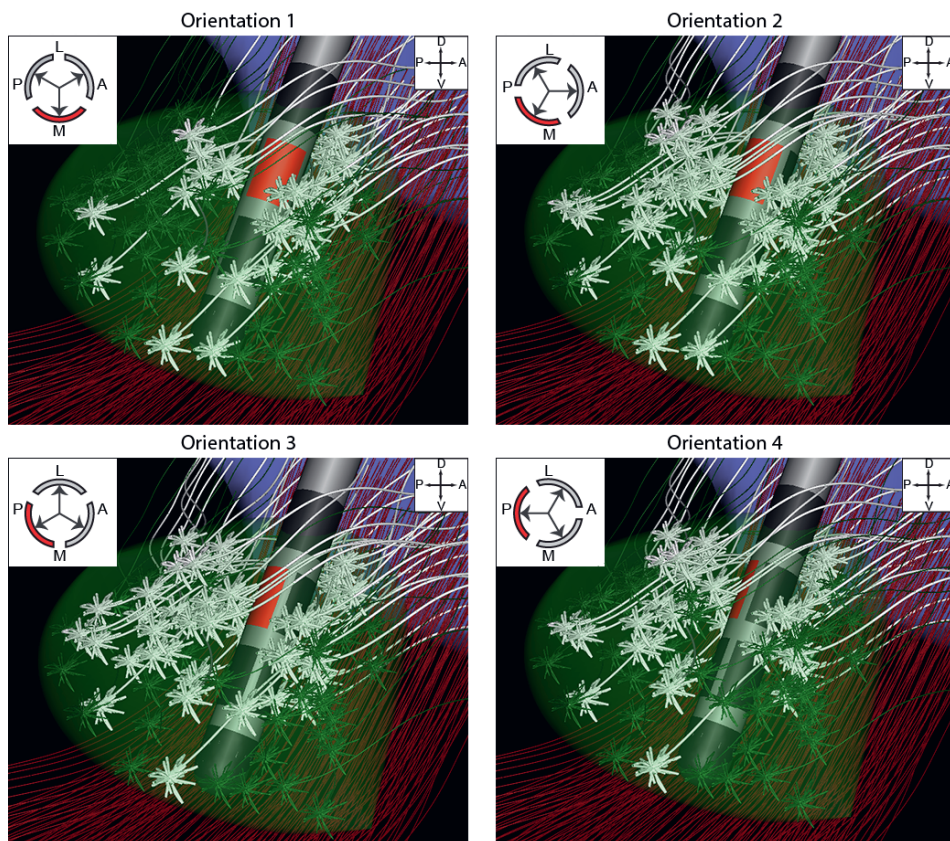


Figure 3-4, An example of the activation of STN cells illustrating the variability in the four orientations while using a monopolar stimulation protocol. The panels show a medial perspective of the STN (green volume), the globus pallidus (purple volume), IC fibers in red, and the STN cells in green and white. STN cells that were activated by the stimulation pulse are displayed in white. The stimulation pulse activated 35%, 55%, 61% and 49% of the STN cells in orientation 1-4 respectively.

### Current steering stimulation protocol

For most of the orientations and datasets our current steering protocol prefers to steer the current into the posterior-medial quadrant, only at the center location in the second orientation four datasets had the optimal stimulation towards the posterior-lateral direction, applying most of the total stimulation current in posterior direction.

At center location with the steering-DBS lead in its first orientation, it was able to activate  $63.7\% \pm 5.2\%$  STN cells by dividing the total current ( $3.8 \pm 0.7$  mA) over the medial contact and post-lateral contact (80%/20% in 4 datasets and 60%/40% in 1 dataset). In the second orientation,  $58.7\% \pm 2.0\%$  STN cells were activated by dividing the total current ( $4.4 \pm 0.8$  mA) over the post-medial and post-lateral contact (80%/20% in 1 dataset, 20%/80% in 2 datasets, 40%/60% in 2 datasets). In the third orientation,  $62.5\% \pm 5.6\%$  STN cells were

activated by dividing the total current ( $3.80 \pm 0.7$  mA) over the post-medial and antero-medial contact (80%/20% in 5 datasets). In the fourth orientation,  $60.4\% \pm 2.9\%$  STN cells were activated by dividing the total current ( $4.1 \pm 1.0$  mA) over the posterior and antero-medial contact (80%/20% in 2 datasets and 60%/40% in 3 datasets). Comparing the stimulation effect of our current steering stimulation protocol to single contact stimulation, we found a significant decrease of activated STN cells in the second orientation ( $p < 0.01$ ) and in the third orientation ( $p < 0.05$ ).

At 1 mm off-center location, the steering-DBS lead was able to activate  $47.2\% \pm 1.5\%$  STN cells in the first orientation by dividing the total current ( $2.5 \pm 0.0$  mA) over the medial contact and post-lateral contact (80%/20% in 2 datasets and 60%/40% in 3 dataset). In the second orientation,  $43.9\% \pm 0.7\%$  STN cells were activated by dividing the total current ( $2.5 \pm 0.0$  mA) over the postero-medial and postero-lateral contact (80%/20% in 5 dataset). In the third orientation,  $46.8\% \pm 4.4\%$  STN cells were activated by dividing the total current ( $2.5 \pm 0.0$  mA) ) over the postero-medial and antero-medial contact (80%/20% in 5 datasets). In the fourth orientation,  $52.9\% \pm 3.4\%$  STN cells were activated by dividing the total current ( $3.0 \pm 0.0$  mA) over the posterior and antero-medial contact (80%/20% in 5 datasets). Comparing the stimulation effect of our current steering stimulation protocol to single contact stimulation, we found a significant decrease of activated STN cells in the second ( $p < 0.01$ ) and third orientation ( $p < 0.01$ ) and a significant increase in the first ( $p < 0.01$ ) and fourth orientation ( $p < 0.05$ ).

At 2 mm off-center location, the steering-DBS lead using the current steering protocol was not able to activate any STN cells without activating one or more IC fibers.

### **Comparison of the CC lead and the steering-DBS lead**

Finally we statically compared the stimulation effect of the steering-DBS lead with the stimulation effect of the CC lead (Figure 3-3). The CC lead, with its optimal stimulation settings, was able to activate  $56.6\% \pm 4.8\%$  STN cells at center location,  $31.4\% \pm 1.4\%$  of STN cells at 1 mm off-center location, and  $6.4\% \pm 4.4\%$  of STN cells at 2 mm off-center location [34]. At center location, the steering-DBS lead using single contact stimulation was able to activate significantly more STN cells in the second and third orientation ( $p < 0.01$ ). Interestingly, in none of the four orientations the steering-DBS lead using current steering stimulation was able to activate significantly more STN cells than the CC lead. At 1 mm off-center location, a significant increase was found for all the orientations when using the current steering stimulation ( $p < 0.01$ ), while using single contact stimulation a significant increase was found at the second, third and fourth orientation ( $p < 0.01$ ). At 2 mm off-center location there were no significant differences found.

## Discussion

In this computational modeling study, we investigated a new steering-DBS lead design. The steering-DBS lead is able to shape the stimulation field by selecting appropriate electrode contacts for stimulation. In this manner, it is possible to stimulate target areas while not stimulating areas that cause side effects. Our results show that under the right circumstances, even using only single contact stimulation, the steering-DBS lead is indeed able to stimulate a significantly higher percentage of STN cells without activating any of the IC fibers compared to the CC lead. Especially in the case of a 1 mm displacement and the lead in optimal orientation, the steering-DBS lead outperforms the conventional lead. The current steering stimulation protocol shows that in case of a 1 mm displacement of the lead, where the single contact stimulation is performing weakly, dividing the stimulation current over two contacts opposing the IC can increase the percentage of activated STN cells. However, the results also show that correct placement and orientation of the lead within the target remains an important aspect for optimal stimulation outcome.

Using single contact stimulation at center and 1 mm off-center location, we found significantly different results in STN activation for the four orientations. The steering-DBS lead in its second and third orientation, which had an electrode contact in the opposite direction of the IC, the posterior-medial direction, was able to activate a significantly higher percentage of STN cells compared to the CC lead. The two other orientations did not have a steering electrode contact in opposite direction of the IC, which resulted in a less effective performance. Nevertheless, even in these two orientations the performances of the steering-DBS lead were never significantly worse than the CC lead and even at 1 mm off-center location the steering-DBS performed significantly better than the CC-lead while stimulating through the posterior contact (orientation 4).

The varied results that were obtained for the different orientations, illustrates a new challenge in correctly implanting the lead in the target. The lead contains a marker to verify the orientation of the lead by x-ray imaging. However, in order to make use of the full potential of the steering-DBS lead, the clinical effect of different orientations should be tested first during clinical trials. For this, computational models such as described in this study, can be a useful tool to gain more insight in the effect of the different orientations and finding the correct orientation. Finally, future studies should assess besides lead displacements also the rotation of the lead over time, and find ways to guarantee a fixed orientation of the lead.

One way to compensate for the orientation dependency of the steering-DBS lead is current steering stimulation. We showed that by balancing current across the medial and

posterior-lateral contact it is possible to increase the percentage of activated STN cells. This suggests that current steering enables stimulation in intermediate direction to a certain level. Unfortunately, stimulation through two contacts increases the active contact surface surrounding the lead, with which the selectivity of directional steering is reduced. This might explain why the current steering protocol is not performing better than stimulation through a cylindrical contact placed in the center of the STN. It should be noted that we presented the current steering separately from the single contact stimulation. In the clinic the current steering protocol will be an addition to the single contact stimulation protocol. This means a clinician will not use the current steering protocol in case single contact stimulation is already the optimal stimulation protocol, such as in second and third orientation. Secondly, only current-steering through the two adjacent contacts on the same row was tested to show the potential of an easy to interpret current steering protocol. More advanced current steering patterns with multiple contacts might enable more selective stimulation, such that similar percentages of STN cells are activated as those achieved by using a single contact in posterior-medial direction. Thirdly, it should be noted, more advantaged current steering patterns can also be performed with the CC lead. A previous modeling study, using similar methods, showed that the CC lead at the center of STN was able to activate 8% more STN cells using current steering with two independent sources than with monopolar stimulation [35]. This will level out the performances of the leads, especially at center location. However, with a 1 mm displacement the decrease in performance of the CC lead is considerably larger than the decrease in performance of the directional lead. This indicates that the directional lead, within the 1 mm window, is less sensitive to the displacement away from the optimal center location.

At the 2 mm off-center location, we found no difference between the CC lead and the steering-DBS lead. This was due to the fact that the optimal electrode contact for both leads was the same top cylindrical contact, C3 and C7. The steering-DBS lead has only two rows of electrode contacts along the lead which can be used for steered stimulation (C1-C6). In the 2 mm displacement scenario, the two rows of steering electrode contacts were shifted 1.32 mm ventrally and ended up too close to the ventrally located axon segments of the IC fibers. This scenario illustrates that with the limited amount of rows of steering electrode contacts it remains important to position the lead at the correct depth. In addition, the possible advantage of this steering-DBS lead is vulnerable to a displacement along the trajectory of the lead.

We decided to include the model representation of the steering-DBS lead in a well-described model of the subthalamic region that included many important and realistic details. The technical limitations of this computational model are comprehensively

described in previous studies, such as the large voxel size of the DTI dataset, and ignoring the capacitive behavior at the electrode-tissue interface [26, 42, 43]. In this specific study, the large voxel size of the DTI dataset had an effect on two aspects of the model. Firstly, the conductivity of the tissue in model was based on the DTI and this resulted in a low spatial resolution. Therefore, the anisotropy of small fiber bundles in the brain were not included in the model. Secondly, because of the low spatial resolution of the DTI dataset we were only able to trace the IC fibers and not the STN axons projecting to the pallidum. With respect to the capacitive behavior, in case of voltage controlled stimulation, the capacitive behavior of the electrode-tissue interface is important, especially for small contact surfaces area, because of its reduced electrode capacitance. However, while using current-controlled stimulation, similar to the one used in our current study, the electrode capacitance had negligible effects on the corresponding tissue voltage [28]. A previous study on a segmented lead with similar contact surface areas as the one in our model also showed that including this capacitive behavior in their model did not significantly change their results [31]. Finally, since our results focus on a comparison between the CC and HD leads in the same model, the limitations will influence both leads and therefore will have little impact on the comparison.

We should note that, in order to quantify the stimulation effect, we adopted the criterion that with DBS a maximum percentage of activated STN cells is needed while not stimulating the IC. Clinical research is needed to find more realistic and more detailed criterions. Therefore our criterion should only be regarded as an example to show the steering effect on a plausible target while steering away from a region causing side effects. Using this criterion also meant we did not pay attention to power consumption. We believed maximizing the effect of DBS is of greater importance than battery lifetime, especially now that rechargeable implantable pulse generators have become available [44, 45].

Because we used the same modelling procedure, we are able to compare the current results of the steering-DBS lead with a previously described 40 contact lead [34]. This shows that at center and 1 mm off-center location the steering-DBS lead with the option to steer the stimulation field in posterior-medial direction performed very similar as the 40 contact lead. However, at 2 mm off-center location the HD lead was able to perform significantly better (10%-11% more STN cells activated) than the CC lead, which was due to the fact that the dorsally located electrode contact of the 40 contact lead also can be used for steering. The previous study did not investigate different orientations of the 40 contact lead, however this lead is always able to stimulate in posterior-medial direction, and is therefore probably less sensitive to rotations of the lead.

Having only eight electrode contacts is a great advantage in programming the stimulation settings when monopolar stimulation is used. For a HD lead with a large number of electrode contacts programming the stimulation settings with a trial-and-error approach will not suffice in clinical practice [13]. For a 32 HD lead, which was used in a proof of concept study the test stimulation was limited to 4 standard steering directions, because of time constraints [46]. The eight channel lead has the advantage that it can be combined with a novel internal pulse generator, which includes eight independent current sources [11]. We used just a simple current steering stimulation protocol with two contacts, which already showed an improvement of the stimulation effect in certain cases. By selecting the appropriate current strength on each contact the steering properties of DBS can be improved even more [35], however, finding the correct current for each of the eight contacts will highly increase the complexity of programming the stimulation parameters. Thus, unless new technological tools will be developed to aid clinicians in selecting the optimal stimulation settings, the theoretical advantage of having many contacts or many current sources might not be fully utilized in practice. Creating patients specific models, by using the patients MRI/DTI dataset and using the same methodology as the current study, can be one of these tools. Patient specific models effectively have been used before to select stimulation settings, which maximize neural activation in a certain area [30]. Additionally, using the patient specific IC in the model can be used to warn the clinician to avoid certain settings. Besides running through all possible settings in an electric field model, more advanced techniques based on machine learning [31] and particles swarm optimization [47] can be the next step in finding the optimal settings in a time efficient way.

## Conclusion

In conclusion, we found that the concepts of steering the stimulation field with a steering-DBS lead with only 8 channels may be beneficial compared to the conventional lead, and it allows to correct for lead displacement errors of approximately 1 mm when it has the correct orientation or using current steering. While using single contact stimulation, which has the advantage of being easy to use in the clinic, our results illustrate the importance of the orientation of this lead. Therefore, sufficient attention should be paid to implanting the steering DBS-lead in the most effective orientation, and to keep this orientation of the lead over time.



## References

1. Deuschl G, Schade-Brittinger C, Krack P, et al. A Randomized Trial of Deep-Brain Stimulation for Parkinson's Disease. *New England Journal of Medicine* 2006; 355(9): p. 896-908.
2. Breit S, Schulz JB, and Benabid AL. Deep brain stimulation. *Cell Tissue Res* 2004; 318(1): p. 275-88.
3. Brown P. Oscillatory nature of human basal ganglia activity: relationship to the pathophysiology of Parkinson's disease. *Mov Disord* 2003; 18(4): p. 357-63.
4. Hariz M. Deep brain stimulation: new techniques. *Parkinsonism Relat Disord* 2014; 20 Suppl 1: p. S192-6.
5. Rossi PJ, Gunduz A, Judy J, et al. Proceedings of the Third Annual Deep Brain Stimulation Think Tank: A Review of Emerging Issues and Technologies. *Front Neurosci* 2016; 10: p. 119.
6. Tass PA. A model of desynchronizing deep brain stimulation with a demand-controlled coordinated reset of neural subpopulations. *Biol Cybern* 2003; 89(2): p. 81-8.
7. Tass PA, Qin L, Hauptmann C, et al. Coordinated reset has sustained aftereffects in Parkinsonian monkeys. *Ann Neurol* 2012; 72(5): p. 816-20.
8. Little S, Pogosyan A, Neal S, et al. Adaptive Deep Brain Stimulation in Advanced Parkinson Disease. *Annals of Neurology* 2013; 74(3): p. 449-457.
9. Rossi L, Foffani G, Marceglia S, and Priori A. Towards adaptive deep brain stimulation: Recording local field potentials during stimulation. *Movement Disorders* 2007; 22: p. S234-S234.
10. Rosin B, Slovik M, Mitelman R, et al. Closed-Loop Deep Brain Stimulation Is Superior in Ameliorating Parkinsonism. *Neuron* 2011; 72(2): p. 370-384.
11. Timmermann L, Jain R, Chen L, et al. Multiple-source current steering in subthalamic nucleus deep brain stimulation for Parkinson's disease (the VANTAGE study): a non-randomised, prospective, multicentre, open-label study. *Lancet Neurol* 2015; 14(7): p. 693-701.
12. Martens HC, Toader E, Decre MM, et al. Spatial steering of deep brain stimulation volumes using a novel lead design. *Clin Neurophysiol* 2011; 122(3): p. 558-66.
13. Willsie AC and Dorval AD. Computational Field Shaping for Deep Brain Stimulation With Thousands of Contacts in a Novel Electrode Geometry. *Neuromodulation* 2015; 18(7): p. 542-50; discussion 550-1.
14. Pollo C, Kaelin-Lang A, Oertel MF, et al. Directional deep brain stimulation: an intraoperative double-blind pilot study. *Brain* 2014; 137(Pt 7): p. 2015-26.
15. Hamel W, Fietzek U, Morsnowski A, et al. Deep brain stimulation of the subthalamic nucleus in Parkinson's disease: evaluation of active electrode contacts. *J Neurol Neurosurg Psychiatry* 2003; 74(8): p. 1036-46.
16. Okun MS, Tagliati M, Pourfar M, et al. Management of referred deep brain stimulation failures: a retrospective analysis from 2 movement disorders centers. *Arch Neurol* 2005; 62(8): p. 1250-5.
17. van den Munckhof P, Contarino MF, Bour LJ, Speelman JD, de Bie RM, and Schuurman PR. Postoperative curving and upward displacement of deep brain

- stimulation electrodes caused by brain shift. *Neurosurgery* 2010; 67(1): p. 49-53; discussion 53-4.
18. Contarino MF, Bot M, Speelman JD, et al. Postoperative displacement of deep brain stimulation electrodes related to lead-anchoring technique. *Neurosurgery* 2013; 73(4): p. 681-8; discussion 188.
19. Zylka W, Sabczynski J, and Schmitz G. A Gaussian approach for the calculation of the accuracy of stereotactic frame systems. *Medical Physics* 1999; 26(3): p. 381-391.
20. Fitzpatrick JM, Konrad PE, Nickele C, Cetinkaya E, and Kao C. Accuracy of customized miniature stereotactic platforms. *Stereotact Funct Neurosurg* 2005; 83(1): p. 25-31.
21. Hamani C, Saint-Cyr JA, Fraser J, Kaplitt M, and Lozano AM. The subthalamic nucleus in the context of movement disorders. *Brain* 2004; 127(Pt 1): p. 4-20.
22. Krack P, Fraix V, Mendes A, Benabid AL, and Pollak P. Postoperative management of subthalamic nucleus stimulation for Parkinson's disease. *Mov Disord* 2002; 17 Suppl 3: p. S188-97.
23. Steigerwald F, Muller L, Johannes S, Matthies C, and Volkmann J. Directional deep brain stimulation of the subthalamic nucleus: A pilot study using a novel neurostimulation device. *Mov Disord* 2016; 31(8): p. 1240-3.
24. Barbe MT, Maarouf M, Alesch F, and Timmermann L. Multiple source current steering--a novel deep brain stimulation concept for customized programming in a Parkinson's disease patient. *Parkinsonism Relat Disord* 2014; 20(4): p. 471-3.
25. Miocinovic S, Noecker AM, Maks CB, Butson CR, and McIntyre CC. Cicerone: stereotactic neurophysiological recording and deep brain stimulation electrode placement software system. *Acta Neurochir Suppl* 2007; 97(Pt 2): p. 561-7.
26. Chaturvedi A, Butson CR, Lempka SF, Cooper SE, and McIntyre CC. Patient-specific models of deep brain stimulation: influence of field model complexity on neural activation predictions. *Brain Stimul* 2010; 3(2): p. 65-7.
27. Astrom M, Lemaire JJ, and Wardell K. Influence of heterogeneous and anisotropic tissue conductivity on electric field distribution in deep brain stimulation. *Med Biol Eng Comput* 2012; 50(1): p. 23-32.
28. Butson CR and McIntyre CC. Tissue and electrode capacitance reduce neural activation volumes during deep brain stimulation. *Clin Neurophysiol* 2005; 116(10): p. 2490-500.
29. McIntyre CC, Mori S, Sherman DL, Thakor NV, and Vitek JL. Electric field and stimulating influence generated by deep brain stimulation of the subthalamic nucleus. *Clin Neurophysiol* 2004; 115(3): p. 589-95.
30. Frankemolle AM, Wu J, Noecker AM, et al. Reversing cognitive-motor impairments in Parkinson's disease patients using a computational modelling approach to deep brain stimulation programming. *Brain* 2010; 133(Pt 3): p. 746-61.
31. Teplitzky BA, Zitella LM, Xiao Y, and Johnson MD. Model-Based Comparison of Deep Brain Stimulation Array Functionality with Varying Number of Radial Electrodes and Machine Learning Feature Sets. *Front Comput Neurosci* 2016; 10: p. 58.

32. Alonso F, Latorre MA, Goransson N, Zsigmond P, and Wardell K. Investigation into Deep Brain Stimulation Lead Designs: A Patient-Specific Simulation Study. *Brain Sci* 2016; 6(3): p. 1-16.
33. Buhlmann J, Hofmann L, Tass PA, and Hauptmann C. Modeling of a segmented electrode for desynchronizing deep brain stimulation. *Front Neuroeng* 2011; 4: p. 15.
34. van Dijk KJ, Verhagen R, Chaturvedi A, et al. A novel lead design enables selective deep brain stimulation of neural populations in the subthalamic region. *J Neural Eng* 2015; 12(4): p. 046003.
35. Chaturvedi A, Foutz TJ, and McIntyre CC. Current steering to activate targeted neural pathways during deep brain stimulation of the subthalamic region. *Brain Stimul* 2012; 5(3): p. 369-77.
36. Butson CR and McIntyre CC. Current steering to control the volume of tissue activated during deep brain stimulation. *Brain Stimul* 2008; 1(1): p. 7-15.
37. Wakana S, Jiang H, Nagae-Poetscher LM, van Zijl PC, and Mori S. Fiber tract-based atlas of human white matter anatomy. *Radiology* 2004; 230(1): p. 77-87.
38. Tuch DS, Wedeen VJ, Dale AM, George JS, and Belliveau JW. Conductivity tensor mapping of the human brain using diffusion tensor MRI. *Proceedings of the National Academy of Sciences of the United States of America* 2001; 98(20): p. 11697-11701.
39. Hines ML and Carnevale NT. The NEURON simulation environment. *Neural Comput* 1997; 9(6): p. 1179-209.
40. Sato F, Parent M, Levesque M, and Parent A. Axonal branching pattern of neurons of the subthalamic nucleus in primates. *Journal of Comparative Neurology* 2000; 424(1): p. 142-152.
41. McIntyre CC, Richardson AG, and Grill WM. Modeling the excitability of mammalian nerve fibers: Influence of afterpotentials on the recovery cycle. *Journal of Neurophysiology* 2002; 87(2): p. 995-1006.
42. Butson CR, Cooper SE, Henderson JM, and McIntyre CC. Patient-specific analysis of the volume of tissue activated during deep brain stimulation. *Neuroimage* 2007; 34(2): p. 661-70.
43. Miocinovic S, Parent M, Butson CR, et al. Computational analysis of subthalamic nucleus and lenticular fasciculus activation during therapeutic deep brain stimulation. *J Neurophysiol* 2006; 96(3): p. 1569-80.
44. Waln O and Jimenez-Shahed J. Rechargeable deep brain stimulation implantable pulse generators in movement disorders: patient satisfaction and conversion parameters. *Neuromodulation* 2014; 17(5): p. 425-30; discussion 430.
45. Timmermann L, Schupbach M, Hertel F, et al. A new rechargeable device for deep brain stimulation: a prospective patient satisfaction survey. *Eur Neurol* 2013; 69(4): p. 193-9.
46. Contarino MF, Bour LJ, Verhagen R, et al. Directional steering: A novel approach to deep brain stimulation. *Neurology* 2014; 83(13): p. 1163-9.
47. Pena E, Zhang S, Deyo S, Xiao Y, and Johnson MD. Particle swarm optimization for programming deep brain stimulation arrays. *J Neural Eng* 2017; 14(1): p. 016014.



# Chapter 4

Spatial localization of sources in the rat subthalamic motor region using an inverse current source density method

*Based on:*

van Dijk, K. J., Janssen, M. L., Zwartjes, D. G., Temel, Y., Visser-Vandewalle, V., Veltink, P. H., ... & Heida, T. (2016). Spatial localization of sources in the rat subthalamic motor region using an inverse current source density method. *Frontiers in neural circuits*, 10, 87.

## Abstract

*Objective.* In this study we introduce the use of the current source density (CSD) method as a way to visualize the spatial organization of evoked responses in the rat subthalamic nucleus (STN) at fixed time stamps resulting from motor cortex stimulation. This method offers opportunities to visualize neuronal input and study the relation between the synaptic input and the neural output of neural populations.

*Approach.* Motor cortex evoked local field potentials and unit activity were measured in the subthalamic region, with a 3D measurement grid consisting of 320 measurement points and high spatial resolution. This allowed us to visualize the evoked synaptic input by estimating the current source density (CSD) from the measured local field potentials, using the inverse CSD method. At the same time, the neuronal output of the cells within the grid is assessed by calculating post stimulus time histograms.

*Main results.* The CSD method resulted in clear and distinguishable sources and sinks of the neuronal input activity in the STN after motor cortex stimulation. We showed that the center of the synaptic input of the STN from the motor cortex is located dorsal to the input from globus pallidus.

*Significance.* For the first time we have performed CSD analysis on motor cortex stimulation evoked LFP responses in the rat STN as a proof of principle. Our results suggest that the CSD method can be used to gain new insights into the spatial extent of synaptic pathways in brain structures.

## Introduction

In the last decades, technology for the recording of neuronal activity has advanced rapidly. Probes and microelectrode arrays have become available, which allow electrophysiological recordings with high temporal and spatial resolution [1-3]. In general, the recordings of neuronal activity can be divided into two components: the high frequency part of the potentials measured provide information about the spiking activity of neurons nearby, while the low-frequency part (the local field potential; LFP) contains information about how the dendrites process synaptic inputs [4]. The recorded potentials are dominated by a weighted sum of contributions from transmembrane currents through the membranes of the neurons nearby the electrode contacts [4]. Unfortunately, the large number of contributing sources makes the interpretation of the recordings complicated. Therefore, careful mathematical modeling and analysis are needed to take full advantage of the opportunities that such measurements offer in understanding the signal processing in neurons and neural circuits [5]. The development of methods for such modeling and signal analysis becomes even more pertinent with the on-going technological advancement. For example in the field of deep brain stimulation, novel stimulation lead designs [6, 7] allow LFP recordings on multiple locations within the region of interest to identify the stimulation target [8].

When grouped synaptic activity is sufficiently synchronized, it is often evident at the level of the LFP [9, 10]. By stimulating pre-synaptic neuronal populations, it is possible to evoke synchronized synaptic input in post-synaptic neuronal populations. The synaptic activation will cause an inflow of ions at the dendrites. For example, an inhibitory synaptic input using gamma-aminobutyric acid (GABA) as a neurotransmitter will cause an inflow of negatively charged Chloride ( $\text{Cl}^-$ ) ions at the dendrites. An excitatory synaptic input using glutamate as a neurotransmitter will cause an inflow of positively charged Sodium ( $\text{Na}^+$ ) and Potassium ( $\text{K}^+$ ) ions at the dendrites [11]. The ionic flow in and out of the extracellular medium caused by synaptic input can be described by the current source density (CSD) [5]. LFP recording with high spatial resolution microelectrode arrays allows us to estimate the CSD from the LFPs [9, 12-14]. With the CSD one can study the occurrence, spatial distribution and extent of the current sources and sinks of the synaptic input more locally. This offers opportunities to visualize neuronal input and study the relation between the synaptic input and the neural output, i.e. unit activity, of neural populations.

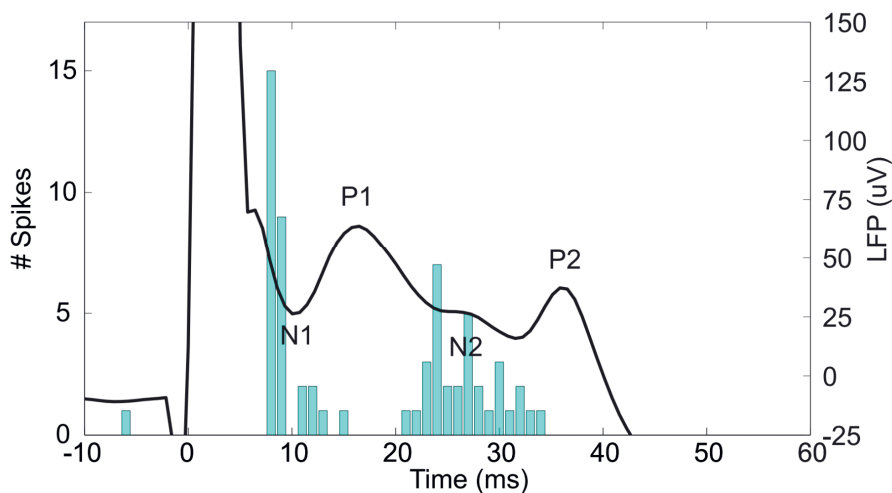


Figure 4-1, The evoked LFP and peristimulus time histogram (PSTH) of the unit activity in the STN after 600  $\mu$ A MCS. At 0 ms the stimulus is given. The negative deflections of the LFP, N1 and N2, are accompanied by an increased spiking rate as seen in the PSTH. In contrast, the positive deflections, P1 and P2, occurred concurrently with a decreased spiking rate in the PSTH.

The subthalamic nucleus (STN) is an important relay in the basal ganglia network as it is one of the main entry ports at which cortical input enters the basal ganglia and modulates the basal ganglia output structures [15, 16]. Cortical signals are conveyed to the STN by the monosynaptic cortico-subthalamic pathway, also known as the hyperdirect pathway, and the multisynaptic indirect pathway through the striatum and globus pallidus (GP). In response to motor cortex stimulation (MCS), STN neurons show a distinctive pattern of increased and decreased spike activity. The periods of increased spike activity are related to the excitation of the glutamatergic monosynaptic cortico-subthalamic pathway (N1, Figure 4-1) [17-22] and disinhibition via the indirect pathway (N2, Figure 4-1) [17, 20, 21]. In between an inhibitory period is present, which is believed to result from the GABAergic GP connections in the STN-GP-STN feedback loop (P1, Figure 4-1) [17, 19-21]. After the last excitation, a long-latency, long-duration inhibitory period follows (P2, Figure 4-1). Electrophysiological studies on cortically evoked subthalamic responses have thus far been focused on the temporal response of the unit activity and LFP on multiple locations within the STN [17, 19, 20, 22]. None of these studies visualized the spatial organization of the evoked response signal at fixed time stamps, such as the times of the incoming synaptic inputs.

In case of the STN, visualization of the spatial organization of synaptic inputs is important to study the segregation of synaptic pathways in the basal ganglia network and functional segregation in the STN. This is clinically relevant as deep brain stimulation of the STN has



shown to be an effective treatment for motor symptoms in patients with Parkinson's disease [23-26]. One of the major hurdles of this therapy is the occurrence of cognitive and limbic alterations in some of the treated patients [27, 28]. Many different approaches are explored to selectively target the STN motor region. High resolution imaging has been used to visualize the motor region [29], oscillations of neuronal activity [30] and subthalamic neuronal responses to motor cortex stimulation [31]. The CSD approach might provide more insight about the STN functional organization and the differences between unit activity and LFP. This tool might be used to further study cortico-subthalamic pathways in neurodegenerative diseases, which in the end could lead to further optimization of neuromodulative therapies in neurodegenerative diseases.

In this study, MCS evoked LFP and unit activities were simultaneously measured in the subthalamic region of the rat in a high spatial resolution three dimensional (3D) grid consisting 4x5x16 (antero-posterior x medio-lateral x dorso-ventral) measurement points, containing a volume of 200x100x1600  $\mu\text{m}$ . These measurements allowed us to perform CSD analysis at the times of the incoming synaptic inputs and to visualize the spatial organization of both components in the electrophysiological signals. The aim of this study was to show the strength of the CSD method to gain new insights into the spatial organization of synaptic pathways in brain structures, such as the clinically relevant STN. Furthermore, the aim was to investigate different cortico-subthalamic pathways, i.e. both the monosynaptic (hyperdirect) and multisynaptic (indirect) pathways and the STN-GP-STN feedback loop.

## Materials and Methods

### Experimental design

The experiments described in this paper were conducted on male Sprague Dawley rats (IFFA Credo, St Germain Sur l'Arbresle, France), weighing 250-400 g. Experiments were carried out according to the European Economic Community (86-6091 EEC) and the French National Committee (décret 87/848, Ministère de l'Agriculture et de la Forêt) guidelines for the care and use of laboratory animals and were approved by the Ethical Committee of Centre National de la Recherche Scientifique, Région Aquitaine-Limousin. In each rat, measurements were performed in the right hemisphere. The rats were anesthetized with urethane hydrochloride (1.2 g/kg, i.p. injections, Sigma-Aldrich, Saint-Quentin Fallavier, France) and fixed in a stereotactic frame (Horsley Clarke apparatus, Unimécanique, Epinay sur Seine, France). Body temperature was monitored with a rectal probe and maintained at 37 °C with a homeothermic warming blanket (model 50-7061, Harvard Apparatus, Les Ulis, France). Burr holes in the skull were made above the stimulation and recording sites. A saline solution was applied on all exposed cortical areas

to prevent dehydration. The microelectrode probe with 16 contacts was used to perform the electrophysiological recordings (A1x16-10mm-100-703-A16, Neuronexus, Ann Arbor, USA). Each contact on the probe has a contact area of  $703\ \mu\text{m}^2$ , and  $100\ \mu\text{m}$  inter-electrode distance. The probe was lowered into the brain towards the STN using a microdrive (Microcontroller ESP 300, Newport, Evry, France). Stereotactic coordinates in mm relative to Bregma were: AP  $-3.8$ , ML  $\pm 2.5$ , DV  $-8.0$  [32].

When the electrode was in place, the stimulation session started. Recordings of both the unit activity at a sample rate of  $22321\ \text{Hz}$  and the LFPs at a sample rate of  $1395\ \text{Hz}$  were performed concurrently with cortical stimulation using the AlphaLab SnR system (AlphaOmega, Nazareth, Israel). After a baseline recording of 2 minutes, 99 stimuli with an amplitude of  $300\ \mu\text{A}$  and 99 stimuli with an amplitude of  $600\ \mu\text{A}$  were given. The forelimb region of the motor cortex (coordinates in mm relative to the bregma: AP  $+3.2$ , ML  $\pm 4.0$ , DV  $-2.6$ ) was stimulated with  $0.3\ \text{ms}$  pulse width and  $1.1\ \text{Hz}$  frequency ipsilateral to the recording site with two concentric bipolar electrodes [33]. Electrical stimuli were generated with an isolated stimulator (DS3, Digitimer Ltd., Hertfordshire, UK) triggered by the AlphaLab SnR (AlphaOmega, Nazareth, Israel). Stimulation electrode localization was confirmed histologically.

After the first stimulation session, the recording probe was retrieved and inserted again at the same depth, but shifted  $200\ \mu\text{m}$  in medio-lateral or antero-posterior direction. This was repeated to obtain a total of 20 trajectories, five in medio-lateral direction and four in antero-posterior direction. As the probe consisted of 16 electrode contacts, a 3D measurement grid of  $4 \times 5 \times 16$  (antero-posterior  $\times$  medio-lateral  $\times$  dorso-ventral) was achieved (Figures 4-2a). Traces of the electrodes along the trajectories have been verified histologically (Figure 4-2b). Only data from rats in which the traces had been within the STN and in which clear triphasic responses were seen were analyzed, resulting in a total data set from 4 rats. The absolute coordinates of the electrode trajectories with respect to the STN were unfortunately not retrievable.

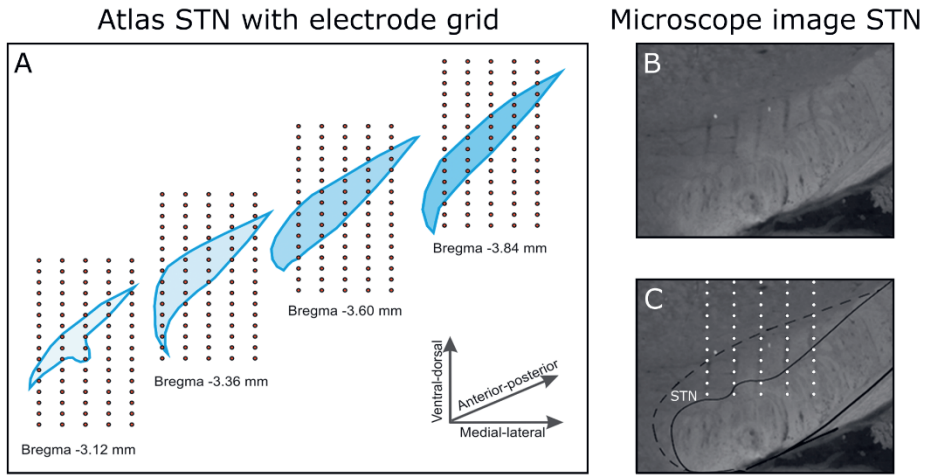


Figure 4-2, (A) The 3D electrode grid inside four coronal STN slices (bregma -3.1 to -3.8 mm in the antero-posterior direction). In total, this gives a 4x5x16 grid (antero-posterior x medio-lateral x dorso-ventral). Note that the four illustrated slices are 0.24 mm apart, in reality the measurements were performed 0.2 mm apart. (B) A selection of a microscope image of a coronal brain slice (Anterior-posterior -3.8 mm relative to Bregma). (C) In the brain slice, the electrode trajectories are visible within the STN.

### Unit activity analysis.

The recorded evoked unit activity was visualized by post stimulus time histograms (PSTHs). These histograms were used to visualize the rate and timing of neuronal spike discharges in relation to an external stimulus. PSTHs were generated by using an envelope spike detection method [34]. Peaks above the threshold, mean  $\pm$  3 times the standard deviation (SD), were marked as spikes and principal components analyses were used to classify the waveforms of the detected spikes [35]. From the classification of the waveforms, the first and second principal components were used for Bayesian clustering, which practices probability density function (Gaussian mixture model) and expectation maximization. Spikes were bin sized at 1ms. Unit activity was amplitude significant by a threshold of  $\pm$  3 times the SD based on 100 ms PSTH's of preceding stimulation.

### LFP analysis

First, we checked the channels for high level of noise. If the power between 2 and 200 Hz of the signal during baseline recording exceeded 10 times the average power of all baseline recordings in that particular rat, the measurements at that grid point were rejected. In that case, the average LFP responses of the surrounding grid points were used to interpolate the LFP on the rejected channel. Second, the signals were divided into epochs of 100 ms before stimulation until 500 ms after stimulation. The offset for each epoch was filtered out of the signal using a second order high-pass non-causal Butterworth filter with a cut-

off frequency of 1 Hz. All epochs were checked for artifacts; an artifact was detected if the absolute signal in the epoch exceeded 400  $\mu\text{V}$  (note that the signal during the stimulation artifact, from 0 ms to +7 ms relatively to the trigger, was excluded from this criterion). Epochs containing artefacts were rejected. The remaining epochs of the 99 stimuli were averaged per grid point per stimulation type. Subsequently, this average LFP response was smoothed over time and space in dorso-ventral direction, using a third order Savitzky–Golay filter with a window size of 9 samples [36]. We only spatially filtered in one axes, because of the lower spatial resolution and smaller range of measurement points in antero-posterior and medio-lateral axes.

## CSD analysis

To estimate the CSD distribution we used the inverse Current Source Density (iCSD) method. The method has been described for one dimensional recordings by Pettersen et al. [13] and has been generalized to three-dimensional recordings by Łęski et al. [14]. The iCSD method is based on linear inversion of the electrostatic forward solution. In the iCSD method, the CSD is assumed to have a certain known distribution class. The distribution class should be parameterized with as many parameters as the number of recorded signals. By using the electrostatic forward solution one can find a linear relation  $F$  between the CSD distribution and the LFP generated by the CSD on the electrode locations (Equation 1). The linear relation can be used to solve the inverse problem by using the inverse of  $F$  to calculate the CSD distribution from the recorded LFP signals (Equation 2).

$$\overline{LFP} = F \cdot \overline{CSD} \quad (1)$$

$$\overline{CSD} = F^{-1} \cdot \overline{LFP} \quad (2)$$

With  $\overline{LFP}$  the LFP vector ( $\overline{LFP}$  in  $\mathbf{R}^{320}$ ),  $\overline{CSD}$  the CSD vector ( $\overline{CSD}$  in  $\mathbf{R}^{320}$ ) and  $F$  the iCSD transformation matrix. The LFP vector consists of 320 cortically evoked LFPs corresponding to the number of grid points. To describe the CSD distribution we used the natural spline iCSD in which the CSD values within the grid are obtained using natural spline interpolation [14]. As this approach assumes all sources to be within the measurement grid, an additional boundary condition was introduced. This boundary condition extends the CSD distribution with one layer beyond the original grid, with the grid points in the outer layer having the same value as the nearest CSD value [14]. Next, the calculated CSD distribution was used to investigate the fast CSD sources and sinks caused by evoked synaptic input from the cortex and GP in the STN. For this, we high-pass filtered the CSD using a second order high-pass non-causal Butterworth filter with a cut-off frequency of 50 Hz. Finally, to determine whether these sources and sinks were of significant amplitude, we used the CSD of 100 ms preceding stimulation and

determined the threshold as the mean of this signal  $\pm 3$  times the SD. When sources and sinks were above or below this threshold, they were considered significant.

### Localization of MCS evoked synaptic activity

For each rat the CSD and PSTH distribution in 3D were evaluated at the points in time at which N1, P1 and N2 occur (Figure 4-1). At the instant of N1 the excitatory synaptic input will cause an inflow of positively charged ions at the dendrites, which results in negative values in the CSD distribution (sinks). To find the center of the excitatory synaptic pathway in the STN we calculated the center of mass (CoM) of the significant sinks in the evoked CSD distribution at time of N1 (Equation 3-5). At the instant of P1 the inhibitory synaptic input will cause an inflow of negatively charged ions at the dendrites, which results in positive values in the CSD distribution (sources). To find the center of the incoming inhibitory synaptic pathway in the STN we calculated the CoM of the significant sources in the evoked CSD distribution at time of P1 (Equation 3-5).

$$C_x = \frac{\sum x \cdot f(x,y,z)}{\sum f(x,y,z)}, C_y = \frac{\sum y \cdot f(x,y,z)}{\sum f(x,y,z)}, C_z = \frac{\sum z \cdot f(x,y,z)}{\sum f(x,y,z)} \quad (3-5)$$

With C the CoM, x,y and z the coordinates within the measurement grid on the, antero-posterior, medio-lateral and dorso-ventral axis respectively,  $\sum$  a 3D summation over the measurement grid, and  $f(x,y,z)$  contains the significant CSD sinks, the significant CSD sources, or the significant PSTH values within the measurement grid.

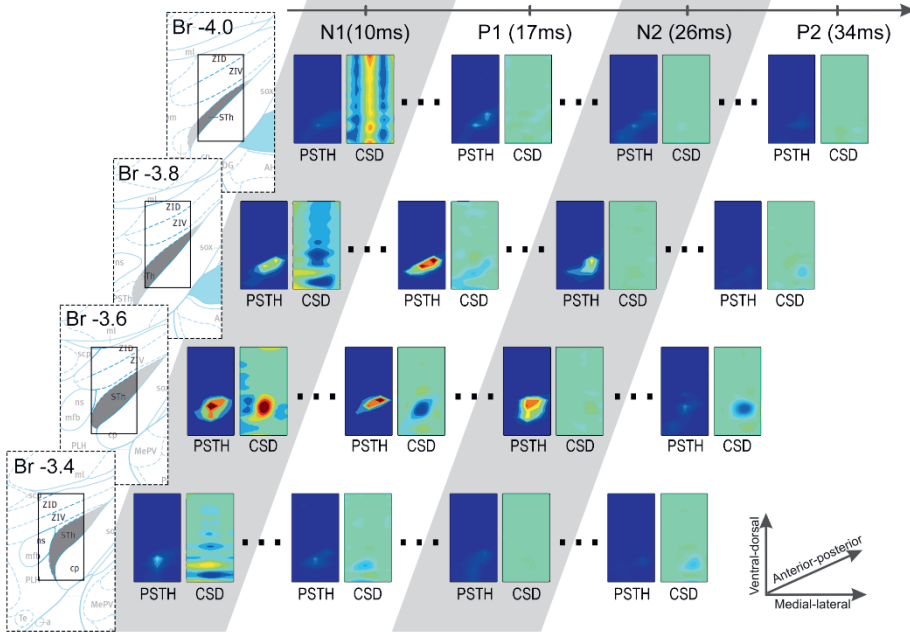
For each rat we assessed the location of the incoming excitatory and inhibitory synaptic input relatively to the center of the responsive STN cells, i.e. the CoM of the PSTH at time of N1 (Equation 3-5). Also, we assessed the locations of the CoM of the PSTH at N1 and N2, relatively to the center of the excitatory synaptic input at time of N1. A one-way analyses of variance (ANOVA) with post hoc multiple comparison procedure, using a Bonferroni adjustment to compensate for multiple comparisons with a significance level of 0.05, was used to check whether the CoM of the inhibitory and excitatory synaptic input were situated significantly different from each other and from the center of the responsive cells. A paired two tailed t-test with a significant level of 0.05 was used to check whether the CoM of the PSTH distribution at time of N1 and N2 were located differently from each other, along the dorso-ventral, antero-posterior, and medio-lateral axis.

## Results

We first focus on the results obtained during 600  $\mu$ A MCS (Figure 4-3). The CSD and unit activity were evaluated for 4 rats at the points in time at which N1, P1, N2 and P2 occur. At the time of N1, the CSD distribution showed a clear local sink corresponding to an

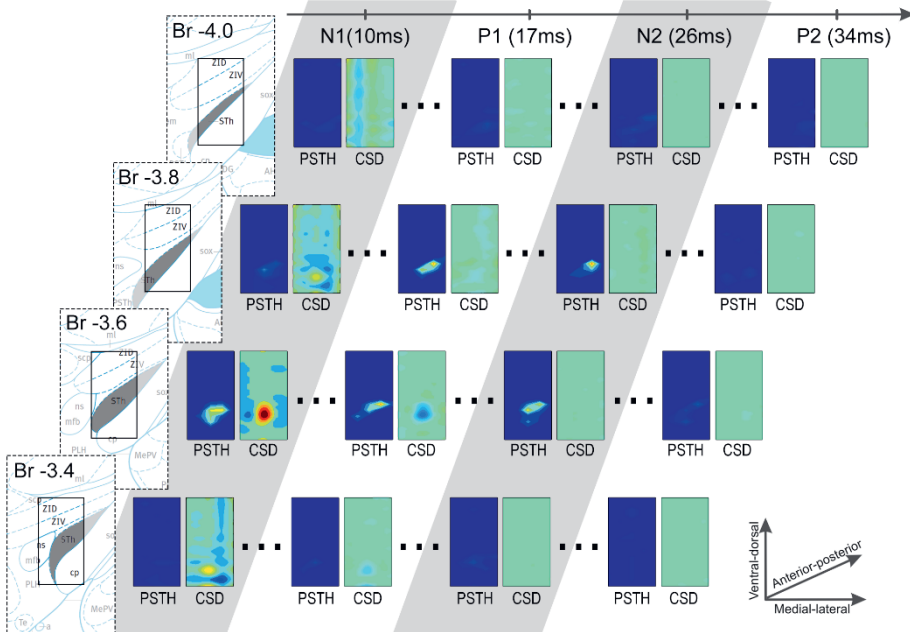
## Motor cortex stimulation 600 $\mu$ A

Spatial distribution of evoked neural activity



## Motor cortex stimulation 300 $\mu$ A

Spatial distribution of evoked neural activity



← Figure 4-3, Representative examples of 600  $\mu$ A and 300  $\mu$ A MCS evoked CSD and PSTH distributions are shown. The four rows contain coronal slices (bregma -3.4 to -4.0 mm). Each row contain, from left to right: first an image of the brain atlas. The atlas is for visualization purposes only, the STN is denoted in gray and the small rectangle is the size of our measurement grid (0.8 mm x 1.5 mm). We used the coronal atlas slices closest to the measurement grid, i.e. bregma -3.36, -3.60, -3.84, and -3.96. Second, the PSTH and CSD distribution at the time of P1, N1, P2 and N2. Only significantly increased spiking rates are shown in the PSTH distributions, and only sinks (red) and sources (blue) with significant strength are shown in the CSD distributions. The x-axis of each rectangle ranges from most medial recording (bregma 2.1 mm) to the most lateral recording (bregma 2.9mm). The y-axis of each rectangle ranges from most ventral recording to the most dorsal recording.

excitatory synaptic input, represented by a red area. In the unit activity a locally increased spiking rate can be seen within the grid, also represented by a red area. At the time of P1 the CSD shows a clear local source, represented by a blue area, corresponding to an inhibitory synaptic input near the previously spiking neurons. In the unit activity the spiking rates were reduced. At the time of N2 a locally increased spiking rate can be seen, however no clear sources or sinks were present in the CSD. Finally, at the time of P2 the spiking rate is reduced through the whole area and the CSD showed local source corresponding to an inhibitory synaptic input near the previously spiking neurons. In two rats, during 300  $\mu$ A MCS, the response was similar as the 600  $\mu$ A MCS, however the sinks and sources became weaker (Figure 4-3). The sources at P1 and P2 reduced in strength more dramatically than the sink at N1. In the other two rats the 300  $\mu$ A MCS did not evoke a similar response.

Furthermore, we computed the center of the excitatory and inhibitory synaptic pathways (Figure 4-4). During 600  $\mu$ A MCS, the CoM of the CSD sinks at time of N1 was located  $26 \pm 49$   $\mu$ m anterior,  $1 \pm 91$   $\mu$ m medial, and  $153 \pm 105$   $\mu$ m dorsal of the center of the responsive STN cells. The CoM of the CSD sources at time of P1 was located  $25 \pm 107$   $\mu$ m anterior,  $75 \pm 76$   $\mu$ m medial, and  $134 \pm 172$   $\mu$ m ventral of the center of the responsive STN cells. The CoM of the excitatory and inhibitory synaptic inputs were not located significantly different from the center of the responsive cells, however they were located significantly different from each other in the dorsoventral ( $p < 0.01$ ). During 300  $\mu$ A MCS, the CoM of the CSD sinks at time of N1 was located  $44 \pm 46$   $\mu$ m anterior,  $11 \pm 90$   $\mu$ m medial, and  $167 \pm 66$   $\mu$ m dorsal of the center of the responsive STN cells. The CoM of the CSD sources at time of P1 was located  $7 \pm 115$   $\mu$ m anterior,  $34 \pm 104$   $\mu$ m medial, and  $135 \pm 142$   $\mu$ m ventral of the center of the responsive STN cells. The CoM of the excitatory and inhibitory synaptic inputs were not located significantly different from the center of the responsive cells, however they were located significantly different from each other in the dorsoventral axis ( $p < 0.01$ ).

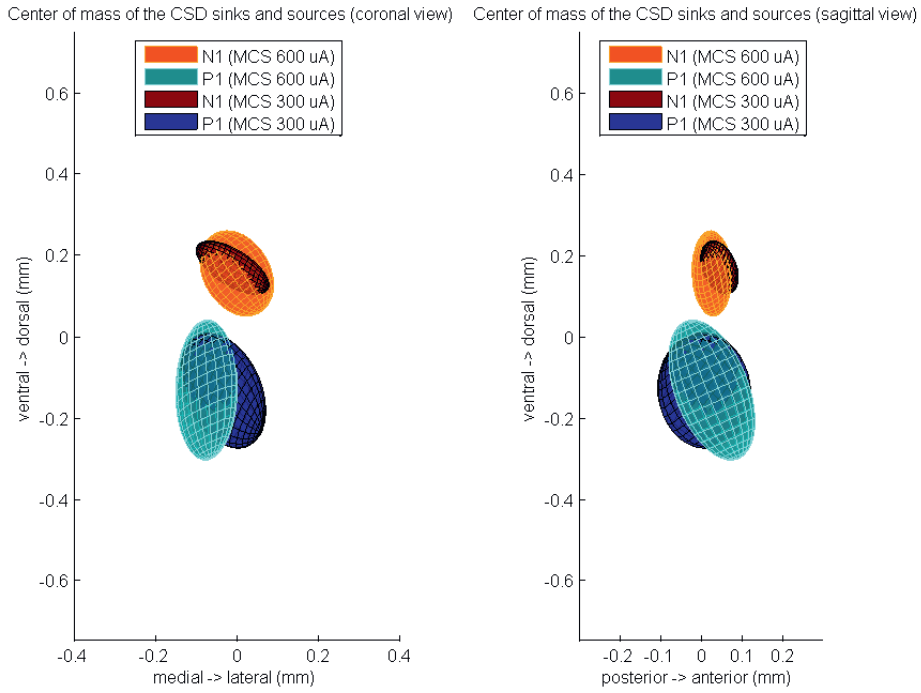


Figure 4-4, The averaged center of mass locations of the CSD sources at time of P1 and the CSD sinks at time of N1, relatively to the center of mass of the evoked unit activity at time of N1. These relative center locations are averaged over all rats which showed a MCS response and is visualized by a color-coded Gaussian ellipsoid. The centroid of the ellipsoid is located on the mean center of mass location and the width of the centroid is the covariance of the center of mass coordinates.

Finally, we computed the CoM of the unit response during N1 and N2 (Figure 4-5). During 600  $\mu$ A MCS, the CoM of the PSTH distribution at time of N1 was located  $26 \pm 49$   $\mu$ m posterior,  $1 \pm 91$   $\mu$ m lateral, and  $153 \pm 105$   $\mu$ m ventral of the CoM of the excitatory synaptic input. The CoM of the unit activity at time of N2 was located  $13 \pm 76$   $\mu$ m posterior,  $34 \pm 38$   $\mu$ m lateral, and  $235 \pm 157$   $\mu$ m ventral of the CoM of the excitatory synaptic input. During 300  $\mu$ A MCS, the CoM of the PSTH distribution at time of N1 was located  $44 \pm 46$   $\mu$ m posterior,  $11 \pm 90$   $\mu$ m lateral, and  $167 \pm 66$   $\mu$ m ventral of the CoM of the excitatory synaptic input. The CoM of the PSTH distribution at time of N2 was located  $80 \pm 69$   $\mu$ m posterior,  $54 \pm 71$   $\mu$ m lateral, and  $188 \pm 233$   $\mu$ m ventral of the CoM of the excitatory synaptic input. For both stimulation strengths, the CoM of the unit activity at N1 and N2 were not significantly different on any of the three axes.



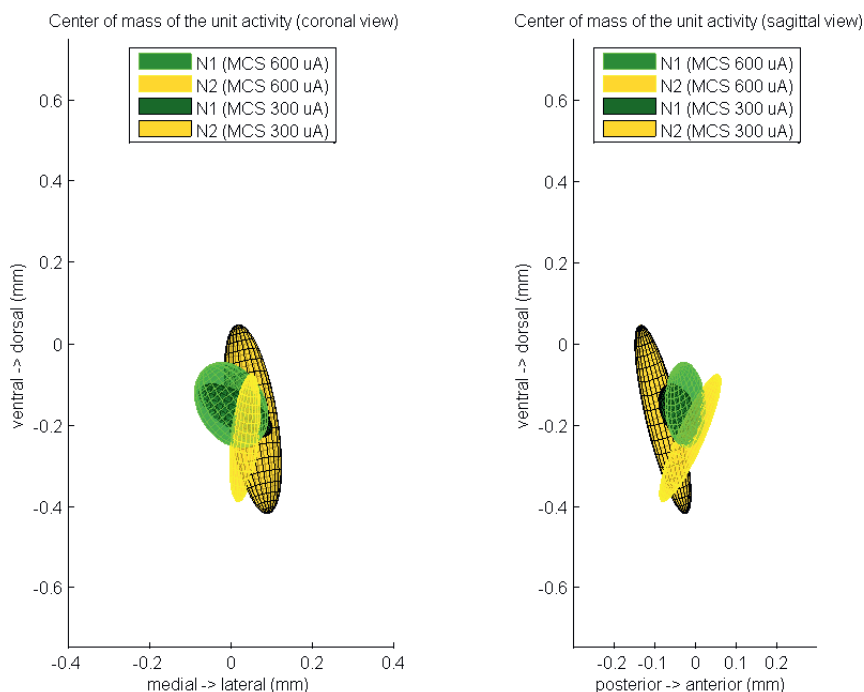


Figure 4-5, The averaged center of mass locations of the unit activity at time of N1 and at time of N2, relatively to the center of mass of the evoked CSD source at time of N1. These relative center locations are averaged over all rats which showed a MCS response and is visualized by a color-coded Gaussian ellipsoid. The centroid of the ellipsoid is located on the mean center of mass location and the width of the centroid is the covariance of the center of mass coordinates.

## Discussion

In this study, LFP and unit activities were simultaneously measured in the subthalamic region with a carefully constructed high resolution measurement grid. For the first time we have performed CSD analysis on MCS evoked LFP responses in the rat STN.

### Interpretation of the MCS evoked response

Previous studies showed that STN neurons display a distinctive temporal pattern of increased and decreased spike activity after cortex stimulation [17, 19, 20, 22]. The first increased spike activity is due to activation of the glutamatergic monosynaptic cortico-subthalamic pathway. An excitatory synaptic input using glutamate as a neurotransmitter will cause an inflow of positively charged  $\text{Na}^+$  and  $\text{K}^+$  ions at the dendrites [11]. Our 3D CSD visualization shows, at the time of this incoming pathway (N1), the inflow of positively charged particles as a strong local current sink within the measurement grid.

As expected, the excitatory synaptic input causes an increase of the unit activity within the measurement grid. In addition, the location of the CoM of the excitatory synaptic input was not significantly different than the location of the responsive cells. Intracellular labeling of rat STN neurons shows the dendritic fields are ellipsoidal shaped surrounding the soma[37], therefore synaptic currents at the dendrites and firing at the soma should be approximately the same location along the different axis.

The inhibitory period which follows is a result of the GABAergic input from GP connections involved in the STN-GP-STN feedback loop [17, 19-21]. An inhibitory GABA synaptic input will cause an inflow of negatively charged Cl<sup>-</sup> ions at the dendrites. The 3D visualization shows, at the time of this incoming pathway (P1), the inflow of negatively charged particles as a strong local current source within the measurement grid. At the same time, a decrease of spiking activity of the excited STN cells was observed. However, in the example CSD (Figure 4-3) some of the dorsally located STN cells were not affected by the inhibitory synaptic input. This suggests the local subset of STN cells, which were affected by the excitatory input, triggered the STN-GP-STN feedback loop. However, the evoked inhibition from GP did not cover the complete local subset of STN cells. This finding also corresponds with the computed CoM of sources and sinks in the CSD distribution at the time of N1 and P1.

The CoM of the inhibitory synaptic input from GP was located significantly more ventral than the excitatory input from the cortex. Retrograde and anterograde labeling studies concerning afferent pathways of the rat STN showed that projections from the cerebral cortex were distributed extensively over the STN in only a coarse topographic manner [38, 39]. In animals with clear topographic organization, such as macaque monkeys, however, the projections from the motor areas appear to be confined to the dorsolateral part of the STN [40]. The afferent connections that are involved in the STN-GP-STN feedback loop are suggested to be more precisely organized [38]. Anterograde tract-tracing from the GP demonstrated that after deposit of biotinylated dextran amine in the GP, the site of terminal labeling tended to be denser in the ventral border of the STN [41]. Another anterograde study using horseradish peroxidase showed that a dense terminal field of GP origin was located in the ventral part of the STN, although it gradually moved more dorsally at the caudal level [38].

After the inhibitory period the spike-rate goes back up at time of N2, due to disinhibition of STN through inhibition of GP by the indirect pathway [17]. This corresponds to our results. The 3D PSTH distribution showed a local increase of the spike rate. The CSD distribution did not show sources and sinks, meaning that the increase in spike rate is a result of disinhibition and not a result of synaptic input.

The source of the long-latency, long-duration inhibitory period, P2, is thought to result from cortical depression. In our example it looks like that P2 is located in the same area as P1. As P1 is caused by an inhibitory input from the GP, this suggests that P2 is also caused by an inhibitory input from the GP. Also, when comparing the results obtained with 300  $\mu\text{A}$  to those obtained with 600  $\mu\text{A}$  MCS, it is evident that both the area and the amplitude of the source of P2 are reduced more drastically than the sink of N1. This could be explained by the fact that P2 occurred after multiple synaptic stations and thus required temporal-spatial summation to be effective. In contrast, N1 is caused by the monosynaptic cortico-subthalamic pathway.

### The iCSD method

To perform the iCSD method, the responses in the 3D grid have to be measured simultaneously. Our measurements were performed in multiple trials, but by averaging the responses of 99 stimuli; by making sure that the stimulation electrode was not moved during the experiments, we assumed that the responses were very similar to what would have been measured if all the points in the 3D grid were measured simultaneously. The same assumption was made by Łęski et al. [14] to test the iCSD method and they were able to estimate plausible CSD distributions from evoked LFPs. Unfortunately, it is possible that tissue will get damaged due to consecutively inserting the measurement electrode in a small nucleus such as the STN. Remarkably, we kept measuring good quality multiphasic unit activity responses after many consecutive insertions of the measurement electrode.

There are other problems, which complicate the reconstruction of the CSD. The method assumes homogenous isotropic volume conduction of the tissue. The STN is surrounded by myelinated axon bundles [42], which have different conductivities and are highly anisotropic [43-45]. Besides, as shown in the microscope image of the STN (Figure 4-2b) the trajectories of the lead can be seen in the tissue. These trajectories also introduce heterogeneous volume conduction in the tissue when they fill up with cerebral fluid. The cerebral fluid has a high conductivity relative to brain tissue [45], the opposite goes for the lead carrying the 16 measurement contacts. The low conductivity of the lead will shield off one side of the measurement electrode.

Finally, in the rats without LFP response, misplacement of either the stimulation or the recording electrode could have occurred. The placing of the recording electrode was checked and confirmed, so misplacement of the recording electrode was not the case. Wearing and tearing of the recording electrode due to blood clotting and cleaning probably affected the impedance of the electrode, which resulted in a decreased signal to noise ratio and also variation in the signal acquisition per measurement point. The iCSD

method assumes the exact same signal acquisition for each of the 320 measurement points. When this is not the case, it will result in overfitting of the CSD distribution on the measured signals. Therefore, we included several filtering steps, including spatial as well as temporal filtering, to get a smooth LFP distribution before we used the iCSD method to estimate the CSD distribution.

The iCSD method enables compensation of signal acquisition errors and false assumptions on tissue and electrode impedances, when you know its effect on the measured LFP, by including it in the construction of matrix  $F$  (Equation 1). Also, instead of using the iCSD method it is possible to use more advanced CSD methods such as the kernel CSD method [46]. This method is based on reproducing kernel Hilbert space and includes cross-validation and ridge regression that address the problem of noise in the data. This method is harder to interpret than a linear method and you have to make new assumption on the size of the sources and sinks.

Despite the problems we addressed, we believe that with a reasonable set of recordings at different sites the CSD reconstruction may provide the basic understanding of different incoming synaptic pathways in a brain structure such as the STN. In contrast to conventional retrograde and anterograde labeling methods, the CSD method allows us to perform *in vivo* experiments without sacrifice of the animal to study synaptic pathways.

## Validity of the results

It should be noted that this study with 4 rats is a proof of principal of the CSD method. The aim of this study was to show the strength of the visualization methods to investigate the spatial organization of both components in the electrophysiological signals. For this, we included only rats with LFPs and unit activity responses similar to those described in earlier reports [17]. This approach allowed us to use the knowledge from the well described temporal behavior of the evoked response to explain the evoked spatial distributions of the evoked CSD. Our results are well in line with these previous studies, however to gain new insights into the synaptic pathways to the STN and topology of the STN cells, more electrophysiological data needs to be acquired in future studies.

## Future clinical prospects

MCS and simultaneous measurements of the subthalamic response has been performed in PD patients in order to locate the motor area of the STN[31, 47]. The method presented in this paper was able to distinguish the different sources and sinks of the neuronal input in the STN. Novel DBS electrode design are presented, which is capable of high resolution stimulation and recording in different directions [6-8]. In the future this new electrode design enables the CSD approach. The sources and sinks resulting from the CSD approach

could be used to optimize the target location for the DBS electrode. In that regard, it has to be determined which location relative to these sources and sinks provides the optimal clinical benefit for the patient. In future, this new approach enables a more precise localization of the STN motor area and could improve surgical outcomes of DBS for PD.

## Conclusion

In this study, we used CSD analysis in the rat to determine the sources and sinks of neuronal input in the STN after cortical stimulation. The CSD method resulted in clear and distinguishable localization of sources and sinks of the neuronal input activity in the STN after MCS. Finally, we showed that the center of the synaptic input of the STN from the MC is located dorsal to the input from GP.

## References

1. Buzsáki, G., *Large-scale recording of neuronal ensembles*. Nat. Neurosci., 2004. 7(5): p. 446-451.
2. Du, J.G., et al., *Multiplexed, High Density Electrophysiology with Nanofabricated Neural Probes*. Plos One, 2011. 6(10).
3. Kipke, D.R., et al., *Advanced Neurotechnologies for Chronic Neural Interfaces: New Horizons and Clinical Opportunities*. Journal of Neuroscience, 2008. 28(46): p. 11830-11838.
4. Buzsáki, G., C.A. Anastassiou, and C. Koch, *The origin of extracellular fields and currents — EEG, ECoG, LFP and spikes*. Nat Rev Neurosci, 2012. 13(6): p. 407-420.
5. Einevoll, G.T., et al., *Modelling and analysis of local field potentials for studying the function of cortical circuits*. Nat Rev Neurosci, 2013. 14(11): p. 770-785.
6. Martens, H.C., et al., *Spatial steering of deep brain stimulation volumes using a novel lead design*. Clin Neurophysiol, 2011. 122(3): p. 558-66.
7. Bour, L.J., et al., *Directional Recording of Subthalamic Spectral Power Densities in Parkinson's Disease and the Effect of Steering Deep Brain Stimulation*. Brain Stimul, 2015. 8(4): p. 730-41.
8. Mitzdorf, U., *Current Source-Density method and application in cat cerebral cortex Investigation of evoked potentials and EEG phenomena*. Physiol. Rev., 1985. 65(1): p. 37-100.
9. Hubbard, J.I., R.R. Llinás, and D.M. Quastel, *Electrophysiological analysis of synaptic transmission*. 1969: Williams & Wilkins Company.
10. Purves, D., *Neuroscience*. 4th ed. 2008, Sunderland, Mass.: Sinauer. xvii, 857, G-16, IC-7, I-29 p.
11. Freeman, J.A. and C. Nicholson, *Experimental optimization of current source-density technique for anuran cerebellum*. J Neurophysiol, 1975. 38(2): p. 369-82.
12. Pettersen, K.H., et al., *Current-source density estimation based on inversion of electrostatic forward solution: effects of finite extent of neuronal activity and conductivity discontinuities*. J Neurosci Methods, 2006. 154(1-2): p. 116-33.

13. Leski, S., et al., *Inverse current-source density method in 3D: reconstruction fidelity, boundary effects, and influence of distant sources*. Neuroinformatics, 2007. 5(4): p. 207-22.
14. Nambu, A., H. Tokuno, and M. Takada, *Functional significance of the cortico-subthalamo-pallidal 'hyperdirect' pathway*. Neurosci. Res., 2002. 43: p. 111-117.
15. Parent, A. and L.N. Hazrati, *Functional anatomy of the basal ganglia. II. The place of subthalamic nucleus and external pallidum in basal ganglia circuitry*. Brain Res Brain Res Rev, 1995. 20(1): p. 128-54.
16. Magill, P.J., et al., *Synchronous unit activity and local field potentials evoked in the subthalamic nucleus by cortical stimulation*. J. Neurophysiol., 2004. 92: p. 700-714.
17. Kitai, S.T. and J.M. Deniau, *Cortical inputs to the subthalamus: intracellular analysis*. Brain Res., 1981. 214(2): p. 411-415.
18. Fujimoto, K. and H. Kita, *Response characteristics of subthalamic neurons to the stimulation of the sensorimotor cortex in the rat*. Brain Res., 1993. 609: p. 185-192.
19. Maurice, N., et al., *Relationships between the prefrontal cortex and the basal ganglia in the rat Physiology of the corticosubthalamic circuits*. J. Neurosci., 1998. 18(22): p. 9539-9546.
20. Nambu, A., et al., *Excitatory cortical inputs to pallidal neurons via the subthalamic nucleus in the monkey*. J. Neurophysiol., 2000. 84: p. 289-300.
21. Kolomiets, B.P., et al., *Segregation and Convergence of Information Flow through the Cortico-Subthalamic Pathways*. J. Neurosci., 2001. 21(15): p. 5764-5772.
22. Paxinos, G. and C. Watson, *The rat brain in stereotaxic coordinates*. 1998, New York: Academic Press.
23. Tan, S.K.H., et al., *Experimental deep brain stimulation in animal models*. Neurosurgery, 2010. 67(4): p. 1073-1080.
24. Dolan, K., et al., *Automatic noise-level detection for extra-cellular micro-electrode recordings*. Med Biol Eng Comput, 2009. 47(7): p. 791-800.
25. Lewicki, M.S., *A review of methods for spike sorting: the detection and classification of neural action potentials*. Network, 1998. 9(4): p. R53-78.
26. Savitzky, A. and M.J. Golay, *Smoothing and differentiation of data by simplified least squares procedures*. Anal Chem, 1964. 36(8): p. 1627-1639.
27. Hamani, C., et al., *The subthalamic nucleus in the context of movement disorders*. Brain, 2004. 127(Pt 1): p. 4-20.
28. Nicholson, P.W., *Specific impedance of cerebral white matter*. Exp Neurol, 1965. 13(4): p. 386-401.
29. Hauelsen, J., et al., *The influence of brain tissue anisotropy on human EEG and MEG*. Neuroimage, 2002. 15(1): p. 159-66.
30. Andreuccetti, D., R. Fossi, and C. Petrucci, *An Internet resource for the calculation of the dielectric properties of body tissues in the frequency range 10 Hz - 100 GHz*. Website at <http://niremf.ifac.cnr.it/tissprop/>. IFAC-CNR, Florence (Italy), 1997. Based on data published by C.Gabriel et al. in 1996.
31. Potworowski, J., et al., *Kernel current source density method*. Neural Comput, 2012. 24(2): p. 541-75.

# Chapter 5

Quantification of hand motor symptoms in Parkinson's Disease: a proof-of-principle study using inertial and force sensors

*Based on:*

van den Noort, J. C., Verhagen, R., van Dijk, K. J., Veltink, P. H., Vos, M. C., de Bie, R. M., ... & Heida, C. T. (2017). Quantification of hand motor symptoms in Parkinson's disease: A proof-of-principle study using inertial and force sensors. *Annals of biomedical engineering*, 45(10), 2423-2436.

*Essential scientific contribution K.J. van Dijk:*

Experiment design, data collection, data analysis

## Abstract

*Objective.* This proof-of-principle study describes the methodology and explores and demonstrates the applicability of a system, existing of miniature inertial sensors on the hand and a separate force sensor, to objectively quantify hand motor symptoms in patients with Parkinson's disease (PD) in a clinical setting (off- and on-medication condition).

*Approach.* Four PD patients were measured in off- and on- dopaminergic medication condition. Finger tapping, rapid hand opening/closing, hand pro/supination, tremor during rest, mental task and kinetic task, and wrist rigidity movements were measured with the system (called the PowerGlove).

*Main results.* To demonstrate applicability, various outcome parameters of measured hand motor symptoms of the patients in off- versus on-medication condition are presented.

*Significance.* The methodology described and results presented show applicability of the PowerGlove in a clinical research setting, to objectively quantify hand bradykinesia, tremor and rigidity in PD patients, using a single system. The PowerGlove measured a difference in off- versus on-medication condition in all tasks in the presented patients with most of its outcome parameters. Further study into the validity and reliability of the outcome parameters is required in a larger cohort of patients, to arrive at an optimal set of parameters that can assist in clinical evaluation and decision-making.



## Introduction

Parkinson's disease (PD) is an age-related neurodegenerative disorder, second in prevalence to Alzheimer's disease [1]. In current practice, the severity of the motor symptoms that partially defines the clinical condition of a PD patient is scored during a standardized neurological examination, using the motor examination part of the Unified Parkinson's Disease Rating Scale (UPDRS-ME) [2, 3].

Assessment of hand movements is an important part of the UPDRS-ME and includes items for bradykinesia, hand tremor and wrist rigidity [2, 4-7]. These are symptoms that strongly respond to dopaminergic medication and deep brain stimulation (DBS) and are therefore often used to judge the effects of these therapies. However, the assessment of the corresponding movements may often vary between clinicians and depends on the level of experience of the neurologist or movement disorder nurse. This subjective nature introduces extra variability to the UPDRS-ME [4, 8-11]. Furthermore, the current clinical exam may not be able to detect small changes as all items are scored on a five-point scale [4, 5, 9, 11]. A single scoring may be dependent on multiple measures such as speed, amplitude, decrease in amplitude over time, and occurrence of hesitations. To adequately study the PD motor symptoms including the effects of medication or DBS and the fluctuations over a period of time, it is worthwhile to find an objective and quantified measure of (the specific components of) these symptoms.

Objective quantification of PD hand motor symptoms has been the subject of several studies (examples are given in Table 5-1). However, previous studies had some limitations since their systems were either very complex (e.g. [12, 13]), unable to measure all hand motor symptoms in one assessment (e.g. [14] [11, 15-17]), or not applied in patients (e.g. [18]). Therefore, these systems are not easily available and/or often clinically not applicable.

In this study, an alternative system to obtain accurate hand and finger kinematics in PD patients is proposed, called the PowerGlove system, which is a combination of miniature inertial and magnetic sensors on each finger segment and the back of the hand [19]. Combination of these sensors enables a 3D reconstruction of the movements of all finger joints and the orientation of the hand. In combination with a force sensor, also joint rigidity could be quantified. Therefore, the PowerGlove might have potential to be used for clinical research into PD motor symptoms without extensive changes to the clinical setting. With this, the effect of dopaminergic medication or DBS could potentially be evaluated.

For application, the system should meet certain requirements, which firstly include clinical applicability measuring all hand motor symptoms in one clinical assessment, and

a good validity on its outcome parameters to differentiate between certain conditions. Other requirements are further validation to discrimination between different clinical scores and a good intra- and inter-reliability. Measurement of hand and finger kinematics with the PowerGlove has already been evaluated with an optoelectronic motion capture system as a reference system [20]. However, application of the PowerGlove for quantification of PD hand motor symptoms in different conditions has not been studied yet.

Therefore, in this proof-of-principle study we explore and demonstrate the applicability of quantifying hand motor symptoms in PD patients with the PowerGlove and an additional force sensor in a clinical setting (in which the patients are admitted to the hospital for a DBS surgery screening and assessed in off- and on- dopaminergic medication condition). This study is part of a larger ongoing project to test the validity and reliability of outcome parameters in a larger cohort of PD patients. In this paper, we first aim to describe the methodology of the application, and demonstrate the results of all hand motor symptoms in a few representative PD patients in off- versus on- dopaminergic medication condition, by means of measured differences in multiple outcome parameters.

## **Materials and Methods**

### **Subjects**

Four PD patients were recruited from the Academic Medical Center (AMC) in Amsterdam, the Netherlands, where they were admitted for an extensive two-day screening in order to become candidates for DBS surgery. In this proof-of-principle study, data of these 4 PD patients (selected randomly from a larger cohort), with a difference of at least 1 point in at least one of the UPDRS-ME hand items in off- versus on-condition, are presented to demonstrate multiple outcome parameters of the measurement system. Inclusion criteria were occurrence of PD symptoms for more than five years, which are interfering with daily life activities. Patient showed in general a good response to dopaminergic medication but suffered from dopamine-dependent motor response fluctuations with or without levodopa induced dyskinesia. Furthermore, patients had to be able to communicate adequately in Dutch or English, and be older than 18 years. Exclusion criteria were a medical history other than PD which restricted hand movements and an inability to correctly place the PowerGlove sensor units on the patient's hand or to correctly perform anatomical calibration (described below). The study was approved by the local Medical Ethical Committee. Full written informed consent was obtained from all patients.

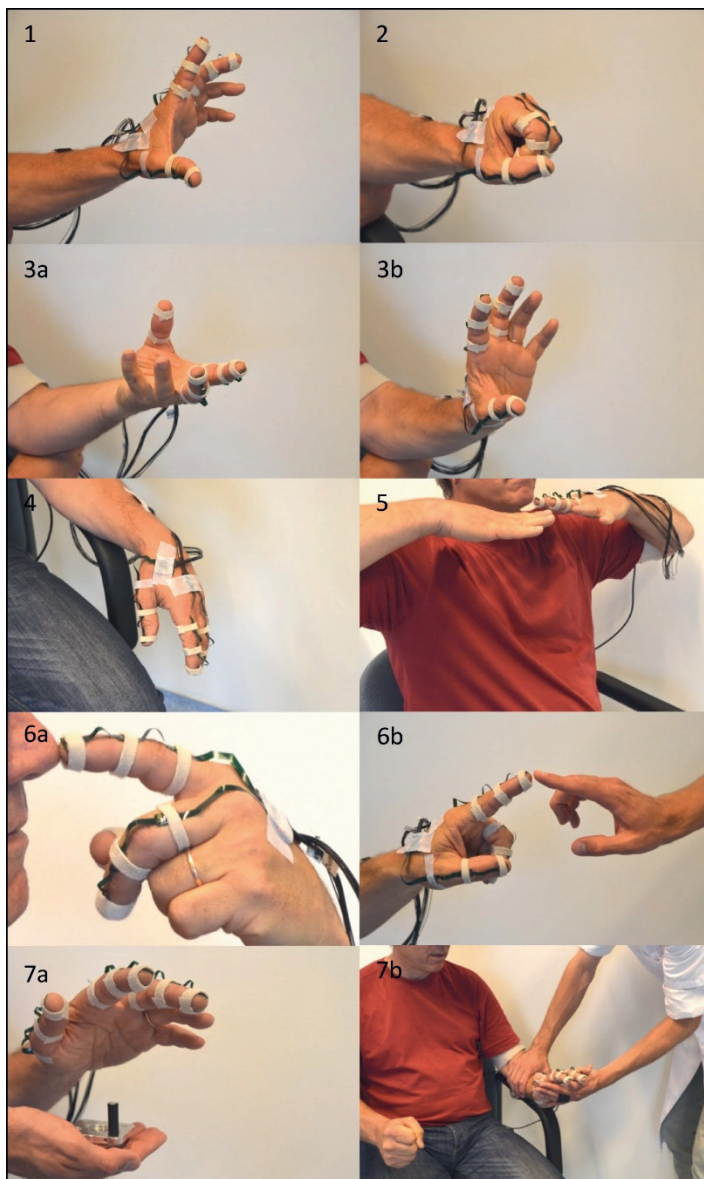


Figure 5-1, Assessment of hand motor symptoms in a patient with Parkinson's disease, using the PowerGlove (miniature inertial sensors on the hand and fingers and, for rigidity assessment, an additional force sensor on the palmar side of the hand). From left to right and top to bottom: (1) rapid finger tapping (thumb/index), (2) rapid hand opening/closing movements and (3a,b) pro/supination of the hand for assessment of bradykinesia; tremor was assessed (4) during rest with and without a mental task, (5) during a posturing task (holding hands outstretched below chin) and (6a,b) during an active kinetic task (moving index finger between patient's nose and the finger of the examiner); (7a,b) the wrist rigidity test consisted of passive wrist flexion/extension (performed by the examiner) with and without contralateral activation by making a fist.

## **PowerGlove system**

Eleven sensor units [19] were attached to the dorsal side of the hand and fingers; on the metacarpal, proximal and distal phalanges of the thumb and the proximal, middle and distal phalanges of the index and middle fingers using small Velcro straps (Figure 5-1). Two sensor units were taped on the back of the hand, of which the one connected to the index and middle finger string was used for the hand orientation. An additional sensor was attached to the dorsal side of the lower arm to be able to measure wrist kinematics. All sensor units contained a 3D gyroscope and a 3D accelerometer (ST LSM330DLC). Additionally, the sensor units on the distal phalanges, metacarpal of the thumb, back of the hand and the lower arm also contained a 3D magnetometer (Honeywell HMC5983).

## **Clinical PD motor symptom assessment**

For each patient, PD motor symptoms were measured in off-medication condition, in the morning after overnight withdrawal from dopaminergic medication; and afterwards in on-medication condition, at the time of optimal medication effect, typically one hour after medication intake (120% of normal morning dose). At both times, the patient had a clinical evaluation by a nurse specialized in movement disorders guided by the version of the UPDRS-ME developed by the Movement Disorder Society (MDS-UPDRS-ME [21, 22]), of which the Dutch translation is validated in our centre. The MDS-UPDRS-ME hand items used in this study include finger tapping (thumb on index finger), rapid hand opening/closing movements and pro/supination of the hand for assessment of bradykinesia [21, 22]. The scale ranges from 0 to 4, with 0 being normal and a higher score indicating more pronounced symptoms. Tremor was assessed during rest with and without a mental task, during a posturing task (holding hands outstretched below chin) and during an active kinetic task (moving index finger between patient's nose and the finger of the examiner). The wrist rigidity test consisted of passive wrist flexion/extension (performed by the examiner) with and without contralateral activation by making a fist.

## **PowerGlove procedure**

Besides the clinical assessment, all patients were evaluated with the PowerGlove system. The order of the clinical assessments by nurse and the PowerGlove assessment was randomized.

At the start of PowerGlove measurements, an anatomical calibration procedure was performed on every patient to determine the sensor-to-segment coordinate systems. The calibration procedure included several steps: (i) hand placed on a flat surface with wrist in 0 degrees flexion, (ii) thumb placed on a flat surface, (iii) thumb flexed 3 times in the

interphalangeal (IP) joint, (iv) fingers flexed 3 times in the metacarpophalangeal (MCP) joints (fingers stretched, hand still), and (v) hands placed together while performing an eight-shaped movement. From these, 3D segment coordinate systems could be determined which describe the segment orientation of the finger segments and the hand [19, 20]. Furthermore, to enable accurate measurements of fingertip positions the lengths of the hand and finger segments were measured using a ruler, which were used for scaling in the applied biomechanical hand model [19, 20]. Besides the anatomical calibration, a magnetic field mapping was performed to account for any disturbances caused by e.g. ferromagnetic materials in the direct environment.

To measure the moment applied on the wrist during the rigidity tasks, a force/moment sensor (ATI mini45, ATI Industrial Automation USA) was used. During this measurement, the lower arm was resting on the arm support of the chair. The hand was passively moved by the examiner, while stabilizing the lower arm. The force/moment sensor was attached to the hand of the examiner using a strap. Moment arm of the sensor to the patient's wrist was measured using a ruler.

Examples of all the PowerGlove assessments are shown in Figure 5-1.

## Data acquisition

Sensor data of the PowerGlove were captured with a sample frequency of 100 Hz using custom-made, Matlab-based software that computed the anatomical segment calibration, and collected information from gyroscopes, accelerometers and magnetometers, and applied this in an extended Kalman filter algorithm that merged all sensory inputs into a biomechanical hand model [19]. Force data was captured with a sample frequency of 512 Hz via a Porti system with PolyBench software (Twente Medical Systems International B.V. Oldenzaal, NL). Post-hoc, the force data were synchronized with the PowerGlove data based on an external synchronization signal that was visible in the magnetometer data of the PowerGlove and in a separate channel captured via the same Porti system as the force data. For this, the data from the force sensor and the synchronization signal were down-sampled to 100 Hz.

Table 5-1. Examples of studies using objective quantification of PD motor symptoms.

Study	Measurement system	Placement on body	Parameters
<b>Bradykinesia</b>			
Dunnewold et al. [5]	Accelerometer	Wrist	Mean acceleration Tap rate
Tavares et al. [36]	Quantitative digitography using a computerized-interfaced keyboard	Not applicable	Time of movement interval Time of movement interval Velocity Frequency
Koop et al. [20]	Gyroscope	Hand	Root mean square angular velocity
Keijsers et al. [19]	Accelerometer	Several body parts	Mean velocity
Salarian et al. [32]	Gyroscope	Forearm	Root mean square angular velocity Amplitude
Tabbal et al. [35]	Gyroscope	Forearm	Total range of motion
Jun et al. [18]	Gyroscope	Hand	Root mean square angular velocity Root mean square angle and angular velocity
Endo et al. [8]	Magnetic sensor consisting of two coils	Thumb and tip of index finger	Peak power and total power of angular Maximum velocity Amplitude of position data
Pulliam et al. [31]	Accelerometer and gyroscope	Index finger	Time of movement interval Amplitude Velocity
Mentzel et al. [23]	Accelerometer and gyroscope Magnetometers	Forearm Upper arm Waist	Rhythm Time of movement interval Amplitude Velocity
Djuric-Jovicic et al. [3]	Gyroscopes	Thumb and tip of index finger	Time of movement interval Angular velocity Total angular range of motion (aperture)
<b>Tremor</b>			
Keijsers et al. [19]	Accelerometer	Several body parts	Percentage peak frequencies above 4 Hz
Salarian et al. [32]	Gyroscope	Forearm	Root mean square angular velocity Amplitude
Giuffrida et al. [12]	Accelerometer and gyroscope	Middle finger	Total range of motion Peak power acceleration and angular velocity Frequency of the peak power
Gallego et al. [11]	Gyroscope	Forearm Hand	Root mean square of angular velocity and of Amplitude angular velocity Frequency

Mostile et al. [24]	Accelerometer and gyroscope	Middle finger	Root mean square amplitude Peak power angular velocity and acceleration Peak power of angular velocity Root mean square of acceleration Maximum amplitude acceleration Peak power, median power and power distribution of acceleration Amplitude
Heldman et al. [16] Scanlon et al. [33] Daneault et al. [1]	Accelerometer and gyroscope Accelerometer Accelerometer (in smart phone)	Index finger Upper and lower limbs Unknown	
Pulliam et al. [31] <b>Rigidity</b> Prochazka et al. [30]	Accelerometer and gyroscope Hand-held force sensing device (air-filled pads) combined with a compliant displacement gauge Torque motor Electromyography Pads connected to a force transducer Gyroscope	Index finger Wrist Forearm Hand Elbow Wrist	Impedance Viscous damping constant Elastic stiffness Impulse Work Elastic stiffness Viscous damping constant Impedance Range of motion Viscous damping constant Elastic stiffness Impedance
Fung et al. [10] Patrick et al. [27]			
Sepheri et al. [34]	Test rig with strain gage force transducer and potentiometer	Elbow	
Tabbal et al. [35] Park et al. [26]	Pads connected to a force transducer Gyroscope Torque motor Potentiometer Load cell Accelerometer Force sensor Gyroscope Electromyography Torque motor Electromyography Load cell Potentiometer Accelerometer	Elbow Wrist Wrist  Wrist  Wrist  Wrist  Wrist	Torque Viscous damping constant Elastic stiffness Work & Impulse Torque Elastic coefficient  Work & Impulse Reflex responses Viscous damping constant Elastic stiffness Impulse Impedance
Endo et al. [7, 8] Powell et al. [29] Kwon et al. [22]			

## Data analysis and parameters

The signals measured and computed by the PowerGlove system could be used for quantification of each of the PD hand motor symptoms. These signals include angular velocity and acceleration of the hand and finger segments, positions of segments (e.g. fingertip), joint angles (e.g. MCP joint) and applied force (for the rigidity test only) (Figure 5-2). From these signals, many outcome parameters can be extracted to quantify PD motor symptoms (Table 5-2). The selection of these parameters is based on the parameters previously used in the literature (Table 5-1) and on characteristics of the assessed phenomena, such as movement information for bradykinesia and tremor (e.g. amplitude, velocity and frequency characteristics) and movement and force information for rigidity (e.g. torque-angle relations) (Figure 5-2 and Table 5-2). To demonstrate the applicability of the PowerGlove system for the quantification of PD hand motor symptoms, differences in the outcome parameters listed in Table 5-2 were explored in off- versus on-medication condition.

### Bradykinesia

Bradykinesia during finger tapping was quantified using data of four sensors of the PowerGlove: the sensors on the tip of the index finger, tip of the thumb, proximal phalanx of the index finger, and the back of the hand (Figure 5-2). Since movement could occur around all three axes of a sensor, the norm of the accelerations in three directions (3D:  $x,y,z$ ) and the norm of the 3D angular velocities were calculated. MCP joint angles (flexion/extension) and 3D index and thumb fingertip positions were obtained from the PowerGlove software based on the anatomical calibration, forward kinematics and biomechanical hand model [19]. The distance between the tips of the index finger and thumb was calculated by the norm of the difference between the two position vectors in space. The time of each movement interval was determined using the MCP angle (cycle time, average and standard deviation over cycles). For acceleration and angular velocity, the root mean square (RMS) over all cycles was calculated. Furthermore, for the MCP angle and thumb/index amplitude, the minimum, maximum and range of motion (ROM) per cycle was determined, and consequently the average and standard deviation over cycles were calculated as outcome parameters (Table 5-2).

For analysis of hand opening/closing movements, data of three sensors of the PowerGlove were used: the sensors on the tip of the index finger, proximal phalanx of the index finger, and hand (Figure 5-2). The same procedure was followed as for the finger tapping task, including similar parameters (Table 5-2). Instead of index/thumb amplitude, the trajectory of the index fingertip position with respect to the hand was calculated using the norm of the vector.



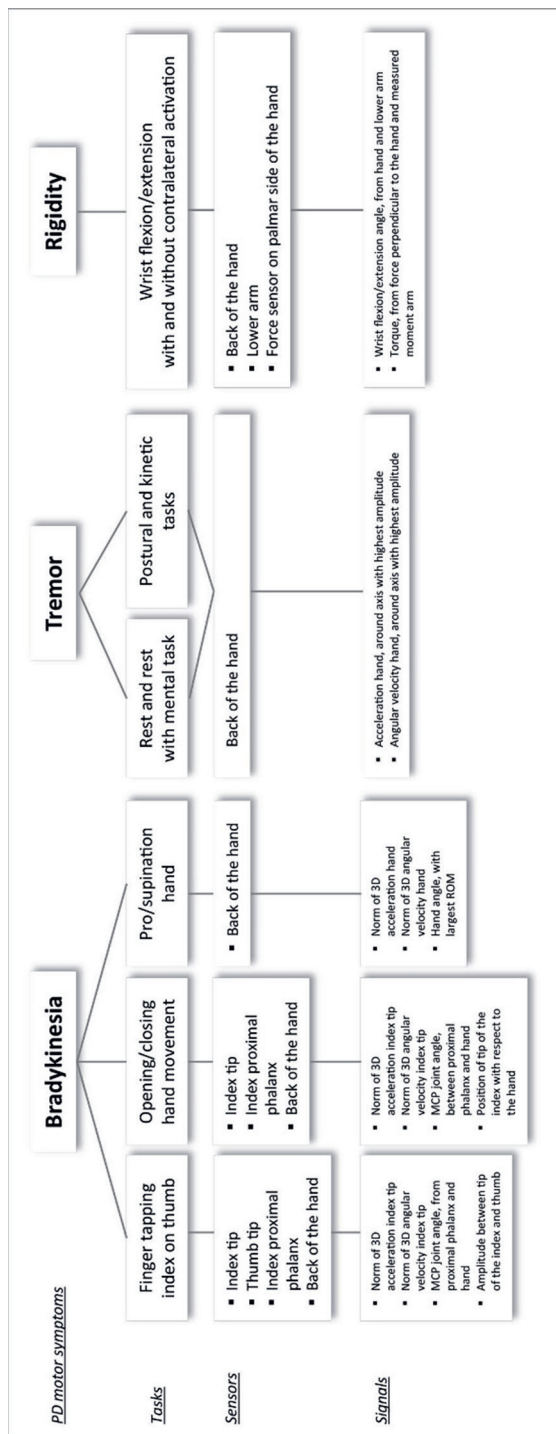


Figure 5-2, Sensors and signals used to determine hand motor symptoms in Parkinson's disease with the PowerGlove system

For pro/supination, data of the hand sensor were used (Figure 5-2). In line with the procedure as described above, the norm of the hand accelerations in three directions (3D:  $x,y,z$ ) and the norm of the 3D hand angular velocities were calculated. For the other outcome parameters based on the hand angle (Figure 5-2 and Table 5-2), first the 3D hand angles in the global coordinate system were determined in which the angles were calculated with respect to the anatomical reference position (hand and lower arm placed on a flat surface). Subsequently, from the 3D hand angles, the hand angle with the greatest ROM was selected as representing the pro/supination angle.

### Tremor

Tremor was quantified using data of the hand sensor (Figure 5-2). Data of accelerometers and gyroscopes were bi-directional second-order high-pass filtered at 1.0 Hz (Butterworth) [14, 17, 23, 24] to remove slow voluntary movements and dyskinesia. For the kinetic task, the acceleration and angular velocity data were bi-directional second-order high-pass filtered at 4.0 Hz (Butterworth) to also remove the faster voluntary movement.

Spectral analysis (discrete Fourier transform) was performed on the 3D acceleration and 3D angular velocity signals to analyse the data in the frequency domain. Peak power and total power around the axis with the highest amplitude was evaluated in the 4-10 Hz frequency band, i.e. the band in which PD tremor can be expected for both rest and kinetic tasks, therewith excluding voluntary movement ( $<4$  Hz) and physiological tremor (10-12 Hz) [14, 17, 23, 25-28]. The total power of the tremor band was calculated by numerical integration of the power in the frequency bands. Also, RMS values of acceleration and angular velocity around the axis with the highest amplitude were calculated (Table 5-2).

### Rigidity

Wrist rigidity was quantified using the inertial sensors on the lower arm and hand, and the force sensor that was placed on the palmar side of the patient's hand by the examiner during the wrist extension/flexion movement (Figure 5-2). The wrist flexion/extension angle was calculated from the angle between lower arm and hand, anatomically calibrated using a posture with hand and lower arm on a flat surface in 0 degrees flexion/extension. The torque (i.e. wrist joint moment) was calculated by multiplying the measured moment arm with the force measured perpendicular to the hand. For analysis, only the wrist extension movements were selected. Selected wrist movements were averaged for further calculation of parameters. For maximal ROM, the maximal extension angle was determined. Torque was defined at 20 and 50 degrees wrist extension and at maximal wrist extension. Stiffness was defined as the slope of the torque-angle curve of the wrist, over the 10-90% range of motion window (in degrees). Impulse was calculated by the

Table 5-2 Investigation parameters for quantification of bradykinesia, rigidity and tremor obtained by signals measured with the Powerglove system.

Task	Parameters
<b>Bradykinesia:</b>	
Finger tapping index on thumb	RMS of the acceleration of the index fingertip, over all cycles (norm of 3D)
Hand opening/closing	RMS of the angular velocity of the index fingertip, over all cycles (norm of 3D)
	Time of movement intervals (i.e. cycle time) using MCP angle, average and standard deviation of all cycles
	Minimum, maximum and ROM of the MCP angle of the index finger, average and standard deviation of all cycles (flexion angle)
	Minimum, maximum and ROM of the distance (i.e. amplitude) between index and thumb fingertips, average and standard deviation of all cycles (finger tapping)
	Minimum, maximum and ROM of the distance (i.e. amplitude) between index fingertip and hand, average and standard deviation of all cycles (hand open/close)
Pro/supination	RMS of acceleration of the hand, over all cycles (norm 3D)
	RMS of angular velocity of the hand, over all cycles (norm 3D)
	Time of movement intervals (i.e. cycle time) using the hand angle, average and standard deviation of all cycles
	Minimum, maximum and ROM of the hand angle, average and standard deviation of all cycles (angle with largest ROM)
<b>Tremor:</b>	
During rest	RMS of acceleration of the hand (around axis with highest acceleration)
During mental task	RMS of angular velocity of the hand (around axis with highest angular velocity)
During postural task	Peak power in tremor band (4-10Hz) using the acceleration of the hand
During kinetic task	Total power in tremor band (4-10Hz) using the acceleration of the hand
<b>Rigidity:</b>	
Wrist-flexion-extension (passive)	Maximum ROM of wrist angle
	Torque at 20° and 50° wrist extension at wrist joint
	Maximal torque
	Stiffness of wrist joint (10-90% range of motion window)
	Impulse of wrist joint (10-90% time window)
	Work of wrist joint (10-90% range of motion window)
<b>RMS root mean square, ROM range of motion, MCP metacarpophalangeal joint</b>	

integration of torque over a 10-90% time window (in seconds) and work was determined by integration of torque over angle using the 10-90% range of motion window (in degrees) (Table 5-2).

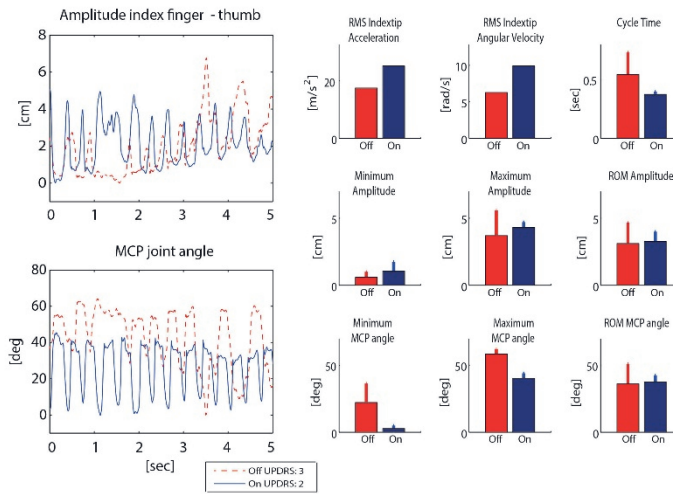
## Results

All patients were able to perform the anatomical calibration of the PowerGlove and the tasks related to the hand in the MDS-UPDRS-ME with the PowerGlove attached, in both off- and on-medication condition. The total time to measure all hand motor symptoms varied between 15 and 30 minutes per condition. Typical examples of data and outcome parameters of the 4 representative patients measured with the PowerGlove in off- versus on-medication condition are presented in Figures 5-3, 5-4 and 5-5 for bradykinesia, tremor and rigidity respectively, showing a difference between conditions in most outcome parameters. MDS-UPDRS-ME scores of these patients are shown in the legends.

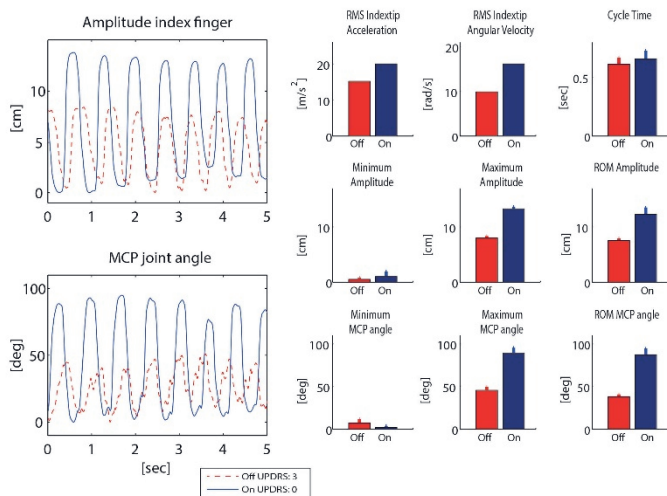
Figure 5-3 →

*Bradykinesia of the hand in Parkinson's disease patients. Outcome parameters measured with the PowerGlove in off- and on-medication condition: A. Finger tapping (patient 1); B. Opening/closing hand movements (patient 2); C. Pro/supination of the hand (patient 2). For all parameters, the average per cycle (barplot) and the standard deviations over cycles are shown. For RMS, the value of the whole time window is shown. MDS-UPDRS-ME scores are shown in the legends.*

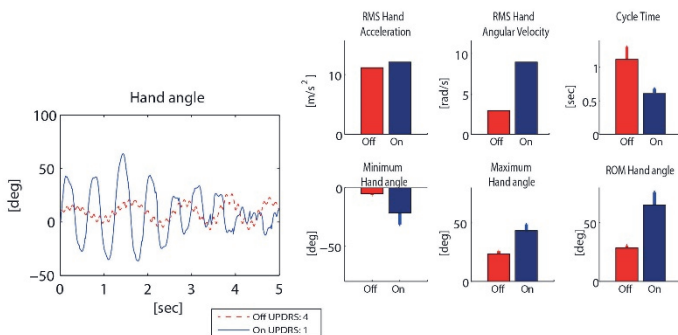
## A. Finger tapping index/thumb



## B. Opening/closing hand movement



## C. Pro/supination hand



## Bradykinesia

Finger tapping (Figure 5-3A; UPDRS off: 3, on: 2) shows higher movement speed in on- versus off-medication condition. This is most expressed in the increased RMS acceleration and RMS angular velocity and in the decreased cycle time. The minimal MCP joint angle was lower in the on- versus off-medication condition, which means that the index finger was in general more extended during movement in the on-condition. Full MCP joint extension (0 degrees) was not always reached in off-medication condition. Most pronounced was the movement irregularity in off-medication condition, which is expressed in high standard deviations of cycle time, amplitude (maximum and ROM) and MCP angle (minimum and ROM). The average ROM values did not show clear differences.

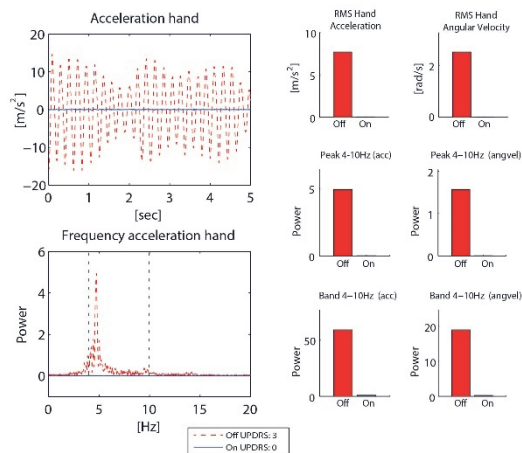
Opening/closing hand movement (Figure 5-3B; UPDRS off: 3, on: 0) shows clear improvement in all parameters in the on-medication condition (i.e. increased velocity, acceleration, amplitude and range of motion), except for the cycle time. The minimum MCP angle shows good extension in both conditions. This example does not show any hesitation in the presented time-frame in either off- or on-medication condition; the cycle time standard deviations are small in both conditions.

The pro/supination parameters (Figure 5-3C; UPDRS off: 4, on 1) show improvement in all parameters in on- versus off-medication condition, i.e. a higher velocity, shorter cycle time and larger ROM. In the hand angle it can be observed that pro/supination movement in off-medication condition could barely be performed, as seen from the small ROM. Furthermore, over the slow pro/supination movements in off-medication condition, a tremor movement (of about 7 Hz) can be observed.

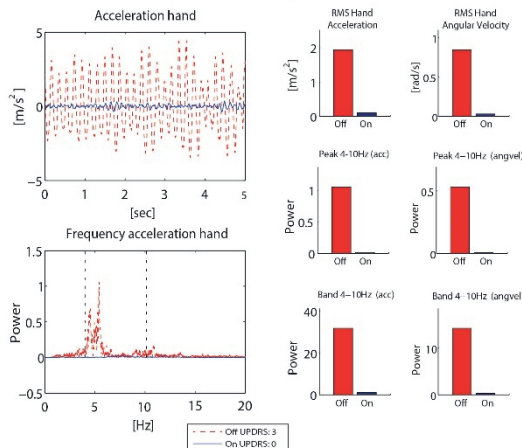
Figure 5-4, →

*Tremor of the hand in Parkinson's disease patients. Outcome parameters measured with the PowerGlove in off- and on-medication condition: A. Tremor at rest (patient 3); B. Tremor during mental task (patient 1); C. Tremor during kinetic task (patient 2). The frequency band (4-10 Hz) is indicated with the black dotted lines. MDS-UPDRS-ME scores are shown in the legends.*

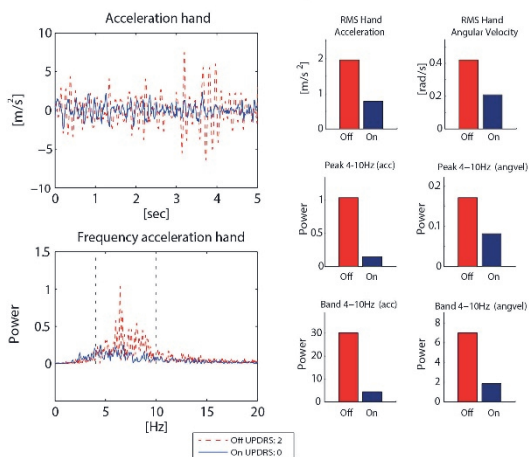
## A. Tremor at rest



## B. Tremor during mental task



## C. Tremor during kinetic task



## Tremor

Parameters for tremor at rest (UPDRS off 3, on 0) and tremor during a mental task (UPDRS off 3, on 0) and a kinetic task (UPDRS off 2, on 0) show a difference in all parameters in on- versus off-medication condition (Figure 5-4). No tremor is present in on-medication condition during rest and during the mental task, whereas in off-medication condition tremor is clearly present as can be seen by the large power in the 4-10 Hz frequency band, where tremor is expected for PD patients. Furthermore, a high RMS is seen in off-medication condition (related to high amplitude, present most of the time).

## Rigidity

Finally, the quantification of parameters of the wrist rigidity task (Figure 5-5, without contralateral activation; UPDRS off 2, on 1) shows that due to the medication intake, the wrist ROM is increased, whereas torque, stiffness, impulse and work are all decreased in comparison to the off-medication condition.

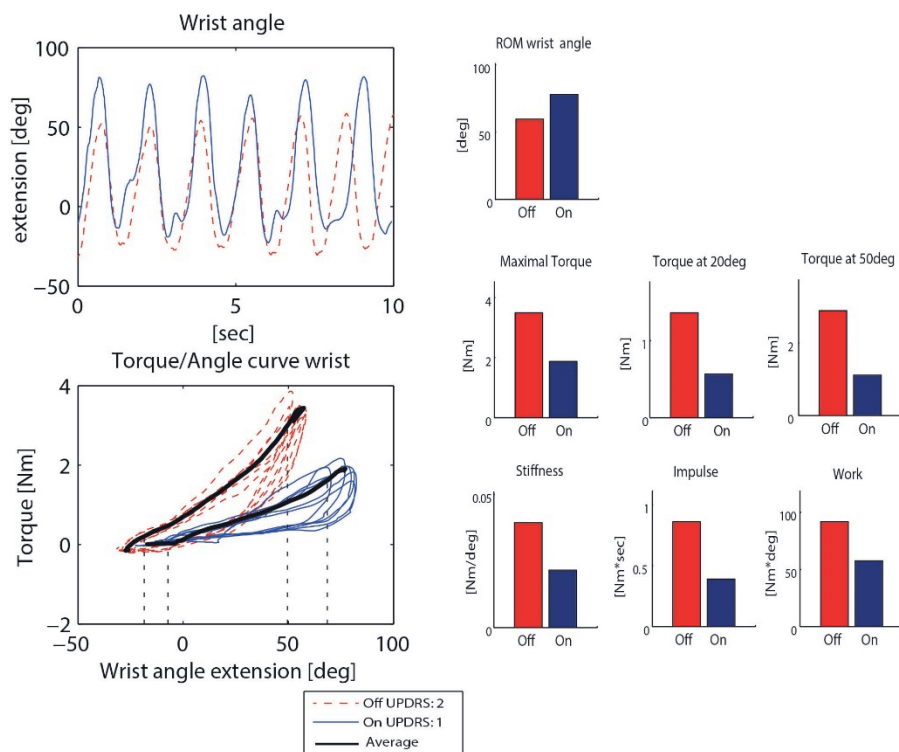


Figure 5-5, Rigidity of the wrist in a Parkinson's disease patient. Outcome parameters measured with the PowerGlove in off- and on-medication condition (patient 4). The 10-90% range of motion windows are indicated with the black dotted lines. MDS-UPDRS-ME scores are shown in the legends.



## Discussion

### Applicability of the PowerGlove and proposed outcome parameters

In the past, several measurement systems have been proposed to quantify the hand motor symptoms in PD. However, only a few studies have attempted to measure at least two of the phenomena of bradykinesia, tremor and rigidity with a single system or together in one study [5, 11, 25, 29]. In our study, the PowerGlove enabled us to measure all hand motor symptoms in PD patients using a combination of inertial sensors and a force sensor, where the force sensor was only applied for the assessment of wrist rigidity. We selected a variety of outcome parameters to show the applicability of the PowerGlove (Table 5-2), to measure differences in off- versus on-medication condition and to explore optimal outcome parameters.

Previously, it has been shown that for assessment of bradykinesia, increased angular velocity (maximum, RMS) is related to improvement after DBS [5, 27] and can be used to discriminate between UPDRS-ME scores [24, 29, 30]. Furthermore, amplitude (distance between the tips of the index finger and thumb) has been shown to be sensitive in measuring differences in bradykinesia, such as after DBS [5].

In the finger tapping task, a large and fast index finger movement is important, and full extension of the MCP joint needs attention. Not all parameters showed improvement in on-medication condition. In line with literature, RMS of angular velocity and acceleration as well as maximum amplitude did improve in the given example (i.e. increased in on-medication condition). Furthermore, average cycle time and standard deviations of cycle time and ROM did decrease. However, average ROM of amplitude and MCP angle did not clearly discriminate on- and off-medication condition. That is likely caused by irregularity of the movement in off-medication condition, where fast and small movements are followed by several slow and large movements (in accordance to a MDS-UPDRS-ME score of 3 [22]), leading to a mean ROM that is comparable to the on-medication state. Because a patient's movement in the off-medication state can be affected in different ways (see e.g. the patterns described in [18]), it remains important to always combine mean values with standard deviations when interpreting ROM values.

In the pro/supination task, improvement was observed in all measured parameters of the presented patients. Also for hand opening/closing movement, all parameters improved, except cycle time.

The different results of the three bradykinesia tasks illustrate that bradykinesia can improve in different ways for different tasks and/or different patients, either as an improvement in amplitude, speed or both. For example, in the opening/closing

movement, an increase in amplitude can cloud an increase in speed, when only measuring cycle times. An objective and quantitative measurement system like the PowerGlove enables us to measure different aspects of hand motor control that might be clinically relevant for PD patients. In the clinical exam, this might be difficult to observe and will surely be difficult to separately quantify using only the 0-4 scoring system. Quantifying only one parameter might be too restricted to describe the complex phenomenon of bradykinesia, since this is related to several aspects of the movement like amplitude, ROM, velocity, occurrence of hesitation and mean and SD of the time of each cycle. Yet, the PowerGlove system enables us to combine several quantitative parameters.

For tremor, literature indicates that peak power [17] and RMS and amplitude of acceleration and angular velocity [16, 23, 25] are correlated to clinical scores or discriminative in off- versus on-medication. We did not include amplitude for tremor, but RMS was calculated for acceleration and angular velocity around the axis with highest amplitude and showed differences between off- and on-medication in the presented example. The same was true for all power parameters. It is likely that tremor can be quantified fairly easily by many systems, therefore, the added value of the PowerGlove mainly lies in the ability to combine tremor measurement with bradykinesia and rigidity measurements.

Finally, for the assessment of rigidity, in literature torque [5, 31], impulse [7, 32] and the viscous damping constant [10, 12, 32] were shown to correlate with the UPDRS-ME scores, improve after DBS or differentiate between patients and controls, whereas work was shown not to be a valid measure [7, 12]. We measured increased ROM and decreased torque, stiffness, impulse and work, reflecting a reduction in rigidity in the PD patient. Viscous damping constant has not been calculated. This parameter has to be determined using a fitting spring-damper model and reflects velocity-dependent behavior [12, 32]. Such an approach is more complex and, since all chosen parameters improved after medication intake, it is questionable whether including this parameter would be necessary to quantify a difference in on- and off-medication state.

Since in the rigidity test the ROM in on-medication condition is increased, this might have influenced the calculated work, and possibly also the impulse calculations. Using a similar window in the on- and off medication condition, e.g. the ROM of the off-medication condition, would further reduce the calculated work in on-medication condition. The use of the PowerGlove might enable standardization of either the measured or analyzed ROM between on- and off-medication measurement, which might increase the reliability of rigidity measurements. However, the maximal ROM itself is also an outcome that could be clinically relevant for PD patients.

## Future directions

This proof-of-principle study is the first step in a larger study, in which the aim is to test the validity and reliability of the proposed outcome parameters in a larger cohort of PD patients. For validity, the correlation of the outcome parameters with the MDS-UPDRS-ME scores could be further studied. However, not all proposed parameters might be suitable to discriminate between small deviations in a patient's clinical condition, or could also be redundant with respect to each other. Therefore, per clinical phenomenon an optimal set of parameters should be defined describing the different aspects of that particular motor symptom (as discussed above), which could guide clinical evaluation and decision-making. Additionally, evolution of parameters over the course of one measurement can be of importance. An optimal set of parameters to describe different aspects of a motor symptom could be found by using methods such as machine learning. This may lead to the development of a prediction tool with classification algorithms based on measurement sets to e.g. predict MDS-UPDRS-ME scores, or to discriminate small changes in the outcome parameters that cannot be observed with the clinical score.

The influence of reattachment of sensors and a second anatomical calibration in between conditions on the outcome parameters needs to be further investigated in an intra- and inter-rater reliability study. This calibration is important for the determination of the MCP joint angle, hand angle and fingertip positions. Results of a previous study on a comparison between the PowerGlove and an opto-electronic system (a standard in most movement analysis laboratories) already give some insights in the effect of calibration [20]. It shows that the effect of another anatomical calibration (in that case due to using a different measurement system) is limited to a difference in finger joint angles between 3 and 8deg and a difference in thumb/index amplitude of less than 16mm. The on- vs. off-differences presented in the PD patients (Figure 5-3, 5-4 and 5-5) are larger than these differences.

For determination of the outcome parameters, not all data of all sensors have been used (Table 5-2). Therefore, for future application of the PowerGlove in a clinical setting, a reduced set of sensors might be sufficient to obtain clinically relevant outcome parameters. In a recent study, only sensors on the tip of the index finger and thumb are proposed to measure angular changes during finger tapping [18]. However, to estimate distance between the tip of the index finger and of the thumb in bradykinesia tasks, a reduced set of sensors is only applicable with the prerequisite that position of the tip of the index finger and thumb can be modeled without any information about the orientation of the middle phalanx of the index and the metacarpal and proximal phalanges of the thumb (such as in

Nataraj et al. [33]). Data of the middle finger is not used at all, and these sensors could therefore easily be omitted.

For easy attachment to the fingers, the miniature inertial sensors should be embedded in either a glove or easy to use straps connected to the sensors. With the current straps, the sensors were firmly attached, but a quicker way of attachment is desirable. Currently, the system is not wireless. However, the wires are lightweight and patients mentioned no limitations in their movement because of the wires. Still, for future application, a wireless system would be desirable. Moreover, the sensors/glove should be easy to clean, especially when future applications during DBS surgery are envisioned, in which quantitative assessment of symptom severity could guide DBS implantation or optimization of stimulation settings. If a next version of the system will be developed for future DBS applications, using for example a glove approach, new studies on reliability and validity are needed, in which current knowledge on the clinical applicability and outcome parameters, such as presented in this paper, will be helpful. Until now, only a few studies attempted to quantify motor symptoms during DBS surgery [27, 34] or for automatic optimization of DBS settings [11]. Optimization of DBS settings can be a challenge due to the number of variables that must be considered, including presence of multiple motor signs, side effects and battery life [11]. A simple and objective way to quantify the motor symptoms in the hand can definitively assist in this challenging process.

### **Limitations of the study**

Outcome parameters are calculated over a time-window of 5 seconds. Although this time frame is sufficient to illustrate the applicability, longer time-windows may be necessary to assess certain aspects of PD hand motor symptoms, such as hesitation in movement or decrease in amplitude over time for bradykinesia tasks. Also, when a patient shows large fluctuations in tremor symptoms, longer registration and the detection of tremor and non-tremor windows might be beneficial.

For determination of outcome parameters in the rigidity task, only the force perpendicular to the palmar side of the hand has been used. In this way, the calculation of the torque has been simplified. Contribution of forces and moments in other directions, as well as the contribution of mass and inertia of the hand and the force sensor itself, have been neglected. It was assumed that the force applied to the hand was largest in the direction of the movement. For mass parameters (mass, inertia and center of gravity), an anthropometric model is required of the hand. Since the hand is a small structure, contribution of these parameters were assumed to be negligible.

Finally, since this is a proof-of-principle study, the number of subject included and the number of examples shown is limited. Therefore, no group results and statistics could be presented. In a future study, a larger cohort of patients will be included and analyzed to assess the clinimetric properties of the PowerGlove and to derive to an optimal set of parameters per symptom.

## Conclusion

The methodology described and the results presented in the current paper show the applicability of the PowerGlove to objectively quantify bradykinesia, tremor and rigidity in PD patients in a clinical research setting. The presented examples showed a difference in off- versus on-medication condition in all tasks for most outcome parameters. Further study into validity and reliability of the proposed outcome parameters is required in a larger group of patients, to arrive at an optimal set of parameters that will guide clinical evaluation and decision making.

## References

1. Dorsey, E., Constantinescu, R., Thompson, J. P., Biglan, K. M., Holloway, R. G., Kieburtz, K., ... & Tanner, C. M. (2007). Projected number of people with Parkinson disease in the most populous nations, 2005 through 2030. *Neurology*, 68(5), 384-386.
2. Fahn, S. (1987). Unified Parkinson's disease rating scale. Recent developments in Parkinson's disease volume II. *Macmillan Healthcare Information*, 153.
3. Goetz, C. G., LeWitt, P. A., & Weidenman, M. (2003). Standardized training tools for the UPDRS activities of daily living scale: newly available teaching program. *Movement Disorders: Official Journal of the Movement Disorder Society*, 18(12), 1455-1458.
4. Patrick, S. K., Denington, A. A., Gauthier, M. J., Gillard, D. M., & Prochazka, A. (2001). Quantification of the UPDRS rigidity scale. *IEEE transactions on neural systems and rehabilitation engineering*, 9(1), 31-41.
5. Endo, T., Yokoe, M., Fujimura, H., & Sakoda, S. (2011). Novel methods to evaluate symptoms in Parkinson's disease—rigidity and finger tapping. *Diagnostics and Rehabilitation of Parkinson's Disease. Rijeka: InTech*, 191-206.
6. Keijsers, N. L., Horstink, M. W., & Gielen, S. C. (2006). Ambulatory motor assessment in Parkinson's disease. *Movement disorders: official journal of the Movement Disorder Society*, 21(1), 34-44.
7. Fung, V. S., Burne, J. A., & Morris, J. G. (2000). Objective quantification of resting and activated parkinsonian rigidity: a comparison of angular impulse and work scores. *Movement Disorders: Official Journal of the Movement Disorder Society*, 15(1), 48-55.
8. Post, B., Merkus, M. P., de Bie, R. M., de Haan, R. J., & Speelman, J. D. (2005). Unified Parkinson's disease rating scale motor examination: are ratings of nurses, residents in neurology, and movement disorders specialists interchangeable?. *Movement disorders: official journal of the Movement Disorder Society*, 20(12), 1577-1584.
9. Prochazka, A., Bennett, D. J., Stephens, M. J., Patrick, S. K., Sears-Duru, R., Roberts, T., & Jhamandas, J. H. (1997). Measurement of rigidity in Parkinson's disease. *Movement disorders: official journal of the Movement Disorder Society*, 12(1), 24-32.
10. Sepehri, B., Esteki, A., Ebrahimi-Takamjani, E., Shahidi, G. A., Khamseh, F., & Moinodin, M. (2007). Quantification of rigidity in Parkinson's disease. *Annals of Biomedical engineering*, 35(12), 2196-2203.
11. Pulliam, C. L., Heldman, D. A., Orcutt, T. H., Mera, T. O., Giuffrida, J. P., & Vitek, J. L. (2015). Motion sensor strategies for automated optimization of deep brain stimulation in Parkinson's disease. *Parkinsonism & related disorders*, 21(4), 378-382.

12. Park, B. K., Kwon, Y., Kim, J. W., Lee, J. H., Eom, G. M., Koh, S. B., ... & Hong, J. (2010). Analysis of viscoelastic properties of wrist joint for quantification of parkinsonian rigidity. *IEEE Transactions on Neural Systems and Rehabilitation Engineering*, 19(2), 167-176.
13. Powell, D., Threlkeld, A. J., Fang, X., Muthumani, A., & Xia, R. (2012). Amplitude- and velocity-dependency of rigidity measured at the wrist in Parkinson's disease. *Clinical Neurophysiology*, 123(4), 764-773.
14. Gallego, J. A., Rocon, E., Roa, J. O., Moreno, J. C., & Pons, J. L. (2010). Real-time estimation of pathological tremor parameters from gyroscope data. *Sensors*, 10(3), 2129-2149.
15. Giuffrida, J. P., Riley, D. E., Maddux, B. N., & Heldman, D. A. (2009). Clinically deployable Kinesia™ technology for automated tremor assessment. *Movement disorders: official journal of the Movement Disorder Society*, 24(5), 723-730.
16. Mostile, G., Giuffrida, J. P., Adam, O. R., Davidson, A., & Jankovic, J. (2010). Correlation between Kinesia system assessments and clinical tremor scores in patients with essential tremor. *Movement disorders*, 25(12), 1938-1943.
17. Heldman, D. A., Jankovic, J., Vaillancourt, D. E., Prodoehl, J., Elble, R. J., & Giuffrida, J. P. (2011). Essential tremor quantification during activities of daily living. *Parkinsonism & related disorders*, 17(7), 537-542.
18. Djurić-Jovičić, M., Jovičić, N. S., Roby-Brami, A., Popović, M. B., Kostić, V. S., & Djordjević, A. R. (2017). Quantification of finger-tapping angle based on wearable sensors. *Sensors*, 17(2), 203.
19. Kortier, H. G., Sluiter, V. I., Roetenberg, D., & Veltink, P. H. (2014). Assessment of hand kinematics using inertial and magnetic sensors. *Journal of neuroengineering and rehabilitation*, 11(1), 70.
20. van den Noort, J. C., Kortier, H. G., Beek, N. V., Veeger, D. H., & Veltink, P. H. (2016). Measuring 3D hand and finger kinematics—a comparison between inertial sensing and an opto-electronic marker system. *PLoS One*, 11(11), e0164889.
21. Goetz, C. G., Fahn, S., Martinez-Martin, P., Poewe, W., Sampaio, C., Stebbins, G. T., ... & Holloway, R. (2007). Movement Disorder Society-sponsored revision of the Unified Parkinson's Disease Rating Scale (MDS-UPDRS): process, format, and clinimetric testing plan. *Movement disorders*, 22(1), 41-47.
22. Goetz, C. G., Tilley, B. C., Shaftman, S. R., Stebbins, G. T., Fahn, S., Martinez-Martin, P., ... & Dubois, B. (2008). Movement Disorder Society-sponsored revision of the Unified Parkinson's Disease Rating Scale (MDS-UPDRS): scale presentation and clinimetric testing results. *Movement disorders: official journal of the Movement Disorder Society*, 23(15), 2129-2170.

23. Daneault, J. F., Carignan, B., Codère, C. É., Sadikot, A. F., & Duval, C. (2013). Using a smart phone as a standalone platform for detection and monitoring of pathological tremors. *Frontiers in human neuroscience*, 6, 357.
24. Jun, J. H., Kim, J. W., Kwon, Y., Eom, G. M., Koh, S. B., Lee, B., ... & Tack, G. R. (2011). Quantification of limb bradykinesia in patients with Parkinson's disease using a gyrosensor—Improvement and validation. *International Journal of Precision Engineering and Manufacturing*, 12(3), 557-563.
25. Salarian, A., Russmann, H., Wider, C., Burkhard, P. R., Vingerhoets, F. J., & Aminian, K. (2007). Quantification of tremor and bradykinesia in Parkinson's disease using a novel ambulatory monitoring system. *IEEE Transactions on Biomedical Engineering*, 54(2), 313-322.
26. Deuschl, G., Bain, P., Brin, M., & Ad Hoc Scientific Committee. (1998). Consensus statement of the movement disorder society on tremor. *Movement disorders*, 13(S3), 2-23.
27. Koop, M. M., Andrzejewski, A., Hill, B. C., Heit, G., & Bronte-Stewart, H. M. (2006). Improvement in a quantitative measure of bradykinesia after microelectrode recording in patients with Parkinson's disease during deep brain stimulation surgery. *Movement disorders: official journal of the Movement Disorder Society*, 21(5), 673-678.
28. Elias, W. J., & Shah, B. B. (2014). Tremor. *Jama*, 311(9), 948-954.
29. Tabbal, S. D., Ushe, M., Mink, J. W., Revilla, F. J., Wernle, A. R., Hong, M., ... & Perlmuter, J. S. (2008). Unilateral subthalamic nucleus stimulation has a measurable ipsilateral effect on rigidity and bradykinesia in Parkinson disease. *Experimental neurology*, 211(1), 234-242.
30. Mentzel, T. Q., Lieveise, R., Levens, A., Mentzel, C. L., Tenback, D. E., Bakker, P. R., ... & van Harten, P. N. (2016). Reliability and validity of an instrument for the assessment of bradykinesia. *Psychiatry Research*, 238, 189-195.
31. Endo, T., Okuno, R., Yokoe, M., Akazawa, K., & Sakoda, S. (2009). A novel method for systematic analysis of rigidity in Parkinson's disease. *Movement Disorders: Official Journal of the Movement Disorder Society*, 24(15), 2218-2224.
32. Kwon, Y., Park, S. H., Kim, J. W., Ho, Y., Jeon, H. M., Bang, M. J., ... & Eom, G. M. (2014). Quantitative evaluation of parkinsonian rigidity during intra-operative deep brain stimulation. *Bio-medical materials and engineering*, 24(6), 2273-2281.
33. Nataraj, R., & Li, Z. M. (2013). Robust identification of three-dimensional thumb and index finger kinematics with a minimal set of markers. *Journal of biomechanical engineering*, 135(9).
34. Journee, H. L., Postma, A. A., & Staal, M. J. (2007). Intraoperative neurophysiological assessment of disabling symptoms in DBS surgery. *Neurophysiologie Clinique/Clinical Neurophysiology*, 37(6), 467-475.



# Chapter 6

Measuring hand and finger movements to evaluate  
medication-induced symptom improvements in Parkinson's  
disease patients

*Based on:*

K.J. van Dijk et al., Measuring hand and finger movements to evaluate medication-induced symptom improvements in Parkinson's disease patients, To be submitted (2021).

## Abstract

*Objective:* In this study a measurement device called the Powerglove system is used to objectively measure the hand and finger movements of Parkinson's disease patients. From this, metrics are determined to describe the symptomatic improvement of medication on bradykinesia, one of the main Parkinson's disease symptoms.

*Approach:* The measurements are performed during a preoperative screening for deep brain stimulation at the hospital. During this hospital visit the patients will be in a medication on and off state, giving us the opportunity to evaluate the effect of medication on objective metrics derived from inertial sensing measurement of hand and finger movements. In total 35 patients participated in the study. Movements were recorded while performing standard bradykinesia scoring tasks such as finger tapping, rapid opening and closing of the hand, and rapid pro supination.

*Main result:* We found significant improvements in the inertial sensing-based metrics related to the angular velocity of the hand and fingers, caused by the medication intake. Interestingly, we did not find significant improvement in the movement amplitude parameters.

*Significance:* We found clinical relevant medication induced improvement in the inertial sensing-based metrics . In future studies, the presented metrics can be used in new wearable systems which are easier to wear during day to day tasks and in a home environment. This will give us interesting insights in the progress of the disease over the years and manifestation of the symptoms during the day.

## Introduction

Patients suffering from Parkinson's disease (PD) who are visiting a general practitioner or hospital are often asked to perform a number of quick and simple motor tasks. The movements that are used to perform these tasks are affected by the disease, as it is a degenerative neurological movement disorder. It is characterized by four typical motor symptoms; resting tremor, bradykinesia, rigidity and balance problems [1,2]. Resting tremor is the most commonly recognized symptom and is seen prominently at the distal part of the extremity [2]. Bradykinesia refers strictly to the slowness of performed movements. In addition, akinesia and hypokinesia are often considered to be part of this symptom. The first refers to difficulties to initiate a movement, poverty of spontaneous movements and freezing, and hypokinesia, refers to movements which are smaller than desired [3]. Rigidity refers to the phenomenon of increased resistance when stretching a muscle passively. Postural instability is due to the loss of postural reflexes, complicating walking and increasing the risk to fall, and is generally seen during the later stages of PD [2]. Because the disease cannot be diagnosed with a clinical scan or test during the patient's life, the diagnoses of the disease is limited to a subjective diagnose by visual assessment of the symptoms [4 18]. To do this in a structured manner, the unified Parkinson's disease rating scale (UPDRS) can be used by physicians [5 6].

The UPDRS is the most prominent rating scale used to understand the clinical features of PD in a patient. It consists of four sections with a number of items evaluating both non-motor and motor symptoms. Each item is rated using a scale ranging from zero to four, where zero indicates that the patient performs normally, while four indicates that the symptom in the patient is severe [5 6]. Currently, this is the most used method that is available to evaluate the severity of the symptoms in PD patients [2,7]. The scale can be used for diagnosing, detecting clinical improvement after medication intake, and to decide if a patient is eligible for other treatment methods such as deep brain stimulation (DBS). Unfortunately, when looking at the motor part of the UPDRS, the rating of the corresponding movements often vary between clinicians and may depend on the level of experience of the neurologist or movement disorder nurse. This subjective nature introduces extra variability to the UPDRS [11,12,13 ]. Furthermore, the current clinical examination is based on a short time interval, making it vulnerable to catch the patient in a clinical state which is not representative for its performance on a typical day [19]. Another disadvantage is that the current clinical examination may not be able to detect small changes as all items are only scored on a five-point scale. Besides, each single score may be dependent on multiple measures such as speed, amplitude, decrease in amplitude over time, and occurrence of hesitations [12 13]. The latter makes it impossible to detect if a change in score is due to deterioration of just one measure or a global deterioration on

all aspects of a symptom. To adequately study the PD motor symptoms, including the effects of medication or DBS and the fluctuations over a period of time, it is worthwhile to find an objective and quantified measure of the specific components of these symptoms.

Objective quantification of PD hand motor symptoms has been the subject of several studies [12-17]. In a previous proof-of-principal study by the authors, we proposed an alternative system to obtain accurate hand and finger kinematics in PD patients, called the Powerglove system [10]. This measurement system is a combination of miniature inertial and magnetic sensors on the finger segments and the back of the hand [8, 9]. Combination of these sensors enables a three dimensional reconstruction of the movements of the finger joints and the orientation of the hand. In this proof of principal study, multiple metrics, which were obtained in a normal clinical setting, have been shown to be influenced by the intake of medication. Therefore, it was concluded the system has the potential to be used for clinical research into PD motor symptoms without extensive changes to the clinical setting. At the time, this conclusion was based on the first four patients participating in a more extensive study.

In this paper we will present results from all the participating patients and we will focus on one of the main PD symptoms: bradykinesia. As the visual assessment during the UPDRS for this symptom especially relies on the assessment of the finger movements, we believe the detailed measurements of the Powerglove system will be advantageous in rating this symptom. The Powerglove system were tested on 35 PD patients during a preoperative screening for DBS at the hospital. During this hospital visit the patients was in a medication on and off state, giving us the opportunity to evaluate the effect of medication on inertial- and magnetic sensor based metrics. The measurement system's reliability was evaluated in a test-retest experiment design (intra- and inter-examiner) and a selection of the Powerglove metrics are presented to show the effect of medication on these metrics.

## Materials and Methods

### Subjects

In total 35 subjects participated in the study. Three subjects datasets were excluded for further analyses due to technical malfunctions of the measurement system or early termination of the experiment by the patient, both resulting in incomplete datasets. All subjects were recruited from the Academic Medical Center (AMC) in Amsterdam, the Netherlands, where they were admitted for an extensive two-day screening in order to become candidates for DBS surgery. Therefore, the subjects had to meet three inclusion criteria. First the occurrence of PD symptoms for more than five years which interfered

with daily life activities. Secondly a generally good response to dopaminergic medication but suffering from dopamine-dependent motor response fluctuations with or without levodopa induced dyskinesia. Finally, the patients had to be older than 18 years and be able to communicate in Dutch or English. Patients with a medical history other than PD which influenced hand movement or those who were unable to perform the required anatomical calibration were excluded from the experiment. The inability to correctly place the Powerglove sensor units on the patient's hand was another exclusion criterion. The study was approved by the local Medical Ethical Committee. Full written informed consent was obtained from all patients.

### **The Powerglove measurement system**

The Powerglove measurement system [8, 9] and the measurement procedure performed for this study is described in detail in the proof of principle study by the authors [10]. Summarized, the measurement device consists of multiple inertial and magnetic sensors to measure the angular velocity, linear acceleration and magnetic field at different segments of the hand. By using a patients specific kinematic hand model, an extended Kalman filtering on the sensor data, and a number of calibration steps, the position, orientation and joint angles of the hand and finger segments are obtained.

The sensor units of the Powerglove system were attached to the patients dorsal side of the hand and fingers using Velcro straps and tape (Figure 6-1). The finger sensor units were connected through a flexible printed circuit board to the sensor unit on the hand, and from this a cabled connection to a communication hub attached to the patients upper arm was made. From the two sensor units which were taped on the back of the hand, only the one connected to the index and middle finger string was used for the hand orientation. An additional sensor was attached to the dorsal side of the lower arm to be able to measure wrist kinematics, however this sensor was not used for evaluating the bradykinesia metrics that will be presented.

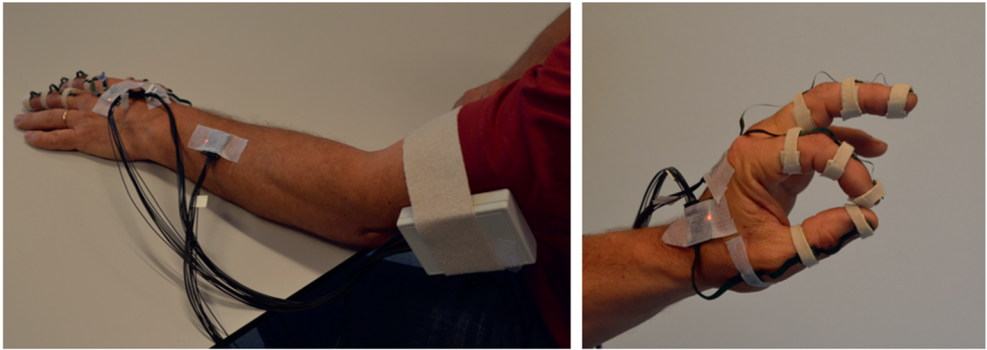


Figure 6-1 , the total Powerglove measurement system attached to the subject's arm, hand, and fingers, using Velcro straps and tape.

### Data analyses

The inertial sensor data for the bradykinesia analysis were obtained during the performance of three different tasks, finger tapping, rapid opening-closing of the hand, and pro-supination of the hand. The three tasks are already familiar to the patient since these same tasks are performed by the patient during standard UPDRS scoring of the bradykinesia characteristics. The performance of the tasks are assessed with the patient in two clinical states, by extracting metrics from the inertial sensor data. The first clinical state, is the medication off state. In this state, the three tasks were performed three different times by the patient and instructed by two individual raters (rater A and rater B). In the first three runs the tasks were instructed twice by rater A and once by rater B, the performance of this sequence (A1, A2 and B1) was randomized. The second clinical state, is the medication on state. In this state the three tasks were only performed once and was instructed by rater A one hour after the patient had its PD medication intake (A3). Additionally to the performance of the tasks to obtain the inertial sensor datasets, rater B, performed the complete UPDRS scoring of the patient in separate sessions to determine the severity of the two clinical states of the patient. The UPDRS scoring was performed, without the inertial sensor measurement system attached to the patient, and randomised before or after the inertial sensor measurements. A complete overview of the datasets is shown in Table 6-1.

Table 6-1, Overview of the acquired datasets. The performance of the sequence (A1, A2 and B1) was randomized. The complete UPDRS scoring was performed once for both clinical states by rater B.

	Medication off state				Medication on state	
datasets	A1	A2	B1	UPDRS-	A3	UPDRS- On
	(Rater A)	(Rater A)	(Rater B)	Off	(Rater A)	(Rater B)
				(Rater B)		

### Task 1: the finger tapping task

During this task the patient had to make a finger tapping movement as large and fast as possible. The inertial sensor system was used to determine five metrics to describe the performance of this task.

*Spectral Power:* The measurement of the angular velocity of the proximal segment of the index finger with respect to the hand was used to calculate the spectral power metric. Periodogram power spectral density estimate was used with a window size of three seconds and one second overlap to obtain the power spectral density of the measured signals per second. For each second the peak power within the movement frequency band, i.e. between 0 and 4 Hz, was taken and then averaged over the duration of the task.

*Frequency:* In the power spectral density per second, the frequency value of the corresponding peak power within the movement frequency band was taken and then averaged over the whole duration of the task.

*Maximum opening angular velocity:* For each finger tap, a single cycle, the maximum angular velocity of the proximal segment of the index finger with respect to the hand was taken and then averaged over all cycles. Cycles were detected using zero crossings of the angular velocity, which separate the opening and closing part. A zero crossing corresponds to zero angular velocity at maximum extension and maximum flexion of the index finger. Visual inspection was used to detect false cycle detections.

*Maximum closing angular velocity:* The same method as for maximum opening angular velocity was used except the maximum negative angular velocity was taken per cycle.

*Maximum angle amplitude:* For each cycle the amplitude of the flexion-extension angle of the proximal segment of the index finger with respect to the hand was taken and then averaged over all cycles.

### Task 2: rapid opening/closing of the hand

During this task the patient had to open and close his or her hand as large and fast as possible. The same five metrics of task 1 were used to describe its performance.

### Task 3: pro-supination of the hand

During this task the patient had to make a pro-supination movement of the hand as large and fast as possible. The inertial sensor system was used to determine four metrics to describe its performance.

*Spectral Power:* The same as the task 1 parameter except the angular velocity of the hand was used instead of the proximal segment of the index finger.

*Frequency:* see task 1

*Maximum pronation angular velocity:* For pronation, during a single cycle, the maximum angular velocity of the hand was taken and then averaged over all cycles. Cycles were detected using zero crossing of the angular velocity, which separate the pronation and supination movement. A zero crossing corresponds to zero angular velocity at maximum pronation and maximum supination of the hand.

*Maximum supination angular velocity:* The same method as the maximum opening angular velocity was used except the maximum negative velocity was taken per cycle.

## Statistical analyses

Statistical analyses is performed on the metrics over the different datasets as introduced in the previous section (Table 6-1). A distinguish is made between clinical and methodical comparisons. In the clinical comparison the difference between the clinical on and off medication state is made. The methodical comparisons are made to analyse the experimental method by looking at the UPDRS correlation and reliability of the measurement system.

### Comparison between on and off medication

Two way analyses of variance (ANOVA) was used to find the significant differences between the parameters in medication on and off state, i.e. A1 – A3, A2 – A3, and B1 – A3. Differences were considered significant when the p value was smaller than 0.05.

### UPDRS correlation

For each parameter described above, the correlation was determined between the parameter value and the corresponding UPDRS sub-score, i.e. UPDRS section 3.4 for finger tapping, 3.5 for rapid opening/closing and 3.6 for pro-supination. The UPDRS scores that were obtained in both on and off medication state and the Powerglove parameters obtained in session A1 and A3 were part of the dataset. Correlation was described by the spearman rho coefficient and was considered to be significant when the p value was smaller than 0.05.

### Reliability

The inter-rater reliability and intra-rater reliability of the measurements were determined by using the interclass coefficients (ICC). ICC relates the measurement error to the variability between subjects. An ICC value of above 0.6 was considered to be moderate and above 0.7 to be good. The intra-rater reliability was calculated by using measurement data from rater A i.e. A1 and A2 and the inter-rater reliability was calculated using measurement data from rater A and B i.e. A1 and B1.



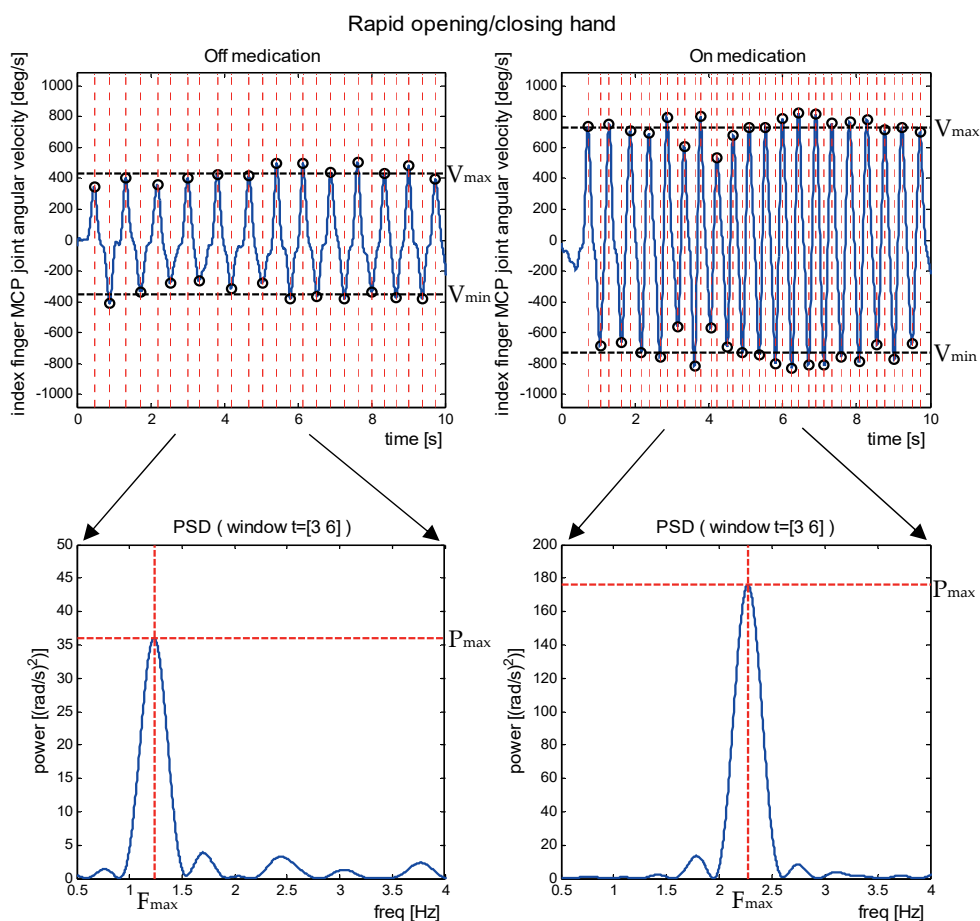


Figure 6-2, shows a typical example of the angular velocity and spectral power metrics used in the performance assessment during the rapid opening and closing of the hand task. Four graphs are shown of which the left column is measured while the patient is without medication and the right column with the same patient with medication. The top row of the four graphs are the time domain plots of the MCP joint angular velocities. The bottom row are the spectral density plots based on the three second time window, in this example between the third and sixth second. In the time domain plots the local maximum and minimum during each cycle, i.e. one opening and closing movement, are denoted with the black circles. The  $V_{max}$  dotted line presents the mean local maximum over all cycles and corresponds to the opening angular velocity metric which is introduced in the method section. The  $V_{min}$  dotted line presents the mean local minimum over all cycles and corresponds to the closing angular velocity metric. The  $P_{max}$  and  $F_{max}$  dotted lines presents the maximum angular velocity power and frequency within this particular 3 seconds time window. This mean value of  $P_{max}$  and  $F_{max}$  over all time windows during the complete task, corresponds to the spectral power and frequency metric which are introduced in the method section.

## Results

Figure 6-2, gives an example of the inertial sensing recordings of the angular velocity of the MCP joint angle during rapid opening and closing of the hand, for one patient with and without medication. The metrics related to the power, frequency, and angular velocity are highlighted in the figure by the dotted lines. Table 6-2, 6-3 and 6-4 show the complete results of analyzed metrics for the three different tasks for all patients. Table elements are coloured green in case of significant differences between on and off medication stat (p value smaller than 0.05), and significant spearman correlation with the corresponding UPDRS score (p value smaller than 0.05),. Table elements are coloured in blue in case of good reliability scores , ICC scores  $\geq 0.7$ .

Table 6-2, TASK 1: Finger tapping. The table shows 1 column with 4 sub columns for the clinical comparison between the medication on state and off state, i.e. A1-A3, A2-A3 and B1-A3. For this comparison the elements are denoted in green when the medication off state was significantly different from the medication on state ( $p < 0.05$ ). The table shows 1 column with 3 sub columns for the methodical statistical analysis. The table elements are coloured blue in case of good reliability score ( $ICC \geq 0.7$ , with ICC inter: A1-B1, and ICC intra: A1-A2). The table elements for the Spearman rho correlation are coloured green in case of a significant spearman correlation with the corresponding UPDRS score.

	Clinical				Methodical		
	A1 med off	A2 med off	B1 med off	A3 med on	ICC inter	ICC intra	Spearman rho
Spectral Power [(rad/s) <sup>2</sup> ]	57±46	60±50	58±57	93±67	0.70	0.68	-0.39
Frequency [Hz]	2.4±0.9	2.8±0.9	2.5±1.1	2.9±0.8	0.59	0.48	0.01
Opening angular velocity [deg/s]	321±149	327±149	321±160	401±155	0.85	0.70	-0.30
Closing angular velocity [deg/s]	355±166	355±155	350±166	424±160	0.81	0.68	-0.33
Angle amplitude [deg]	42±19	38±16	41±20	43±18	0.58	0.47	-0.23

Table 6-3, TASK 2: Rapid opening and closing of the hand. Related Table description is described in detail for Table 6- 2.

	Clinical				Methodical		
	A1 med off	A2 med off	B1 med off	A3 med on	ICC inter	ICC intra	Spearman rho
Spectral Power [(rad/s) <sup>2</sup> ]	66±57	75±62	67±57	140±89	0.63	0.64	-0.41
Frequency [Hz]	1.7±0.6	1.8±0.7	1.6±0.5	2.2±0.7	0.76	0.59	-0.41
Opening angular velocity [deg/s]	390±160	395±166	413±195	556±189	0.62	0.68	-0.41
Closing angular velocity [deg/s]	390±183	407±172	401±212	579±201	0.81	0.77	-0.42
Angle amplitude [deg]	63±22	76±53	69±30	76±25	0.26	0.57	-0.24

Table 6-4, TASK 3: pro- supination hand. Related Table description is described in detail for Table 6-2.

	Clinical				Methodical		
	A1 med off	A2 med off	B1 med off	A3 med on	ICC inter	ICC intra	Spearman rho
Spectral Power [(rad/s) <sup>2</sup> ]	182±179	161±156	151±147	283±187	0.69	0.83	-0.50
Frequency [Hz]	2.1±0.8	2.1±0.9	2.1±0.9	2.5±0.7	0.77	0.73	-0.22
Pronation angular velocity [deg/s]	527±252	510±264	516±275	710±281	0.63	0.80	-0.46
Supination angular velocity [deg/s]	556±264	527±269	533±298	722±275	0.65	0.80	-0.47

## Discussion

In this study we focussed on measuring the finger and hand movements to study the important PD symptom bradykinesia. This symptom is often assessed in a clinical setting by visual inspection of the movements of the fingers and hands during given tasks. A novel measurement device called the Powerglove system, a system consisting of multiple accelerometers, gyroscopes and magnetometers, was used to record the movements of 35 patients during these commonly given tasks at the clinic. The analyses of the recordings showed interesting significant improvements in the patients performance after intake of PD medication compared to the off-medication state. In the three tasks we asked the patient to perform finger tapping, rapid opening and closing of the hand, and rapid pronation movement of the hand. All metrics related to angular velocity showed significant improvement. That is, the angular maximum velocity during the cycles went higher after medication intake, and also the power in the angular velocity signal increased. With the increase of angular velocity also the frequency of the cyclic movement significantly increased.

Interestingly, the amplitude of the movement during finger tapping and hand opening and closing did not change significantly. Before the performance of these tasks the patient got instructions to make the movements as large and as fast as possible. So, we did not distinguish specifically between one task with large movements and another task with fast movements. Therefore, we cannot conclude from this that medication intake had no effect on amplitude at all. However, while performing the movements the patient seems to have used a strategy where the focus was more on improving speed then improving amplitudes of the movement.

When looking at the relation between the UPDRS scores of the patient and the studied Powerglove system metrics, we found significant correlations. All significant correlations were negative, which was expected as the velocity, power and amplitudes decreased with the severity of the rated symptom. All correlations of the single metrics were low, this means that none of the correlations were above 0.5. Firstly, this can be explained as the UPDRS scoring is not based on a single parameter. Instead it is based on multiple factors such as speed, amplitude, smoothness of the movements, freezing and regularity [5, 6]. Secondly, our experiment inclusion criteria was focussed on the clinical comparison between medication on and medication off state. There was no criteria to obtain an uniform distribution of UPDRS scores. A third factor which played a role, was fatigue. In previous studies, which showed higher correlations, measurements were performed in short ten seconds dedicated tests focussing on just one task [15], or performing

measurements over multiple days [20], averaging factors such as fatigue out of the equation.

Measurements of the patients movement were performed with a novel measurement device called the Powerglove, an device based on inertial sensing measurement of hand and finger movements [8]. While the Powerglove can be used to asses numerous variables related to the hand and finger movements we made a strict selection of only five metrics related to angular velocities, amplitudes, frequencies and power. In a previous study by the authors a selection of signals and metrics were already introduced to study PD symptoms [10]. The metrics in the current study were solely based on movements of the sensors on the back of the hand and the sensors on the proximal phalange of the index finger. De Vries et al. also showed that with similar reduction in the amount of sensor information it was still possible to distinguish between coordinated movements to detect grasping during reaching [21]. The main advantage is that , all metrics can be obtained with a large reduction of sensors which needs to be attached to the fingers and hand, since an often mentioned reason for not introducing objective methods of quantification in the clinical setting is additional complexity and time involved [12]. A reduction of sensors will be advantageous in designing wearable systems tailored for PD patients, which is easier to attach and less intrusive to wear.

The inter-rater and intra-rater reliability analyses gave us mixed results. Each rater gave the task instructions to the patient, before the performed hand and finger movements were recorded and the metrics were determined. Only the opening angular velocity during finger tapping tasks, closing angular velocity during rapid hand opening tasks, and the frequency during the pro-supination tasks showed good reliability for both intra- and inter-rater measurements. For the pro-supination task all other metrics had a good intra-rater reliability, however not a good inter-rater reliability. The rapid hand opening task only the frequency parameter had a good inter-rater reliability. For finger tapping on the other hand, the frequency parameter did not have a good reliability, whereas the power and closing velocity had good inter-rater reliability. Previous studies on the Powerglove show the measurement is able to measure movements reliably and accurately [9]. A reason for the low reliability of measurement can be that the state of the patient is highly fluctuating in the studied timeframe. The individual rated measurements were short , minute to sub minute, time fragments, repeated by the other rater 15 to 30 minutes later. Within this timeframe symptoms can deteriorate due to multiple factors such as fatigue and remaining PD medicine wearing off. Of course, this not only affects clinical assessment by measurement devices based on objective inertial sensing recordings, it also affects clinical assessment through subjective rating of the UPDRS. Therefore this is a

major problem for any clinical assessment which is performed once in a short time window.

Using the Powerglove technology in a wearable is where we foresee its real potential. The technology based on inertial sensing, combines the multiple sensor signals to reconstruct the hand and finger movements. The big advantage of this method is that you can distinguish fine finger movement from the larger movements of the complete body, arm and hand. This in contrast to commercially available wearables used for activity trackers. This study shows the technology is able to track this fine finger movement and is sensitive to changes in the clinical state of the patient. Monitoring the patient's ability to do fine finger movements and the development throughout the day, months and years, will give valuable information for the patient and caretakers that can be used to create tailor-made medication intake schedules and prescribed doses. An interesting combination will be a wearable based on the Powerglove technology and questionnaires, which can be answered on mobile phone applications [22, 23]. The latter is a less objective measure than those obtained from wearable sensors. However, the more subjective nature of the questionnaires takes into account the patient's interpretation of the motor symptoms and non-motor symptoms and its effects on the quality of life. This combination will give additional insight in which improvement of which metrics the patient values most.

## Conclusion

In this study we found clinically relevant and significant improvement in the system outcome metrics, based on only the sensors on the back of the hand and proximal phalange of the index finger. In future studies, this reduction of sensors allows a redesign of the Powerglove system, to make it easier to wear during day to day tasks and in a home environment. This will give us interesting insights in the progress of the disease and manifestation of the symptoms during the day, it can help in the need to take Parkinson's care to the home [24].

## References:

1. Gelb DJ, Oliver E, Gilman S. Diagnostic Criteria for Parkinson Disease. *Arch Neurol*. 1999;56(1):33–39. doi:10.1001/archneur.56.1.33
2. Jankovic J Parkinson's disease: clinical features and diagnosis *Journal of Neurology, Neurosurgery & Psychiatry* 2008;79:368-376.
3. A. Berardelli, J. C. Rothwell, P. D. Thompson, M. Hallett, Pathophysiology of bradykinesia in Parkinson's disease, *Brain*, Volume 124, Issue 11, November 2001, Pages 2131–2146
4. Eduardo Tolosa, Gregor Wenning, Werner Poewe, The diagnosis of Parkinson's disease, *The Lancet Neurology*, Volume 5, Issue 1, 2006,
5. Goetz, C. G., P. A. LeWitt, and M. Weidenman. Standardized training tools for the UPDRS activities of daily living scale: newly available teaching program. *Mov. Disord*. 18(12):1455–1458, 2003.
6. Goetz, C. G., B. C. Tilley, S. R. Shaftman, G. T. Stebbins, S. Fahn, P. Martinez-Martin, W. Poewe, et al. Movement Disorder Society-sponsored revision of the Unified Parkinson's Disease Rating Scale (MDS-UPDRS): scale presentation and clinimetric testing results. *Mov. Disord*. 23(15):2129–2170, 2008.
7. Ramaker, C., Johan Marinus, Anne M. Stiggelbout and Bob J van Hilten. "Systematic evaluation of rating scales for impairment and disability in Parkinson's disease." *Movement disorders : official journal of the Movement Disorder Society* 17 5 (2002): 867-76 .
8. Kortier, H. G., V. I. Sluiter, D. Roetenberg, and P. H. Veltink. Assessment of hand kinematics using inertial and magnetic sensors. *J. Neuroeng. Rehabil*. 11:70–83, 2014.
9. van den Noort, J. C., H. G. Kortier, N. van Beek, H. E. Veeger, and P. H. Veltink. Measuring 3D hand and finger kinematics—a comparison between inertial sensing and an opto-electronic system. *PLoS ONE* 11(11):16, 2016
10. van den Noort, J. C., Verhagen, R., van Dijk, K. J. *et al*. Quantification of Hand Motor Symptoms in Parkinson's Disease: A Proof-of-Principle Study Using Inertial and Force Sensors. *Ann Biomed Eng* 45, 2423–2436 (2017) doi:10.1007/s10439-017-1881-x
11. Post, B., M. P. Merkus, R. M. A. De Bie, R. J. De Haan, and J. D. Speelman. Unified Parkinson's disease rating scale motor examination: Are ratings of nurses, residents in neurology, and movement disorders specialists interchangeable? *Mov. Disord*. 20(12):1577–1584, 2005
12. Patrick, S. K., A. A. Denington, M. J. A. Gauthier, D. M. Gillard, and A. Prochazka. Quantification of the UPDRS rigidity scale. *IEEE Trans. Neural Syst. Rehabil. Eng*. 9(1):31–41, 2001.
13. Pulliam, C. L., D. A. Heldman, T. H. Orcutt, T. O. Mera, J. P. Giuffrida, and J. L. Vitek. Motion sensor strategies for automated optimization of deep brain stimulation in Parkinson's disease. *Parkinsonism Relat. Disord*. 21(4):378– 382, 2015.

14. Heldman, D. A., J. Jankovic, D. E. Vaillancourt, J. Prodoehl, R. J. Elble, and J. P. Giuffrida. Essential tremor quantification during activities of daily living. *Parkinsonism Relat. Disord.* 17(7):537–542, 2011.
15. Jun, J. H., J. W. Kim, Y. Kwon, G. M. Eom, S. B. Koh, B. Lee, H. S. Kim, et al. Quantification of limb bradykinesia in patients with Parkinson's disease using a gyrosensor—improvement and validation. *Int. J. Precis. Eng. Manuf.* 12(3):557–563, 2011.
16. Koop, M. M., A. Andrzejewski, B. C. Hill, G. Heit, and H. M. Bronte-Stewart. Improvement in a quantitative measure of bradykinesia after microelectrode recording in patients with Parkinson's disease during deep brain stimulation surgery. *Mov. Disord.* 21(5):673–678, 2006.
17. Tavares, A. L. T., G. S. X. E. Jefferis, M. Koop, B. C. Hill, T. Hastie, G. Heit, and H. M. Bronte-Stewart. Quantitative measurements of alternating finger tapping in Parkinson's disease correlate with UPDRS motor disability and reveal the improvement in fine motor control from medication and deep brain stimulation. *Mov. Disord.* 20(10):1286–1298, 2005.
18. Dickson, Dennis W., et al. "Neuropathological assessment of Parkinson's disease: refining the diagnostic criteria." *The Lancet Neurology* 8.12 (2009): 1150-1157.
19. Maetzler, Walter, et al. "Quantitative wearable sensors for objective assessment of Parkinson's disease." *Movement Disorders* 28.12 (2013): 1628-1637.
20. Griffiths, R. I., Kotschet, K., Arfon, S., Xu, Z. M., Johnson, W., Drago, J., ... & Horne, M. K. (2012). Automated assessment of bradykinesia and dyskinesia in Parkinson's disease. *Journal of Parkinson's disease*, 2(1), 47-55.
21. de Vries, J. C., van Ommeren, A. L., Prange-Lasonder, G. P., Rietman, J. S., & Veltink, P. H. (2018). Detection of the intention to grasp during reach movements. *Journal of Rehabilitation and Assistive Technologies Engineering*, 5, 2055668317752850.
22. Habets, J. G., Heijmans, M., Kuijf, M. L., Janssen, M. L., Temel, Y., & Kubben, P. L. (2018). An update on adaptive deep brain stimulation in Parkinson's disease. *Movement Disorders*, 33(12), 1834-1843.
23. Bayés, À., Samà, A., Prats, A., Pérez-López, C., Crespo-Maraver, M., Moreno, J. M., ... & de Barros, A. C. (2018). A "HOLTER" for Parkinson's disease: Validation of the ability to detect on-off states using the REMPARK system. *Gait & posture*, 59, 1-6.
24. Dorsey, E. R., Vlaanderen, F. P., Engelen, L. J., Kieburtz, K., Zhu, W., Biglan, K. M., ... & Bloem, B. R. (2016). Moving Parkinson care to the home. *Movement Disorders*, 31(9), 1258-1262.



# Chapter 7

General discussion

## Overview

In this thesis, I presented our research which had the goal to improve current deep brain stimulation (DBS) technology, with focus on bringing the conventional DBS system a step closer to adaptive DBS, a personalized DBS therapy. The chapters in this thesis can be seen as individual building blocks for an adaptive DBS system (Figure 7-1). After the introductory chapter, in the second and third chapter, two novel DBS lead designs were studied in a detailed computational model. Both leads contained multiple (small) contacts, divided over the circumference of the electrode, which enables directional steering stimulation. In the computational model both leads were able to exploit the novel distribution of the electrode contacts to shape and steer the stimulation field to activate more neurons in the chosen target or to counteract lead displacement. In the fourth chapter, an important issue concerning the previous studied novel lead designs and their highly increased degrees of freedom in shaping the stimulation field is addressed. A current source density (CSD) method is applied on local field potentials (LFP) measured using a probe consisting of 16 electrodes positioned at multi locations providing a 3D measurement grid in an animal model. This method allowed us to locate sources of dendritic activation within the subthalamic nucleus (STN), evoked by cortical stimulation. A distinguished pattern of sources was found within the STN related to the dendritic activation by neural hyper-direct and direct pathways, transferring information from the activated cortex, through the basal ganglia to the thalamus, and back to the cortex. This pattern of CSD sources can act as a landmark within the STN to locate the DBS target and can guide the adaptive DBS system in finding the correct steering direction and shaping of the directional stimulation field. The fifth and sixth chapter described the last building block of the DBS system. We introduced an inertial sensors and force sensor based measurement system, which can be used to record the hand kinematics and joint rigidity of Parkinson's Disease (PD) patients. The fifth chapter describes the experimental methods on how this system can be used to objectively monitor three of the main PD symptoms, i.e. tremor, bradykinesia and rigidity. The last chapter zooms in on bradykinesia. The sensor system and the metrics distilled from the measurement data was proven to be sensitive to detect clinical changes. Multiple metrics showed significant changes between the PD patient's state when he/she was off medication and after his/her medication intake. Metrics sensitive to changes in the clinical state of the patient, which can act as a feedback signal in an adaptive DBS system, are the last building block of the DBS system.

In the remainder of this chapter I will place our findings in a broader perspective. The individual building blocks as well as the future goal of a complete adaptive DBS system can all be considered as part of the broader research theme: personalized therapy. This is a popular and promising topic in the treatment of many diseases and specifically in PD.

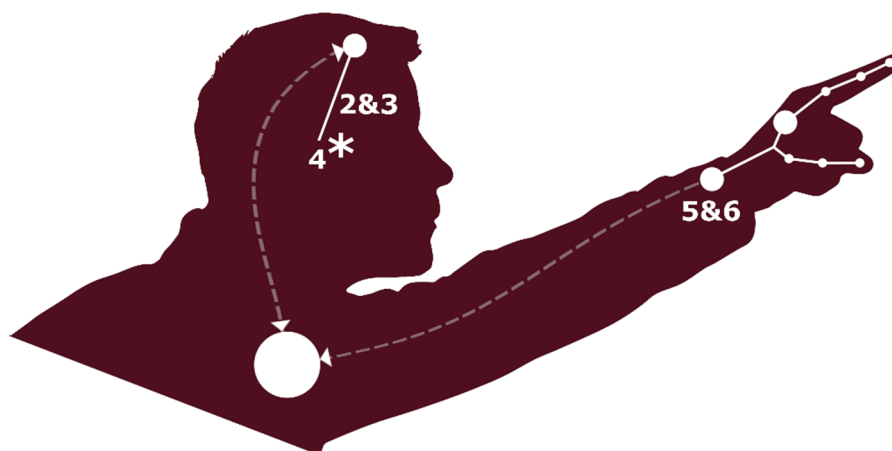


Figure 7-1, A graphical representation of the adaptive DBS system, including the thesis chapter numbers in which on that specific part of the system is elaborated; i.e. Chapter 2&3 focus on novel DBS leads, Chapter 4 on electrophysiological signals measured in the DBS target, and Chapter 5&6 describes the quantitative measurement of PD symptoms.

## Personalized therapy

In the last two decades, with the sequencing of the human genome, many enthusiastic predictions have been done to accomplish better disease prevention and drug treatment, based on the knowledge of the individual patient [1]. This gave a large boost to personalized therapy, especially in cancer research. The National Institutes of Health and the Food and Drug Administration formulated their vision: “to support in the best way to develop new therapies and optimize prescribing by steering patients to the right drug at the right dose at the right time” [2]. In the light of this thesis I would translate this to: optimize the new DBS therapy at the right stimulation location in the right direction at the right time.

## Sensing

To design a personalized DBS therapy one needs to acquire patient-specific information. We can distinguish patient-specific information used for temporal feedback or spatial feedback. Spatial feedback signals are used to determine the correct lead location per patient and to determine the location of patient-specific ‘sweet spots’ of the stimulation field. Temporal feedback signals are used to determine when to stimulate and to determine the clinical state of the PD patient.

## Spatial feedback signals

Correct placement of the DBS lead in the target is an important step in the DBS therapy, and highly affects the clinical outcome [3]. Even small displacements can already reduce the positive effects and can cause the occurrence of cognitive and limbic alterations [4]. Therefore, a lot of effort is taken nowadays in creating patient-specific anatomical models to aid in the stereotactic planning. In the early days, the localization had to be performed on low field, 1.5 Tesla, magnetic resonance images (MRI). However, with this low resolution and low signal to noise ratio MRI it is difficult to differentiate between the target structure and the adjacent structures. With the introduction of the ultra-high field 7 Tesla MRI, it was possible to create successfully patient-specific 3 dimensional (3D) models of the STN and other nearby brain structures [5]. Using the diffusion tensor imaging (DTI) out of the ultra-high field MRI enabled distinguishing motor regions from the neighbouring associative and limbic areas suggesting ultra-high field MRI may facilitate individualized and highly specific planning of deep brain stimulation surgery of the STN [6]. In the next section on actuation I will discuss how these detailed patient-specific models of the STN can also be used as input for the computational models described in Chapter 2 and Chapter 3.

Besides imaging, electrophysiological recordings can be used to create patient-specific 3D models of the target [7]. The study presented in Chapter 3 also relates to this topic. The CSD sources can act as a landmark to localize the individual patient's brain structures. While the study presented in this thesis focussed on the CSD method in an animal model experiment, experiments with cortically evoked potentials were also performed in humans to identify the motor region of the STN [8]. Nevertheless, the method we presented in this thesis is still academic. Instead of evoking the potentials in the cortex and measure the resulting LFP in the STN, it is also possible to do it the other way around. These electrophysiological signals measured at the cortex are also suggested to act as a feedback signal in an adaptive DBS therapy [9], and the origin of the sources are studied in detailed computational models [10]. Other studies on the localization of LFP sources in the STN are not based on cortical evoked potentials, but are based on the increased oscillatory beta waves occurring in the STN in PD patients. Finding the direction of these sources has been performed in humans with an electrode comparable to the electrode designs described in Chapter 2 [11] and Chapter 3 [12]. These studies looked at the electrode picking up the highest power in the beta band (8-35 Hz) and did not reconstruct the CSD to pinpoint the oscillatory activation of the synaptic input. A promising future step would be to develop a CSD method to analyse measurements performed with clinical available directional DBS leads, such as the 8 channel lead described in Chapter 3. The CSD method we used in the animal study assumed a regular square measurement grid. A

possible solution for this practical problem can be offered by an advanced CSD method based on mathematical kernel methods, which can provide a nonparametric estimation of CSD from LFP recorded from arbitrarily distributed electrodes [13].

### Temporal feedback signals

To determine when to stimulate we will discuss two types of signals, i.e. electrophysiological signals in the brain and recordings of movements of the body or body parts. First, electrophysiological signals can not only be used as a spatial feedback signal as we explained in the previous section, it can also be used for temporal feedback. Especially the LFP signals have a huge practical advantage, as these signals can be measured with the already implanted DBS electrode. New-generation DBS pulse generators can already record LFP signals, which have been correlated with clinical symptoms in several studies. For example, decreased beta band activity in the STN by dopaminergic medication and/or DBS has been correlated with improved akinesia, bradykinesia, and rigidity [14-16]. This suggests these signals can be used to determine when to stimulate.

Another type of feedback signals are the recordings of movements, which is a very direct and intuitive way of measuring when the patient is suffering from motor symptoms the most. Driven by the fast technological advances in Micro-Electro-Mechanical Systems (such as accelerometers and gyroscopes), low-power wireless communication protocols (such as Bluetooth low energy, ANT and Zigbee), the constantly increasing energy density in battery cells and increasing low power computation power driven by the smartphone and wearables market, we see that the most promising trends involve sensor devices, which are low cost, low power, unobtrusive, and accurate in the measurements, for monitoring and managing the pathology [17]. In Chapter 5 and 6 of this thesis we presented a number of metrics based on the recordings of an inertial sensor based measurement device we called the Powerglove. The novelty of this system was the combination of sensory data from multiple segments of the hand and fingers. This allowed to distinguish between the fine motor skills of the fingers and the coarser movements of the whole hand. Unfortunately, this Powerglove is not yet a low power, wireless and unobtrusive device. Luckily, the presented way of signal processing can easily be transferred to a new design with only two sensor units, which needs to be attached to two connected hand and/or finger segments. This would result in an unobtrusive system which is sensitive to changes in the clinical state of the patient. Please note, updating the hardware only, will not instantly make it a practical clinical tool. Presenting the data as shown in chapter 5 and 6 is only useful in a research setting. Presenting the signals and metrics in an easy and meaningful way to the patient and clinician, is just as important as

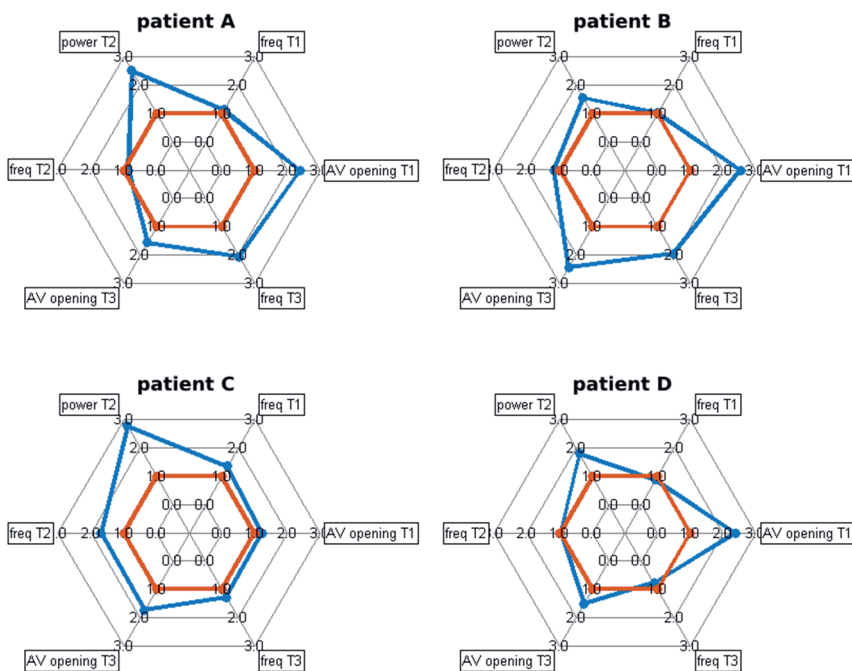


Figure 7-2, Spider plots of four individual patients, the blue line showing the medication intake induced changes in six metrics relative to the normalized value of the metric in medication off-state (red line). The six presented metrics are a selection of the metrics presented in Chapter 6, two metrics per task, i.e. finger tapping task (T1), pro-supination of the hand task (T2), and rapid opening and closing of the hand task (T3). For all tasks the frequency (freq T1-3) metric is shown, for T1 and T3 the maximum angular velocity during opening of the finger/hand (AV opening T1/T3), and for T2 the spectral power in the movement band (between 0 and 4Hz) (power T2).

the hardware in terms of usability. Commercial available systems such as the Personal KinetiGraph wristwatch (Global Kinetics Pty Ltd, Melbourne, AU), and the Kinesia assessment system (Great Lakes NeuroTechnologies, Cleveland, USA) already combine a simple measurement tool (inertial sensors on one segment) and easily interpreting clinical outcome metrics. Future work should show how much such a system will benefit from adding one sensor unit on another segment to assess the fine relative movements.

Chapter 6 presented metrics to objectively observe changes in the patient's performance in a finger tapping task, a rapid opening and closing of the hand task, and a hand pro-supination task, between the medication on- and off state. On a group level multiple metrics showed significant changes between the two clinical states. Instead of focussing on a group level, the same metrics can give interesting insights to be used in the personalized therapy field. Figure 7-2 is an unpublished figure, created with the metrics obtained in Chapter 6. It shows the change in the metrics for the three tasks, induced by

the medication intake on patient level for four individual patients. The shapes of the blue lines are different for each individual patient, suggesting each patient reacts differently to the medication and needs a patient-specific approach in rating the metrics. Besides, this figure points out the necessity to combine metrics to get an overall view of the clinical state of the patient. Currently, a lot of effort is put in to combine metrics from wearable systems using all different types of machine learning approaches (see overview [17]). Also, deep learning techniques are proposed as a promising method to analyse wearable sensor data. The deep learning techniques have multiple advantages such as there is no need to rely on expert-defined features and the analysis procedure resembles what human experts do, since the whole signal segment is rated with one output [18].

## Actuation

In the next section we will discuss the actuation part for a personalized DBS system. Two topics will be addressed: Firstly the lead design and secondly the programming of the actuation settings.

### Lead designs

To design a better personalized DBS therapy it helps to have high degrees of freedom to shape the electric stimulation field. The conventional lead consists of four cylindrical contacts, which limits shaping the stimulation field to varying the radius and height surrounding the lead. In the last decade, multiple companies started developing leads with multiple electrode contacts divided over the circumference of the lead. This technological advance was the beginning of directional DBS. In this thesis, two of those leads were studied and showed the potential of directional DBS in a detailed computational model. During the writing of these chapters and in the years after, multiple clinical trials were started to study directional DBS in human patients. From these studies it can be concluded that directional DBS increases the therapeutic window (i.e. the difference between the minimum stimulation current required to produce adverse effects and the current required to produce a beneficial effect) [19,20, 21] and suggesting directional DBS may be able to compensate for small displacements of the lead from the target [22,34]. The goal of using computational modelling will then no longer be, as presented in this thesis, to demonstrate the potential and limitations [23] of directional DBS, but will be of great value in finding the optimal stimulation settings for each individual patient.

### Programming

With the conventional DBS lead, the stimulation settings were often obtained on an empirical basis with stimulation applied through one or two electrode contacts, with a fixed stimulus frequency of around 120–180 Hz, 60–200  $\mu$ s pulse width and 1–5 mA or 1–

5 V stimulation amplitude [24]. This already gives many options to manually find the optimal settings and in combination with the directional DBS lead, this even increases. Computational models as we presented in Chapter 2 and 3 can aid the PD nurse or physician in finding these settings. The models used in this thesis were based on an average human brain. With the help of the ultra-high field MRI techniques we described in the previous ‘sensing’ section, patient-specific models can be made of the brain tissue to define the boundaries of the optimal target region and those inducing side-effects including neuron fiber tracts such as the Internal Capsula. Once these regions have been identified, a computer program can search for the optimal solution, i.e. the stimulation amplitudes per electrode contact. In this thesis we only implemented a simple brute-force search to find the solution for a possible optimal target region. To decrease computation time, which is necessary in a practical application, ‘smarter’ optimization techniques should be utilized. In a recent paper [25], which uses a computational model of the brain tissue and DBS lead designs similar to the models presented in this thesis, an optimized programming algorithm for cylindrical and directional DBS leads was presented. However, instead of generating the solutions of complex cable models for all neurons in the model, as we did in this thesis and which is time-consuming, they approximated the extracellular electrical stimulation by the second spatial derivative of the electric potential along the nodes of Ranvier of the axons in 3D space. This allowed them to predict, in a fast way, activation along fiber tracts and boundaries of nuclei, and to find the optimal stimulation settings in 0.1-10 seconds.

A remaining question is: what are the correct targeting constraints to find the optimal stimulation settings? Activating as many STN cells as we have assumed to produce the best clinical outcome is probably incorrect as the nucleus also contains non-motor parts. Studies even showed that the therapeutic effects of DBS are related to activation of passing fiber tracts. such as axons from the pallidothalamic pathway (lenticular fasciculus) [26], stimulation of the cerebellothalamic pathway (dentatothalamic tract) for tremor control [27], and/or the hyperdirect pathway for rigidity improvements [28]. Therefore it remains important to continue combining patient-specific computational models and known clinical outcomes for improving the exact identification of the ‘sweet spot(s)’ for stimulation [29]. Once we have a better understanding in the sweet spots for stimulation, a re-evaluation of the lead designs can easily be performed in our computational models, to assess the stimulation performance in targeting the neurons or axons in the sweet spot.

## Adaptive DBS

In this final chapter we will discuss how sensing and actuation can be combined to design a complete personalized and adaptive DBS system.



Firstly, the adaptive DBS system can be controlled with feedback signals from electrophysiological recordings. Different recordings can be used, for example electrocorticography using a subdural grid, surface electromyography, or LFP recordings. Especially the LFP recordings are promising because they can be picked up by the DBS lead. Multiple proof-of-principle studies with a closed loop adaptive DBS strategy, based on the beta power in the LFP signal, showed improvement of the DBS therapy compared to conventional open-loop DBS therapy [16], or approximately equivalent efficacy with respect to conventional DBS, but with less than half the stimulation delivered [30]. With clinical experiments with freely moving patients [31] and sessions up to 8 hours [32] this type of adaptive DBS therapy has been shown to be a safe improvement. This thesis suggests another type of adaptive DBS based on localization of LFP sources. This directional feedback might be another way to expand the electrophysiological signal based adaptive DBS.

Secondly, adaptive DBS can also be controlled with feedback signals from wearable sensors. Studies based on tremor detection have supported the feasibility, effectiveness, and efficiency of wearables-based adaptive DBS [33]. To implement adaptive DBS controlled by wearables to monitor other cardinal motor symptoms than tremor further development and clinical validation is needed [16]. In this thesis, we presented an inertial sensor based measurement system, which was able to monitor all cardinal PD symptoms. In Chapter 6 multiple metrics were presented to monitor the effect of medication on bradykinesia. On a group level these metrics showed to be sensitive to the patients' clinical state. The same dataset also showed interesting results at the individual patient level. Figure 7-3 (unpublished), shows the angular velocity of the wrist during the performance of a pro-supination task. The first three measurements were recorded with the patient in a medication off state, while the fourth measurement was recorded with the patient in a medication on state. On average, in the first three measurements, the performance of the task was worse than the fourth measurement, i.e. lower amplitude, lower frequency in the first measurement, and hesitations in the third measurement. However, in the second measurement it can be seen that the performance was actually very good and similar to the performance in the medication on state. This suggests that data obtained with a wearable sensor system similar to the one presented in this thesis contains information, which can be used as input of an adaptive DBS system to intervene at the right time when the patient is struggling in performing fine-motor tasks.

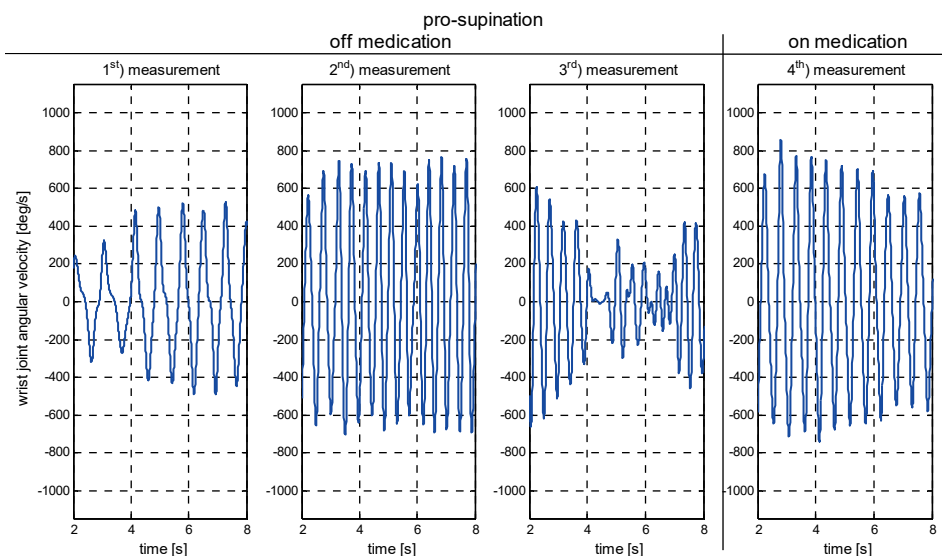


Figure 7-3, wrist joint angular velocity of one individual patient during the performance of a pro-supination task. From left to right: the first three measurements were recorded while the patient was in a medication off state, while the fourth measurement was recorded with the patient in a medication on state.

## Final conclusion

In this thesis we presented multiple building blocks for an adaptive DBS system, which will contribute to an improved personalized therapy. Many of the topics are being followed up by the scientific field, improving the computational models, initiating proof-of-principle studies on human patients, conducting clinical-trials, and bringing technology to the clinic.

One final topic which is still open and which I believe can be of added value to the therapeutic effect of DBS, is directional adaptive DBS. Studying this requires combinations of clinical experiments over multiple days, computational modelling, recordings of LFP signals near the stimulation target and unobtrusive ways of monitoring cardinal PD motor symptoms. This leads to my final recommendation for three future studies:

1. Designing a CSD method for the clinical approved 8 channel directional DBS lead.
2. Perform a patient study in which the patients use a wearable to objectively monitor their motor symptoms, and a logbook to record the subjective rating of the clinical state by the patient itself, in combination with the recording of the STN LFP from the DBS lead. The latter can be used to reconstruct the CSD using the method designed in the first recommended study. The data analyses should

consists of three main parts. Firstly, use ultra-high field MRI to create patient-specific models by fitting a 3D STN structure and locating the DBS lead location in it. The measured CSD and location of the sources relates to this patient-specific brain model. Secondly, to relate the CSD sources to symptoms on a group level, all the patient-specific models should be transferred to a generic brain model as shown in Figure 7-4. Using the same transformation on the CSD the patient specific sources are also transforming to the generic brain model. Thirdly, use machine learning or deep learning approaches to find a relation between the CSD and the objective scoring of the motor symptoms and the subjective scoring of the patient's clinical state. This possibly results in the localization of symptom specific 'sweet spots' in the CSD.

3. Perform a proof of principle patient study with the aim to target sweet spots in the CSD, by applying a directional DBS protocol.

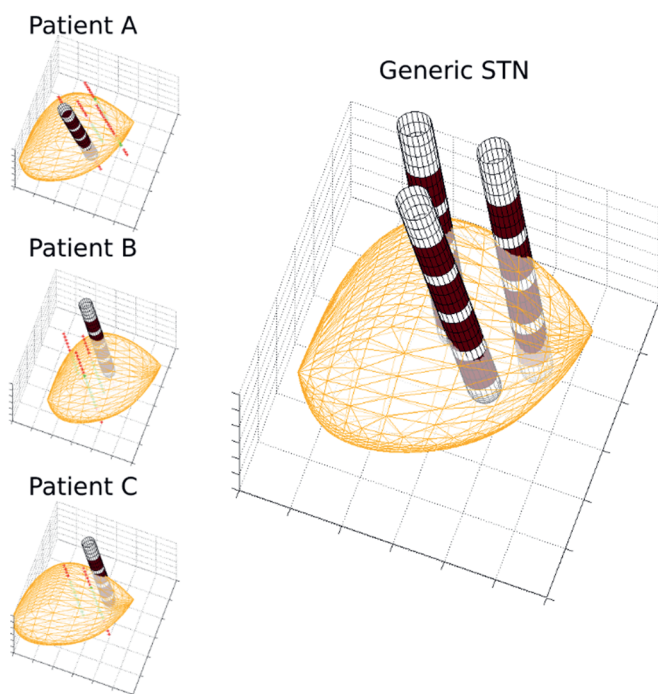


Figure 7-4, On the left, three patient-specific 3D STN models including the implanted DBS lead. On the right, the three patient specific implanted DBS leads transformed to a generic STN model (Figure by Verhagen et al [35]).

## References

1. Langreth, B. R., & Waldholz, M. (1999). New era of personalized medicine: targeting drugs for each unique genetic profile. *The oncologist*, 4(5), 426.
2. Hamburg, M. A., & Collins, F. S. (2010). The path to personalized medicine. *New England Journal of Medicine*, 363(4), 301-304.
3. Okun, M. S., Tagliati, M., Pourfar, M., Fernandez, H. H., Rodriguez, R. L., Alterman, R. L., & Foote, K. D. (2005). Management of referred deep brain stimulation failures: a retrospective analysis from 2 movement disorders centers. *Archives of neurology*, 62(8), 1250-1255.
4. Hamel, W., Fietzek, U., Morsnowski, A., Schrader, B., Herzog, J., Weinert, D., ... & Mehdorn, H. M. (2003). Deep brain stimulation of the subthalamic nucleus in Parkinson's disease: evaluation of active electrode contacts. *Journal of Neurology, Neurosurgery & Psychiatry*, 74(8), 1036-1046.
5. Duchin, Y., Shamir, R. R., Patriat, R., Kim, J., Vitek, J. L., Sapiro, G., & Harel, N. (2018). Patient-specific anatomical model for deep brain stimulation based on 7 Tesla MRI. *PloS one*, 13(8), e0201469.
6. Plantinga, B. R., Temel, Y., Duchin, Y., Uludağ, K., Patriat, R., Roebroek, A., ... & Harel, N. (2018). Individualized parcellation of the subthalamic nucleus in patients with Parkinson's disease with 7T MRI. *Neuroimage*, 168, 403-411.
7. Verhagen, R., Schuurman, P. R., van den Munckhof, P., Contarino, M. F., de Bie, R. M., & Bour, L. J. (2016). Comparative study of microelectrode recording-based STN location and MRI-based STN location in low to ultra-high field (7.0 T) T2-weighted MRI images. *Journal of neural engineering*, 13(6), 066009.
8. Zwartjes, D. G., Janssen, M. L., Heida, T., Van Kranen-Mastenbroek, V., Bour, L. J., Temel, Y., ... & Veltink, P. H. (2013). Cortically evoked potentials in the human subthalamic nucleus. *Neuroscience letters*, 539, 27-31.
9. Gunalan, K., & McIntyre, C. C. (2020). Biophysical reconstruction of the signal conduction underlying short-latency cortical evoked potentials generated by subthalamic deep brain stimulation. *Clinical Neurophysiology*, 131(2), 542-547.
10. Swann, N. C., de Hemptinne, C., Thompson, M. C., Miocinovic, S., Miller, A. M., Ostrem, J. L., ... & Starr, P. A. (2018). Adaptive deep brain stimulation for Parkinson's disease using motor cortex sensing. *Journal of neural engineering*, 15(4), 046006.
11. Bour, L. J., Lourens, M. A. J., Verhagen, R., de Bie, R. M., Van Den Munckhof, P., Schuurman, P. R., & Contarino, M. F. (2015). Directional recording of subthalamic spectral power densities in parkinson's disease and the effect of steering deep brain stimulation. *Brain stimulation*, 8(4), 730-741.

12. Tinkhauser, G., Pogosyan, A., Debove, I., Nowacki, A., Shah, S. A., Seidel, K., ... & Oertel, M. (2018). Directional local field potentials: a tool to optimize deep brain stimulation. *Movement disorders*, 33(1), 159-164.
13. Potworowski, J., Jakuczun, W., Łęski, S., & Wójcik, D. (2012). Kernel current source density method. *Neural computation*, 24(2), 541-575.
14. Giannicola, G., Marceglia, S., Rossi, L., Mrakic-Sposta, S., Rampini, P., Tamma, F., ... & Priori, A. (2010). The effects of levodopa and ongoing deep brain stimulation on subthalamic beta oscillations in Parkinson's disease. *Experimental neurology*, 226(1), 120-127.
15. Little, S., Pogosyan, A., Kuhn, A. A., & Brown, P. (2012). Beta band stability over time correlates with Parkinsonian rigidity and bradykinesia. *Experimental neurology*, 236(2), 383-388.
16. Habets, J. G., Heijmans, M., Kuijf, M. L., Janssen, M. L., Temel, Y., & Kubben, P. L. (2018). An update on adaptive deep brain stimulation in Parkinson's disease. *Movement Disorders*, 33(12), 1834-1843.
17. Rovini, E., Maremmani, C., & Cavallo, F. (2017). How wearable sensors can support Parkinson's disease diagnosis and treatment: a systematic review. *Frontiers in neuroscience*, 11, 555.
18. Eskofier, B. M., Lee, S. I., Daneault, J. F., Golabchi, F. N., Ferreira-Carvalho, G., Vergara-Diaz, G., ... & Bonato, P. (2016, August). Recent machine learning advancements in sensor-based mobility analysis: Deep learning for Parkinson's disease assessment. In *2016 38th Annual International Conference of the IEEE Engineering in Medicine and Biology Society (EMBC)* (pp. 655-658). IEEE.
19. Dembek, T. A., Reker, P., Visser-Vandewalle, V., Wirths, J., Treuer, H., Klehr, M., ... & Timmermann, L. (2017). Directional DBS increases side-effect thresholds—A prospective, double-blind trial. *Movement Disorders*, 32(10), 1380-1388.
20. Contarino, M. F., Bour, L. J., Verhagen, R., Lourens, M. A., de Bie, R. M., van den Munckhof, P., & Schuurman, P. R. (2014). Directional steering: a novel approach to deep brain stimulation. *Neurology*, 83(13), 1163-1169.
21. Steffen, J. K., Reker, P., Mennicken, F. K., Dembek, T. A., Dafsari, H. S., Fink, G. R., ... & Barbe, M. T. (2020). Bipolar directional deep brain stimulation in essential and parkinsonian tremor. *Neuromodulation: Technology at the Neural Interface*, 23(4), 543-549.
22. Steigerwald, F., Müller, L., Johannes, S., Matthies, C., & Volkmann, J. (2016). Directional deep brain stimulation of the subthalamic nucleus: a pilot study using a novel neurostimulation device. *Movement Disorders*, 31(8), 1240-1243.

23. Kramme, J., Dembek, T. A., Treuer, H., Dafsari, H. S., Barbe, M. T., Wirths, J., & Visser-Vandewalle, V. (2021). Potentials and limitations of directional deep brain stimulation: a simulation approach. *Stereotactic and Functional Neurosurgery*, 99(1), 65-74.
24. Machado, A., Rezai, A. R., Kopell, B. H., Gross, R. E., Sharan, A. D., & Benabid, A. L. (2006). Deep brain stimulation for Parkinson's disease: surgical technique and perioperative management. *Movement disorders: official journal of the Movement Disorder Society*, 21(S14), S247-S258.
25. Anderson, D. N., Osting, B., Vorwerk, J., Dorval, A. D., & Butson, C. R. (2018). Optimized programming algorithm for cylindrical and directional deep brain stimulation electrodes. *Journal of neural engineering*, 15(2), 026005.
26. Chaturvedi, A., Foutz, T. J., & McIntyre, C. C. (2012). Current steering to activate targeted neural pathways during deep brain stimulation of the subthalamic region. *Brain stimulation*, 5(3), 369-377.
27. Groppa, S., Herzog, J., Falk, D., Riedel, C., Deuschl, G., & Volkmann, J. (2014). Physiological and anatomical decomposition of subthalamic neurostimulation effects in essential tremor. *Brain*, 137(1), 109-121.
28. Xu, W., Miocinovic, S., Zhang, J., Baker, K. B., McIntyre, C. C., & Vitek, J. L. (2011). Dissociation of motor symptoms during deep brain stimulation of the subthalamic nucleus in the region of the internal capsule. *Experimental neurology*, 228(2), 294-297.
29. Moks, C. B., Butson, C. R., Walter, B. L., Vitek, J. L., & McIntyre, C. C. (2009). Deep brain stimulation activation volumes and their association with neurophysiological mapping and therapeutic outcomes. *Journal of Neurology, Neurosurgery & Psychiatry*, 80(6), 659-666.
30. Little, S., & Brown, P. (2020). Debugging adaptive deep brain stimulation for Parkinson's Disease. *Movement Disorders*, 35(4), 555-561.
31. Rosa, M., Arlotti, M., Ardolino, G., Cogiamanian, F., Marceglia, S., Di Fonzo, A., ... & Priori, A. (2015). Adaptive deep brain stimulation in a freely moving Parkinsonian patient. *Movement Disorders*, 30(7), 1003.
32. Arlotti, M., Marceglia, S., Foffani, G., Volkmann, J., Lozano, A. M., Moro, E., ... & Rampini, P. (2018). Eight-hours adaptive deep brain stimulation in patients with Parkinson disease. *Neurology*, 90(11), e971-e976.
33. Graupe, D., Khobragade, N., Tuninetti, D., Basu, I., Slavin, K. V., & Verhagen Metman, L. (2018). Who may benefit from on-demand control of deep brain stimulation? Noninvasive evaluation of Parkinson patients. *Neuromodulation: Technology at the Neural Interface*, 21(6), 611-616.
34. Steigerwald, F., Matthies, C., & Volkmann, J. (2019). Directional deep brain stimulation. *Neurotherapeutics*, 16(1), 100-104.

35. Verhagen, R., Lourens, M., Contarino, M., de Bie, R., van den Munckhof, P., Schuurman, R., Bour, L. (2014). Automatically generated STN model based on intraoperative microelectrode recordings assists in postoperative management of DBS settings and clinical research. Poster P379. *30th International Congress of Clinical Neurophysiology (ICCN) of the IFCN, March 20–23, 2014, Berlin, Germany.*





# Publications

## Journal papers

Van Dijk, K. J., Verhagen, R., Chaturvedi, A., McIntyre, C. C., Bour, L. J., Heida, C., & Veltink, P. H. (2015). A novel lead design enables selective deep brain stimulation of neural populations in the subthalamic region. *Journal of neural engineering*, 12(4), 046003.

van Dijk, K. J., Janssen, M. L., Zwartjes, D. G., Temel, Y., Visser-Vandewalle, V., Veltink, P. H., ... & Heida, T. (2016). Spatial localization of sources in the rat subthalamic motor region using an inverse current source density method. *Frontiers in neural circuits*, 10, 87.

van den Noort, J. C., Verhagen, R., van Dijk, K. J., Veltink, P. H., Vos, M. C., de Bie, R. M., ... & Heida, C. T. (2017). Quantification of hand motor symptoms in Parkinson's disease: A proof-of-principle study using inertial and force sensors. *Annals of biomedical engineering*, 45(10), 2423-2436.

van Dijk, K. J., Verhagen, R., Bour, L. J., Heida, C., & Veltink, P. H. (2018). Avoiding Internal Capsule Stimulation With a New Eight-Channel Steering Deep Brain Stimulation Lead. *Neuromodulation: Technology at the Neural Interface*, 21(6), 553-561.

## Conference papers

van den Noort, J., van Dijk, K., Kortier, H., van Beek, N., Verhagen, R., Bour, L., & Veltink, P. (2014, June). Applications of the powerglove for measurement of finger kinematics. In *2014 11th International Conference on Wearable and Implantable Body Sensor Networks Workshops* (pp. 6-10). IEEE.

## Conference abstracts

van Dijk, K. J., Zwartjes-de Klerk, D.G.M., Janssen, M.L.F., Benazzouz, A., Temel, V., Visser-Vandewalle, V., Heida, T., & Veltink, P.H., (2013). Current source density analysis of cortically evoked potentials in the rat subthalamic nucleus. *4th dutch bio-medical engineering conference 2013*.

van Dijk, K. J., Verhagen, R., Bour, L.J., & Heida, T., (2013). Selectively stimulating neural populations in the subthalamic region using a novel deep brain stimulation lead design. *6th International IEEE/EMBS Conference on Neural Engineering (NER) 2013*

van Dijk, K. J., Verhagen, R., Bour, L. J., Veltink, P. H., & Heida, T., (2015). Selective stimulation of the subthalamic nucleus using a high density DBS lead. *5th dutch bio-medical engineering conference 2015*.

van Dijk K. J., Verhagen R., van den Noort J., Bour L.J., Veltink P.H., & Heida T., (2015). The PowerGlove: Assessment of hand and finger movements in Parkinson's disease patients. *19th International Congress of Parkinson's Disease and Movement Disorders 2015*

van Dijk K. J., Urbizagástegui P. A., Veltink P.H., Heida T., (2015). Assessing the sensitivity of current source density methods to measurement errors. *7th International IEEE/EMBS Conference on Neural Engineering (NER) 2015*



# Dankwoord

### *Het begint met fascinatie*

Ik weet nog goed dat ik voor het eerst in aanraking kwam met de vakgroep biomedische signalen en systemen (BSS). Ik was mij aan het oriënteren voor een specialisatie-richting binnen mijn master elektrotechniek en er was een voorlichtingsmiddag waar ik mij voor had opgegeven. Ik wilde na mijn bachelor graag iets anders doen dan ‘die-hard’ elektrotechniek en tijdens de voorlichtingsmiddag zouden alle vakgroepen een korte introductie over zichzelf geven. Tijdens het praatje van BSS hoorde ik over het onderzoek dat zij deden naar de communicatie tussen hersencellen/neuronen, en dat dit gaat via kleine elektrische signaaltjes. Het was onder andere mogelijk om deze neurale signalen te meten, de cellen te stimuleren en neurale netwerken dingen te leren en te beïnvloeden. Ik was gelijk gefascineerd.

Ik voerde mijn master afstudeeropdracht uit onder begeleiding van onder andere Ciska Heida en Peter Veltink. Zij bleven mij ook daarna begeleiden als mijn twee promotoren tijdens mijn promotie project.

### *De promotoren*

Beste Ciska, jij was mijn dagelijkse begeleider en eerste aanspreekpunt als ik ergens mee vast liep. Ik wil je heel erg bedanken voor al onze goede discussies tijdens de wekelijkse overleggen en de tips en suggesties die jij gaf op al mijn eerste draft documenten: journal papers, conference abstracts, posters en presentaties. Ik kan je zeer nuchtere aanpak erg waarderen. Tijdens mijn promotie hebben we samen twee keer de Neural Engineering conferentie bezocht, eerst in San Diego en twee jaar later in Montpellier. Ik weet nog goed dat jij in San Diego een klein Japans noodle restaurantje had gevonden waar we gingen eten. We waren precies op tijd, want een half uurtje later was het restaurant vol en stond er een lange rij buiten met wachtende mensen die naar binnen wilden. Het eten was super lekker; een mooie herinnering.

Beste Peter, heel erg bedankt voor alle tijd en energie die je in mijn begeleiding hebt gestoken. Ik was altijd erg onder de indruk van hoe snel, goed en scherp je commentaar kon geven op de stukken die ik je ter review stuurde. Je was altijd erg geïnteresseerd in mijn onderzoek, maar ook in de dingen daarbuiten. Dit zorgde voor een fijne samenwerking.

### *Het project*

Mijn promotie project viel binnen een groter project getiteld ‘Neuromodulatie bij de ziekte van Parkinson. Naar een intelligente vorm van diepe hersenstimulatie’. Ik wil graag beginnen met het bedanken van de Stichting Toegepast Wetenschappelijk Instituut voor

Neuromodulatie (TWIN) voor het financieel mogelijk maken van dit project. De organisatie van het project was ingericht om de krachten van twee PHD studenten te bundelen. Stichting TWIN financierde de plek van Rens Verhagen onder begeleiding van Lo Bour in het Academisch Medisch Centrum in Amsterdam met de focus meer op de klinische kant, en mijn plek aan universiteit Twente met een focus meer op de techniek van neuromodulatie. Ik wil Lo en Rens graag bedanken voor deze samenwerking. Jullie inbreng in mijn onderzoek was zeer waardevol. Het was een mooie samenwerking om de Powerglove studie op te zetten waarin de techniek en de patiënt echt samen kwamen. Rens ik wil je ook bedanken voor de gezelligheid tijdens onze tripjes, eerst Cleveland, later San Diego.

#### *Het onderzoek*

Het onderzoek dat ik in dit proefschrift heb gepresenteerd had ik niet kunnen doen zonder de bijdrage van vele anderen. Natuurlijk wil ik al mijn coauteurs bedanken die mee hebben gewerkt aan mijn artikelen. Daarnaast wil ik ook een aantal anderen nog persoonlijk noemen en bedanken.

I would like to thank Ashu Chaturvedi and Cameron McIntyre for sharing their knowledge on computational modelling and for letting me visit the lab at Case Western Reserve University. This was a great start for my modelling studies and a highly motivational visit.

Zoals ik aangaf in het eerste deel van mijn dankwoord voerde ik mijn afstudeeropdracht uit bij BSS. Deze opdracht heeft mij uiteindelijk doen besluiten om te gaan promoveren. Ik wil daarom graag Daphne bedanken voor de leuke inspirerende opdracht. Mark, ook jouw inbreng was erg belangrijk in mijn keuze. Het project liet een mooie samenwerking zien tussen de techniek en de kliniek. Ik heb jouw commentaar op mijn onderzoek, later ook tijdens mijn promotie, erg gewaardeerd.

Voor de klinische studie met de Powerglove wil ik Josien bedanken voor het, samen met Rens en mij, opzetten van de studie. Het schrijven van de METC was een heel werk wat we mooi met z'n drieën voor elkaar hebben gekregen. Verder wil ik Ed bedanken voor de technische ondersteuning. Prof. de Bie, Marije Scholten en Miranda Postma voor het faciliteren en de hulp van het onderzoek in het AMC. Ook ben ik zeer dankbaar voor de patiënten die mee hebben gedaan aan het onderzoek. Het was bijzonder om te zien dat zij enthousiast waren over het onderzoek en graag mee wilden doen. Tot slot wil ik de studenten bedanken die ik heb mogen begeleiden en die hebben mee gewerkt aan verschillende onderwerpen in mijn proefschrift: Joao, Michelle, Pablo, Emiel en Keshava.

### *Collega's en vrienden*

Naast het serieuze werk moet er ook ontspannen worden. Het is een erg fijne en gezellige tijd geweest om bij BSS te werken. Met een leuke hechte club aan collega's die ik wil bedanken. Laat ik beginnen met mijn paranimfen: Beste Frauke, we begonnen rond dezelfde tijd met onze promotie projecten bij BSS en waren zo'n vier jaar kamergenoten. Ons kantoor was soms ijsig koud, als de airco weer eens ontregeld was, maar gelukkig hadden we altijd onze warme koffie van ons eigen koffiezetapparaat. Ik heb altijd het gevoel gehad dat we ons als een echt team door onze promotie hebben gewerkt. Heel erg bedankt daarvoor.

Beste Frederiek, jij begon iets later met je promotie project bij BSS, maar we konden het al snel goed met elkaar vinden. We hadden dezelfde muziek-, film- en seriesmaak. We moesten, als we het hadden over onze boekjes, vaak lachen om de songtekst van Spinvis: "In de spiegel neem ik soms alvast de pose aan voor de foto op de achterkant". Ik moet je helaas teleurstellen dat er geen foto op de achterkant terecht is gekomen. Bedankt voor al de leuke gesprekken, de optredens die we hebben bezocht, en natuurlijk de gezellige Game of Thrones avonden met een speciaal biertje bij jou en Sander.

Verder wil ik voor de leuke gesprekken, lunch wandelingen, vrijdag middag borrels, fiets tochtjes, het legendarische tripje naar Edinburgh, het zeil uitje, whisky proefavondjes, bedanken: Hendrik, Tom, Fokke, Angelos, Hossein, Frank, Thijs, Robert-Jan, Miriam, Lamia, Yan, Xenia, Wendy, Ainara, Ed, Gerjo, Wies, Marcel, Sandra en Bert-Jan. Natuurlijk ook Henk en Dirk, na onze tijd bij BSS zijn we door gegaan met de whisky proefavonden een mooie traditie die we nog lang door moeten zetten.

Hoe gezellig de vakgroep ook was, ik zag ook nog andere mensen dan mijn collega's bij BSS. Elk jaar ging ik met de vrienden van de studie, Daniel, Tim, Hans, Rene, Peter en Jos, een lang weekend fietsen. Niets zo fijn om je hoofd leeg te maken als op de fiets, niet alleen tijdens het weekend maar ook tijdens de trainingsritjes daarvoor. Bedankt hiervoor. Ook wil ik mijn vrienden Leonard, Jochem, Jasper, en Maarten bedanken voor de goede diepe gesprekken en de uitstapjes buiten mijn technische bubbel.

Ik ben ondertussen al weer drie jaar aan het werk bij Demcon. Ik wil hier mijn collega's bedanken en in het bijzonder Michiel. Met ons control team zijn we interessante, uitdagende dingen aan doen, waar ik de afgelopen drie jaar nieuwe energie uit put.



### *Mijn familie*

Ik ben zeer dankbaar voor de fijne band die ik heb met mijn familie. Ik wil mijn broers Aad en Jan bedanken, dat ik altijd op ze kan bouwen en voor de interesse die ze altijd toonden in mijn werk. Bedankt voor de gezellige verjaardagen en al die keren dat we de BBQ hebben aangestoken. Die dagen waren natuurlijk niet compleet zonder ook jullie gezellige aanwezigheid: Saskia, Lisa, Anouk, Siegrid, Mike en Jesse. Ook jullie heel erg bedankt. Lieve mama, jij en papa hebben mij altijd onvoorwaardelijk gesteund en in mij geloofd. Eerst toen ik verder wilde studeren na mijn bachelor en daarna tijdens mijn promotie. Ik ben je hier voor altijd dankbaar voor. Het is super verdrietig dat pa de afronding van mijn promotie niet meer heeft mogen meemaken, maar ik weet zeker dat hij heel erg trots op mij zou zijn geweest.

Tot slot, lieve Jorinde. Ik ben heel gelukkig dat wij elkaar hebben ontmoet. Het viel niet mee om mijn proefschrift af te maken naast mijn werk bij Demcon, maar jij hebt de last van de laatste loodjes draagbaar gemaakt. Met al je leuke ideeën, mooie uitstapjes en je drang om er op uit te trekken, weet jij me uit mijn comfort-zone te trekken en altijd op te vrolijken. We hebben samen al twee mooie reizen gemaakt en ik hoop dat we binnenkort weer de wijde wereld in mogen trekken, om samen de wereld en ons leven verder te ontdekken.



